Doctoral School of Experimental and Preventive Medicine

Albert Szent-Györgyi Medical School

University of Szeged, Hungary

Quantitative histological and in vitro fluorescence microscopy image analysis: workflow automation, deep learning, and morphometric profiling of subcellular, cellular, and extracellular components of nervous tissue origin

PhD Thesis

Gábor Attila Barczánfalvi

Department of Cell Biology and Molecular Medicine

Department of Medical Physics and Informatics

Supervisors:

Prof. Dr. Károly Gulya (2022-2026)

Dr. József Tolnai (2024-2026)

Prof. Dr. László Tiszlavicz (2022-2023)

Szeged

2026

Peer-reviewed publications related to the PhD Thesis

MTMT Identifier: 10084757; ORCID ID: 0000-0002-2187-8264

I. Barczánfalvi, G., Nyári, T., Tolnai, J., Tiszlavicz, L., Gulyás, B., & Gulya, K. (2025). *Automated Segmentation and Morphometric Analysis of Thioflavin-S-Stained Amyloid Deposits in Alzheimer's Disease Brains and Age-Matched Controls Using Weakly Supervised Deep Learning.* **International Journal of Molecular Sciences**, *26*(15), 7134. https://doi.org/10.3390/ijms26157134 (*2024 (latest available) IF: 4.9; SJR ranking: Q1/D1)*

II. Szabo, M., Lajkó, N., Dulka, K., Barczánfalvi, G., Lőrinczi, B., Szatmári, I., Mihály, A., Vécsei, L., & Gulya, K. (2023). *The kynurenic acid analog SZR104 induces cytomorphological changes associated with the anti-inflammatory phenotype in cultured microglia.* **Scientific reports**, *13*(1), 11328. https://doi.org/10.1038/s41598-023-38107-8 *(2023 IF: 3.8; SJR ranking: Q1/D1)*

III. Pesti, I., Barczánfalvi, G., Dulka, K., Kata, D., Farkas, E., & Gulya, K. (2024). *Bafilomycin 1A Affects p62/SQSTM1 Autophagy Marker Protein Level and Autophagosome Puncta Formation Oppositely under Various Inflammatory Conditions in Cultured Rat Microglial Cells.* **International Journal of Molecular Sciences**, *25*(15), 8265. https://doi.org/10.3390/ijms25158265 *(2024 IF: 4.9; SJR ranking: Q1/D1)*

MSc Thesis

◆ Barczánfalvi, G. (2022). *Thioflavin S-sel jelölt amiloid plakkok és depozitumok kvantitatív morfológiai vizsgálata Alzheimer-kóros agyban.* (*Quantitative morphological analysis of thioflavin S-labeled amyloid plaques and deposits in Alzheimer's diseased brain)* **Biology MSc Thesis**, University of Szeged, Faculty of Science and Informatics, Department of Cell Biology and Molecular Medicine, Supervisor: Prof. Dr. Károly Gulya) https://diploma.bibl.u-szeged.hu/id/eprint/135756

➢ *The structure of this Thesis is based on the publications listed above. Subchapters corresponding to the peer-reviewed publications are indicated by a superscript Roman numeral (I., II., and III.) in their respec-tive headings. The main body of the Thesis is based on the primary, first-author publication (I.), for which the author's MSc Thesis served as foundational work. Furthermore, references are also made to supplementary materials of the associated publications (e.g., tables, figures, and datasheets), indicated by a specific notation that prefixes the label with the corresponding Roman numeral of the source publication.*

Co-author certification

We, the undersigned, Gábor Attila Barczánfalvi PhD candidate as the author of this Thesis and Professor Dr. Károly Gulya as the corresponding author of the associated publications, hereby certify on behalf of all co-authors that:

- All co-authors of the jointly published research have no conflict of interest, and the sections of this dissertation pertaining to the collaborative publications accurately represent the significant intellectual and methodological contributions of the PhD candidate.
- While relevant aspects from the broader collaborative studies are briefly mentioned to ensure narrative coherence and provide necessary scientific context, the work attributable to other co-authors is explicitly distinguished from the candidate's own contributions throughout this Thesis.
- The candidate's specific work and original contributions presented in this Thesis have not formed, and will nor form, the basis for any other qualification process for obtaining a PhD degree.

February 12, 2026		
.....	.....	……..
Date	PhD candidate	Corresponding author

The publications related to the above statement:

- Szabo, M., Lajkó, N., Dulka, K., Barczánfalvi, G., Lőrinczi, B., Szatmári, I., Mihály, A., Vécsei, L., & Gulya, K. (2023). *The kynurenic acid analog SZR104 induces cytomorphological changes associated with the anti-inflammatory phenotype in cultured microglia.* **Scientific reports**, *13*(1), 11328. https://doi.org/10.1038/s41598-023-38107-8

- Pesti, I., Barczánfalvi, G., Dulka, K., Kata, D., Farkas, E., & Gulya, K. (2024). *Bafilomycin 1A Affects p62/SQSTM1 Autophagy Marker Protein Level and Autophagosome Puncta Formation Oppositely under Various Inflammatory Conditions in Cultured Rat Microglial Cells.* **International Journal of Molecular Sciences**, *25*(15), 8265. https://doi.org/10.3390/ijms25158265

Abbreviations

AD: Alzheimer's disease

Adam: adaptive moment estimation

AI: artificial intelligence

ANN: artificial neural network

ANOVA: analysis of variance

APP: amyloid precursor protein

Aβ: amyloid-β

BAF: bafilomycin A1

BBB: blood-brain barrier

BG: background

CAA: cerebral amyloid angiopathy

CAM: class activation maps/mapping

CERAD: Consortium to Establish a Registry for Alzheimer's Disease

CNN: convolutional neural network

CV: computer vision

DAPI: 2-[4-(aminoiminomethyl)phenyl]-1H-indole-6-carboximidamide hydrochloride

DL: deep learning

DSC: Dice similarity coefficient

FC: fully connected

FDR: false discovery rate

FG: foreground

$FN_{c/s}$: false negatives for classification/segmentation tasks

FNR: false negative rate

FOR: false omission rate

$FP_{c/s}$: false positives for classification/segmentation tasks

FPR: false positive rate

GAP: global average pooling

GMP: global max pooling

GNN: graph neural network

GT: ground truth

ICF: illumination correction function

IoU: intersection over union (Jaccard index)

KYNA: kynurenic acid

LPS: lipopolysaccharide

ML: machine learning

MLP: multi-layer perceptron

mTI: modified Tversky index

NFT: neurofibrillary tangles

NIA-AA: National Institute on Aging–Alzheimer's Association

NLP: natural language processing

NPV: negative predictive value

PA: pixel-level accuracy

PCA: principal component analysis

PCs: principal components

p62/SQSTM1: sequestosome 1

ReLU: rectified linear unit

RMSprop: root mean square propagation

RNN: recurrent neural network

ROIs: regions of interest

RST: rosuvastatin

SMO: Silver Mountain Operator

Soft-CP: soft-copy and soft-paste

SZR104: N-(2-(dimethylamino)ethyl)-3-(morpholinomethyl)-4-hydroxyquinoline-2-carboxamide

TAP: thresholded average pooling

ThioS: thioflavin S

$TN_{c/s}$: true negatives for classification/segmentation tasks

$TP_{c/s}$: true positives for classification/segmentation tasks

WSOL: weakly supervised object localization

WSSS: weakly supervised semantic segmentation

$\mathscr{L}_{aUF}$: asymmetric unified focal loss

$\mathscr{L}_{BC}$: binary cross-entropy loss

$\mathscr{L}_{maF}$: modified asymmetric focal loss

$\mathscr{L}_{maFT}$: modified asymmetric focal Tversky loss

Table of contents

1. Introduction and background

1.1 Neuropathology of Alzheimer's disease[I.]

Alzheimer's disease (AD), the leading cause of dementia in late middle-aged and older adults, is a progressive neurodegenerative disorder characterized by a clinically heterogeneous phenotype and a multifactorial etiology. Its sporadic form, which constitutes the vast majority of cases, arises from a complex and still incompletely understood interplay of genetic and environmental factors [1–4]. A gradual deterioration of cognitive abilities, including executive control, defines the clinical phase of AD, leading to a decline in daily functioning and social engagement. This manifests in a range of clinical symptoms, including memory deficits, disorientation, compromised reasoning and judgment, communication impairments, mood disorders, and apathy [1–6]. Critically, this symptomatic stage is preceded by a silent, preclinical stage that can span several decades, characterized by the gradual deposition of protein aggregates throughout the cortex [2,5].

A definitive post-mortem diagnosis of AD relies on specific neuropathological criteria, though the broader histopathological landscape associated with the disease falls into two main categories [3–6]. The first is structural loss, defined by widespread neurodegeneration (entailing neuronal and synaptic loss). This process culminates in macroscopic cortical atrophy (a reduction in brain volume and weight), which is particularly prominent in the medial temporal lobe and strongly correlates with the degree of cognitive impairment [2,6]. Conversely, the second category, emerging abnormal alteration, comprises a spectrum of histopathological changes. Foremost among these are the extracellular deposition of amyloid-β (Aβ) peptides into various plaque types and the intracellular accumulation of hyperphosphorylated, misfolded tau protein aggregates forming neurofibrillary tangles (NFTs) [3,4,6]. Other key alterations include cerebral amyloid angiopathy (CAA), the deposition of Aβ in blood vessel walls, and a robust neuroinflammatory glial response involving both astrogliosis and microglial activation, often in spatial proximity to parenchymal plaques [3,6–10].

The two defining components of the mixed proteinopathy in AD, tau and Aβ, each follow a characteristic hierarchical pattern of spatiotemporal progression, though the topographic distribution and temporal dynamics of these disease hallmarks differ considerably [2,5]. The spread of tau pathology is remarkably predictable and sequential, as systematically described by the Braak staging system [1]. This system stages pathology based on the neuroanatomical location and density of NFTs. Tau pathology typically originates from the transentorhinal regions, advances through anatomically connected areas to limbic structures, and eventually involves the neocortex [1,2,5,6,11]. In contrast, the deposition of Aβ plaques follows a descending pattern of progression as outlined by the Thal phases, spreading from the neocortex through limbic and allocortical regions to eventually reach the brainstem and cerebellum [8,9]. However, unlike tau pathology, the Aβ burden correlates poorly with the

degree of cognitive impairment and displays significant structural heterogeneity [3–6,11]. While the Thal phases describe this anatomical sequence, they do not account for the considerable inter-individual variability observed in the quantity and morphology of the plaques themselves [5,11,12]. Complementing these immunostaining-based topographical systems, the Consortium to Establish a Registry for Alzheimer's Disease (CERAD) protocol [13] introduced a standardized, semi-quantitative assessment of neuritic plaque density within the neocortex. This diagnostic score is based on thioflavin S (ThioS) or silver staining and focuses on a specific plaque subtype characterized by adjacent, NFT-rich dystrophic neurites [5,11,13,14].

The three most influential neuropathological metrics, the Thal phases for Aβ staging, the Braak stages for tau pathology, and the CERAD score for neuritic plaque density, are all integrated in the modern diagnostic guidelines from the National Institute on Aging–Alzheimer's Association (NIA-AA), often referred to as the "ABC" scoring system [15,16]. However, these influential staging systems primarily rely on semi-quantitative assessments and largely disregard the extensive morphological diversity of Aβ pathology [1,5,8,11,15,16], and therefore create a need for more objective, quantitative methods capable of capturing the full spectrum of pathology, including the structural complexity of the Aβ plaques.

1.2 Amyloid plaques: From formation to morphological diversity[I.]

The formation of parenchymal plaques, a pathological hallmark of AD, is driven by the extracellular accumulation and aggregation of Aβ peptides. These peptides, typically 36 to 43 amino acids in length, are generated through the sequential enzymatic cleavage of the amyloid precursor protein (APP), a transmembrane glycoprotein [11,14,17,18]. Among the various isoforms, the 42-amino-acid-long Aβ42 peptide is central to plaque pathogenesis; while produced in smaller quantities than Aβ40, its greater hydrophobicity makes it more prone to aggregation and more neurotoxic, establishing it as the dominant component of dense-cored plaques [6,19,20]. This process of Aβ cleavage and subsequent extracellular aggregation forms the cornerstone of the amyloid hypothesis, which posits that the accumulation of Aβ is the primary trigger for AD's downstream pathology [21]. The aggregation cascade begins with the assembly of monomers into soluble, synapto- and neurotoxic oligomers and progresses to the formation of insoluble, β-sheet-rich fibrils that constitute the core of the Aβ plaques [6,20,21].

The presence of these Aβ aggregates instigates a robust neuroinflammatory response by activating glial cells, which, despite their initial neuroprotective role in attempting to clear deposits, contribute to a persistent, neurotoxic inflammatory microenvironment upon chronic activation [7,10]. This glial response is also linked to a key genetic risk factor for sporadic AD: the ε4 allele of apolipoprotein E,

a protein primarily produced by glial cells in the brain [22,23].

The morphological appearance of the Aβ plaques is remarkably heterogeneous, a characteristic that poses a significant challenge to traditional classification schemes, which are often based on subjective qualitative assessments or inconsistent in their application of quantitative criteria such as size, shape, density, and staining properties [4,24]. At its simplest, this diversity can be conceptualized as a spectrum spanning two broad categories: loosely structured diffuse deposits and dense, Congo red-positive compact plaques, with a wide range of transitional forms existing between these polarities [4,11].

Diffuse plaques (i.e., pre-amyloid deposits), the most prevalent type in the AD brain, encompass a broad morphological spectrum ranging from non-congophilic, moderately Aβ-immunoreactive forms to loosely structured fibrillar deposits showing slight positivity with amyloid probes. This category is defined by the lack of dense regions, alongside the general rarity of dystrophic neurites and significant glial reactivity; the dominant component of these forms is Aβ42. Morphologically, diffuse plaques can appear in diverse forms with variable dimensions, amorphous structure, and poorly defined margins (e.g., small, star-shaped deposits or large "cotton-wool" and "lake-like" structures); their prevalence in cognitively healthy individuals with a high Aβ load also suggests an earlier or less toxic stage of deposition [4,9,11].

In contrast, compact plaques are defined by a dense, fibrillar Aβ-structure detectable with silver staining and positive for immunostaining and amyloid-probes such as ThioS and Congo red. Typically, they are oval or spherical in shape, with diameters ranging from 20 to 60 μm. The most well-characterized subtype is the classical "dense-cored" plaque (focal deposits), which exhibits a complex structural organization and predominantly contains Aβ42: a central condensed core surrounded by a transitional region with reduced Aβ content, and a diffuse, loosely organized peripheral corona ("halo"). This intricate structure is frequently infiltrated by dystrophic tau-positive neurites and the processes of reactive glial cells, leading to the formation of neuritic plaques, a subtype strongly associated with local neurotoxicity [3,4,9,11]. Other variations on the compact theme include less structured, "immature" fibrillar forms, as well as two subtypes predominantly composed of Aβ40: the smaller "burned-out" (or "core-only") plaques, lacking a peripheral region and considered remnants of late-stage development, and the "coarse-grain" plaques, containing multiple smaller cores [3,4,9,25–27].

One leading hypothesis proposes a developmental sequence in which amorphous, diffuse deposits containing oligomers and protofibrils progressively evolve through more fibril-rich "primitive" or "immature" forms into classical dense-cored and ultimately into "burned-out" plaques, a process potentially driven by the inflammatory microglial response [12,28,29]. However, the temporal order of these events in the human brain is difficult to establish, and an alternative view suggests that different

plaque types may arise and evolve independently, dictated by local, region-specific factors and individual patient characteristics [4,12].

Complementing these biological models of plaque evolution, a consistent statistical pattern of plaque growth is observed. Aβ plaques exhibit a positively skewed size distribution, suggesting randomly distributed values on a log scale [30]. This pattern is consistent with a stochastic equilibrium model in which the growth rate of a porous deposit is proportional to its volume, resulting in a log-normal distribution. The interpretation of the cross-sectional observations as a reflection of true volumetric properties is supported by the near-spherical plaque geometry and by similar distributions observed in 3D reconstructions [30–32].

The relationship between plaque morphology, developmental pathways, growth dynamics, and neurotoxicity remains poorly understood, and this uncertainty extends to the functional role of the deposits themselves. While soluble Aβ oligomers are considered the primary neurotoxic species, the ultimate pathogenic, neutral, or even protective role of the various plaque types is still unresolved, leaving a critical gap in our understanding of AD progression. Nevertheless, the significance of senile Aβ plaques as indicative markers of the disease process is well-established [4,11,29].

1.3 Small-molecule probes for the detection of the Aβ-pathology[I.]

Accurate identification, delineation, and quantification of Aβ plaques within brain tissue are essential to understand the progression of the disease and assess the efficacy of potential therapeutic strategies. Fluorescent amyloid probes like ThioS, thioflavin T, and Congo red are widely used to detect Aβ plaques in AD [33–39]. While their binding mechanism lacks epitope-level specificity, these small-molecule dyes and their derivatives are the gold standard as a tool for investigating structural organization and amyloid polymorphism, as their general binding affinity allows them to recognize a broader spectrum of amyloid conformations than antibody-based methods [5,33,34,37]. Indeed, their strength lies in their remarkable versatility; beyond their foundational role in histology, their applications range from *in vitro* monitoring of aggregation kinetics, *in vivo* detection in animal models, to the molecular characterization of distinct Aβ binding sites [33,40,41].

Furthermore, they offer numerous practical advantages, including lower manufacturing costs, chemical stability, less demanding experimental protocols, and intrinsic fluorescence that eliminates the need for secondary conjugates. Their simpler structure and high chemical tractability also accelerate development timelines and facilitate the synthesis of derivatives with tailored properties [33,40–42]. In contrast, immunohistochemical approaches face several disadvantages: the large size of antibody molecules can impede diffusion into thicker, denser histological sections; they can exhibit structural instability and may also show non-specific binding (requiring extensive blocking,

permeabilization, or antigen retrieval steps); they frequently necessitate various pre-treatments and specialized methods to overcome these limitations [43]; and, crucially, they have limited accessibility to the densely packed, insoluble fibrils within compact plaque cores [44–47].

Regarding their potential for *in vivo* diagnostic imaging, antibody-based approaches are challenged by their generally limited blood-brain barrier (BBB) penetrability, as well as unfavorable pharmacokinetic properties and uptake-clearance mechanisms, although promising efforts are underway to develop them as radioligands [47–50]. In stark contrast, the diagnostic potential of small-molecule amyloid probes was realized with the development of Pittsburgh Compound B: a neutral, radio-labeled thioflavin T derivative that became the first successful agent for *in vivo* amyloid imaging via positron emission tomography, demonstrating the translation of a histological tool into a clinical diagnostic [42]. This breakthrough was followed by the development of a series of small-molecule tracers (e.g., florbetapir, florbetaben, and flutemetamol) that are now routinely used in clinical amyloid-imaging [5,40,51,52].

ThioS, a classic fluorescent probe for amyloid detection [35,37,53], is a mixture of several different compounds derived from the methylation of dehydrothiotoluidine, in contrast to the closely related and chemically pure thioflavin T [38]. While both dyes bind with high affinity to β-sheet-rich Aβ fibrils, their photophysical properties differ significantly, as ThioS binding does not produce the same characteristic spectral shift as thioflavin T, a property that can contribute to higher background (BG) [35,37,39]. Despite this, ThioS remains a cornerstone of conventional histology for labeling Aβ aggregates, exhibiting an intense green-yellow fluorescence with a peak emission at 455 nm under epifluorescence microscopy [35,37].

A key characteristic shared by most of these fluorescent probes is that they label both parenchymal (plaques) and vascular amyloid pathology (CAA); moreover, vascular elements themselves often exhibit significant intrinsic autofluorescence. In the following sections, we will refer to all microscopically detectable plaque types and pre-amyloid-like structures within the parenchyma as "parenchymal amyloid deposits". Prior efforts to distinguish these components have included approaches based on morphological criteria [54,55], time-consuming manual labeling procedures [56], as well as multiplex fluorescence labeling and co-localization [57], *in vivo* animal studies suggesting a potential for exploiting differential BBB permeability of amyloid probes [40], and the development of selective antibody fragments recognizing distinct epitopes [58]. However, these diverse approaches are often impractical for robust, large-scale analysis, being limited by their reliance on labor-intensive procedures, susceptibility to observer bias, need for specialized expertise, complex multi-component protocols, or substantial further development. Therefore, the development of robust and automated methods for the objective analysis of these complex pathological features is critical.

However, the implementation of such automated analysis pipelines for histological micrographs is fraught with significant technical challenges. High-resolution fluorescent imaging itself can introduce technical artifacts like illumination nonuniformity and BG fluorescence, which compromise the reliability and reproducibility of the analysis [59–67]. This is particularly evident in some conventional staining protocols; for example, varying ThioS procedures, typically involving high stain concentrations, short incubation times, and differentiation with solvents like ethanol, may lead to non-specific binding, particularly in blood vessels, as well as the loss of ThioS from low-affinity sites, potentially under-detecting subtle amyloid accumulation [35,36,53]. Finally, the marked diversity of Aβ plaques across stages and regions makes robust segmentation especially cumbersome. These issues complicate not only the segmentation of deposits but also the subsequent morphometric analysis required for quantitative neuropathology.

1.4 Machine learning and neural networks in biomedical applications[I]

Artificial intelligence (AI) is a broad, interdisciplinary field of computer science that integrates engineering and data analysis to design technological systems (intelligent machines) capable of performing tasks that typically require human intelligence (e.g., autonomous problem-solving, logical reasoning, planning, and both linguistic and visual perception) [68–70]. Historically, the field evolved from classical, symbolic systems that relied on explicit logic or knowledge bases (rule-based and expert systems), and statistical methods focused on probabilistic modeling, heuristic search, and optimization (searching and evolutionary algorithms) to a data-driven approach: machine learning (ML). As the definitive modern subfield of AI, ML represents a paradigm shift towards automated pattern recognition directly from data, a process based on a model fitting procedure without explicit programming, where parameters are optimized on a given dataset (experience) to improve predictive performance on a specific task [68–72].

AI and ML models are transforming biomedical research and development; while their clinical role remains primarily supportive, they are already applied across a wide spectrum of modalities in key areas such as diagnostics, prognostics, decision-making, treatment optimization, and patient monitoring [73–75]. However, their widespread adoption faces critical hurdles: the scarcity of high-quality, large-scale, and representative datasets and the corresponding expert annotations; the interpretability challenges of "black-box" models; and profound ethical concerns regarding data privacy and diagnostic responsibility [74]. ML algorithms are categorized into learning paradigms:

- In supervised learning, a model learns a mapping function f_θ: $\mathbb{R}^d \rightarrow \mathcal{Y}$ from input features $\boldsymbol{x}_i \in \mathbb{R}^d$ to known output labels $\boldsymbol{y}_i \in \mathcal{Y}$ using a labeled dataset $\mathcal{D} = \{(\boldsymbol{x}_i, \boldsymbol{y}_i)\}_{i=1}^N$. The goal is to minimize a loss function $\mathscr{L}\left(f_\theta(\boldsymbol{x}_i), \boldsymbol{y}_i\right)$ to achieve accurate predictions on new, unseen data (generalization).

The two primary tasks are classification (predicting discrete categories) and regression (predicting continuous values). Supervised models range from classical linear models (e.g., linear and logistic regression) and probabilistic classifiers (e.g., naive Bayes, perceptron), through instance-based "lazy" learners (e.g., k-nearest neighbors), and interpretable, rule-based decision trees, to more complex kernel-methods (e.g., support vector machines) and ensemble techniques (e.g., random forest, gradient boosting) [76–77]. Biomedical applications are dominated by the automated analysis of imaging data (e.g., histological slides, radiological scans) for detecting, segmenting, and classifying anatomical structures, tissues, cell types, and pathologies. This also extends to predictive modeling using structurally diverse clinical, demographic, and epidemiological data (e.g., electronic healthcare records, prescriptions, lab reports, and medical notes) to forecast outcomes (e.g., disease risk, patient trajectories, biomarker levels, and pandemic spread), or to develop triage systems and manage hospital resources. Furthermore, physiological signals (e.g., from sensors and clinical devices) are leveraged for real-time patient monitoring, alongside omics and pharmacological data for molecular simulations, drug discovery, and precision medicine [78–80].

- In contrast, unsupervised learning seeks to uncover hidden structures and correlations in unlabeled datasets $\mathcal{D} = \{\boldsymbol{x}_i\}_{i=1}^{N}$ by fitting a model f_θ that optimizes an internal criterion. Key tasks include clustering (grouping data, e.g., k-means, density-based spatial clustering of application with noise, Gaussian mixture models), dimensionality reduction (finding informative representations, e.g., principal component analysis (PCA) and factor analysis for linear structures, and autoencoders or manifold learning like t-distributed stochastic neighbor embedding and uniform manifold approximation and projection for nonlinear ones), association rule mining (e.g., apriori algorithm, frequent pattern growth), and density estimation, enabling complex applications like anomaly detection, generative modeling, and preprocessing for supervised algorithms [81–83]. In medicine, these tasks translate to analyzing high-dimensional multi-omics profiles or sequences (genetic, proteomic, transcriptomic) to stratify patients, subtype diseases, identify biomarkers, and explore patient-specific drug responses for tailored treatments; and detecting subtle pathologies (e.g., tumors, lesions) through anomaly detection in medical imaging [84].
- In reinforcement learning, an agent learns an optimal policy for a sequential decision-making process by interacting with an environment, maximizing long-term cumulative reward for its actions through trial-and-error, a process typically formalized as a Markov decision process. Methods are categorized as model-based (learning environment dynamics, e.g., Dyna-Q) or model-free, which can be value-based (learning the value of states or actions, e.g., Q-learning, State-Action-Reward-State-Action), policy-based (directly optimizing the policy, e.g., REINFORCE), or hybrid actor-critic

architectures (e.g., proximal policy optimization) [85,86]. By optimizing sequential decision-making, this paradigm shapes adaptive treatment strategies. While safety constraints limit direct exploration, it excels at optimizing interventions using large, pre-existing datasets from critical care (e.g., sedation, ventilation) and developing dynamic treatment regimens for chronic conditions (e.g., drug dosing, combination therapies), with emerging applications in robotic-assisted surgery and clinical trial design [87].

- The scarcity of high-quality, annotated data has blurred classical paradigm boundaries, giving rise to a spectrum of data-efficient strategies. This includes semi-supervised learning (leveraging a mix of labeled and unlabeled data, e.g., pseudo-labeling); weakly supervised learning, central to this dissertation, (multi-instance learning or usage of inexact, incomplete, and inaccurate supervisory signals, e.g., image-level tags for a pixel-level segmentation); active learning (iterative human-in-the-loop process); and self-supervised learning (generating its own supervision via pretext tasks), such as masked modeling (e.g., bidirectional encoder representations from transformers, masked autoencoders) and contrastive learning (e.g., simple framework for contrastive learning of visual representations, contrastive language-image pre-training) [88–92]. A highly effective practice that leverages existing representations is transfer learning (pre-training on a large dataset and fine-tuning on a task-specific one, e.g., multi-task learning, domain adaptation); a principle abstracted further by meta-learning ("learning to learn"), which trains models for rapid adaptation to new tasks from few examples (few/one/zero-shot learning) using metric-based (e.g., Siamese networks) or optimization-based (e.g., model-agnostic meta-learning) methods [88–92]. Biomedical applications include driving computer-aided diagnosis via minimally-assisted annotation of biological structures; accelerating drug discovery and molecular biology extracting omics-derived predictions (e.g., functions, affinities, associations) to automate drug-activity prediction and targeted experiments; and refining clinical data analysis by harnessing raw text for biomedical mining (e.g., named entity recognition and indexing) and for supported labeling of electronic health records to enable patient clustering and diagnostic classification [91,92].

Artificial neural networks (ANNs), a class of neuro-inspired mathematical models, have become a cornerstone of modern ML due to their remarkable flexibility and broad applicability across learning paradigms. Their contemporary application is dominated by deep learning (DL), which utilizes multiple hidden layers (> 1) or long differentiable causal chains (credit assignment path > 2) to learn hierarchical representations by progressively building abstract concepts from low-level patterns [68,70,93]. While the universal approximation theorem posits that a single, sufficiently wide hidden layer possesses arbitrary approximation capabilities, depth confers an exponential advantage in representational efficiency, leading to far superior performance on complex tasks compared to shallow

models [94–97].

While its conceptual precursor was the binary McCulloch-Pitts model (1943) [98], the modern artificial neuron differs fundamentally through its use of differentiable activation functions, which is an essential prerequisite for gradient-based learning. Drawing a simplified analogy to biological nervous systems, each artificial neuron (or node) acts as a computational unit that receives inputs from other units and calculates its activation value based on them [98–101]. This operation can be interpreted as a simplified model of biological neuron function, wherein the inputs, x_i, are abstractions of the signals integrated via synapses from other neurons; the trainable weights and bias, w_i and b, are parameters that model synaptic strengths and an internal, tunable firing threshold, respectively; and the nonlinear activation function, ϕ, represents the continuous-time variations of the dynamic firing rate of a biological neuron with a single, instantaneous, static value. Without nonlinearity, a model has limited expressiveness, as pure sequences of linear operations collapse into a single linear transformation [102–104].

Mathematically, a neuron computes a composition of an affine transformation, in which a bias term is added to the dot product of the inputs and weights, $z = \sum_i w_i x_i + b$, followed by an element-wise nonlinear activation, $y = \phi(z)$, using an activation function such as Sigmoid: $\phi(z) = \frac{1}{1+e^{-z}}$, Tanh: $\phi(z) = \tanh(z)$ or rectified linear unit (ReLU): $\phi(z) = \max(0, z)$. [105–108] The operation of an entire layer containing m such neurons can thus be described in a compact matrix form as $\boldsymbol{y} = \phi(\boldsymbol{W}\boldsymbol{x} + \boldsymbol{b})$, where $\boldsymbol{W} \in \mathbb{R}^{m \times d}$ is the weight matrix, $\boldsymbol{b} \in \mathbb{R}^m$ is the bias vector, $\boldsymbol{x} \in \mathbb{R}^d$ is the input vector, and $\boldsymbol{y} \in \mathbb{R}^m$ is the output vector of the layer [105,106]. In a simple feedforward architecture, neurons are organized into layers, with the transformation from layer l - 1 to layer l defined by the equation $\boldsymbol{h}^{(l)} = \phi(\boldsymbol{W}^{(l)}\boldsymbol{h}^{(l-1)} + \boldsymbol{b}^{(l)})$, where $\boldsymbol{h}^{(l)}$ denotes the activation vector of the l-th layer. The entire function for a network with a total of L layers is the mathematical composition of these individual layers $(f_1, f_2, \ldots, f_L)$, where each function f_l represents the transformation for the l-th layer: $f(\boldsymbol{x}) = f_L \circ f_{L-1} \circ \cdots \circ f_1(\boldsymbol{x})$ [105–109]. This concept of layered representations is also inspired by biology, presenting a functional (rather than anatomical) analogy to certain aspects of cortical organization [101,102–104]. However, the main goal of modern ANNs is not to model the brain with biological accuracy, but to create efficient function approximation machines for statistical generalization grounded in engineering and mathematical principles [102–104]. The training of these models is typically performed in an end-to-end fashion, where the mapping function is learned through an iterative process of minimizing a loss function ($\mathscr{L}$), which quantifies the discrepancy between model predictions and true values [100,102]. This optimization is predominantly performed via gradient descent, which updates parameters in the direction opposite to the loss gradient, with the update magnitude

controlled by the learning rate (η), as per the rule $\Delta w_i = -\eta \frac{\partial \mathscr{L}}{\partial w_i}$, using gradients calculated efficiently by the backpropagation algorithm, a recursive application of the chain rule implemented via dynamic programming that propagates an error term ($\boldsymbol{\delta}^l$) backward through the network: $\boldsymbol{\delta}^l = [(\boldsymbol{W}^{l+1})^{\mathrm{T}}\, \boldsymbol{\delta}^{l+1}] \circ \phi'(\boldsymbol{z}^l)$ [93,100,105]. After training, the model is expected to generalize by making predictions on unseen examples; its development can be monitored on a validation set, while final performance is evaluated on a held-out test set (e.g., using train-test splitting or k-fold cross-validation) [105–108].

These foundations have given rise to the specialized architectures that dominate the field today, such as dense, feedforward multi-layer perceptrons (MLP), convolutional neural networks (CNN), recurrent neural networks (RNN), graph neural networks (GNN), and transformers, which, originating in domains like computer vision (CV) and natural language processing (NLP), now represent the forefront of multimodal learning [105,109]. In biomedical context, these ANN architectures can be used to analyze diverse data types from a wide array of sources: MLPs identify non-linear relationships in scalar data (individual numeric values) to diagnose conditions and predict physiological features (e.g., biomarker concentrations, physiological parameters); CNNs dominate biomedical image analysis, enabling detection, pixel-precise segmentation, and quantification (e.g., pathologies, histological structures, and biomarkers), with generative models providing image synthesis (e.g., cross-modality transformation, registration, and augmentation); RNNs use internal memory states to process sequential data (temporal or ordinal dependencies) for prognostic tasks (e.g., disease progression, readmission risk) and physiological signal reconstruction (e.g., electrocardiogram, time-series biomarkers); and GNNs leverage topological and contextual information to analyze graph data (e.g., biomarker identification, molecular or gene interaction analysis, clinical outcome prediction, tissue-level relationships in imaging) [110,111].

1.5 Computer vision: Overview[I]

CV is an interdisciplinary field that seeks to replicate and automate the capabilities of the human visual system by transforming raw, multi-dimensional sensor data (e.g., digital images, videos, point clouds) into high-level semantic understanding via sophisticated algorithmic models. Modern CV approaches are deeply integrated within the broader framework of ML, particularly DL, leveraging advanced algorithms to analyze vast quantities of visual information and enabling a wide array of applications, including object recognition, localization, segmentation, scene understanding, event detection, and generative modeling [112–115].

Before the CNN revolution, CV was governed by different, fragmented paradigms of manually designed, problem-specific algorithms; it typically relied on encoding prior knowledge and heuristics

into a rigid, two-phase pipeline that separated handcrafted feature extraction from statistical approaches [112,116,117]. The feature extraction phase involved several parallel directions: early approaches, inspired by signal processing, extracted primitive elements like edges (e.g., Canny, Sobel operators), corners (e.g., Harris detector), and textures (e.g., Gabor filter banks with representations similar to those observed in the visual system), while another direction used variational methods to frame higher-level tasks as energy minimization problems (e.g., active contours segmentation or "snakes") [112,117–124]. However, with the rise of ML, the focus shifted to developing robust, invariant feature descriptors for pattern recognition, epitomized by algorithms like the scale-invariant feature transform and histogram of oriented gradients, which were designed to create discriminative "fingerprints" of local image regions, providing invariance to scale, rotation, and illumination [125–129]. In the second phase, these high-dimensional descriptors were aggregated into a fixed-size feature vector, often via the "bag of visual words" model, then input to classical statistical learning algorithms like the support vector machine. The fundamental limitation of this era was its bottleneck: the expressive power of the handcrafted features, which necessitated a shift towards an end-to-end, data-driven representation learning paradigm [125–132].

CNNs are a specialized class of ANNs designed to process grid-like data, such as images. In stark contrast to the naive application of dense MLPs to images, which suffers from a combinatorial explosion of parameters and the loss of spatial topology, CNNs are built on more efficient computational principles, introducing potent, neurobiologically inspired inductive biases [68,133–136]. Their conceptual origins trace back to Hubel and Wiesel's seminal research [137] on the hierarchy of the visual processing (simple and complex cells), a model first operationalized by Fukushima's Neocognitron [138] and later made successful by LeCun's LeNet-5 [139]. CNNs achieve remarkable parameter efficiency through two core principles: sparse connectivity and weight sharing. Mimicking biological receptive fields, sparse connectivity means each neuron connects only to a small, local region of the preceding layer. Weight sharing applies the same set of weights (filters or kernels), where each kernel $\boldsymbol{K} \in \mathbb{R}^{h \times w \times C}$ is applied across the entire input $\boldsymbol{I} \in \mathbb{R}^{H \times W \times C}$ (formalizing that a feature detector is useful everywhere), which drastically reduces parameters and builds translational equivariance into the model [68,133–136]. The fundamental building block of a CNN consists of a discrete convolution (more precisely, cross-correlation: $(\boldsymbol{I} * \boldsymbol{K})(i, j) = \sum_m \sum_n \sum_C I(i + m, j + n, c) K(m, n, c)$), non-linear activation (e.g., ReLU), and a local pooling operation like max pooling ($y_j = \max_{i \in N_j} x_i$). The pooling layer aggregates equivariant feature maps to push the representation towards translational invariance. Stacking these blocks creates a deep, hierarchical representation that functionally models the visual cortex, where the network learns to compose simple, low-level features (e.g., edges,

textures) from initial layers into progressively more abstract, high-level concepts (e.g., objects) in deeper layers. A typical classifier architecture concludes with dense (fully connected, FC) layers that process the vectorized feature maps for the final prediction [68,133–136]. This end-to-end paradigm became dominant after the 2012 ImageNet Large Scale Visual Recognition Challenge victory of AlexNet [140], a breakthrough driven by the convergence of deep architectures, massive GPU parallelization, the ReLU activation, and novel regularization techniques like dropout and augmentation. The success of AlexNet spurred a rapid evolution of increasingly deep and sophisticated backbone architectures, including the uniform structures of VGGNet [141] and ResNet [142] with its gradient-addressing skip connections. These backbones then underpinned complex CV tasks like object detection, which branched into two-stage, high-accuracy methods (e.g., Faster R-CNN) and single-stage, real-time approaches (e.g., You Only Look Once); and semantic segmentation, where encoder-decoder models like the U-Net [143] became the standard in biomedical imaging [133–136].

The main limit of CNNs lies in their rigid, local receptive fields inherently incapable of modeling long-range, global dependencies without a prohibitively deep hierarchy. This issue was directly addressed by the transformer architecture, a paradigm shift originating from NLP that challenges the decade-long hegemony of CNNs in CV. While CV was mastering spatial hierarchies, NLP had concurrently evolved to understand sequential context, moving from RNNs (e.g., long short-term memory, gated recurrent unit) towards the transformer [144–146]. Although the two fields had long, symbiotic relationship (e.g., 1D CNNs for text, RNNs for image captioning), this evolution culminated in the revolutionary (multi-head) self-attention mechanism, a radical departure from recurrent or convolutional structures, creating a dynamic, data-dependent global receptive field by allowing every element in an input sequence to attend to every other. Its mathematical foundation is the scaled dot-product attention: $\mathrm{Attention}(\boldsymbol{Q}, \boldsymbol{K}, \boldsymbol{V}) = \mathrm{softmax}(\frac{\boldsymbol{Q}\boldsymbol{K}^{\mathrm{T}}}{\sqrt{d_k}})V$, where $\boldsymbol{Q}$, $\boldsymbol{K}$, and $\boldsymbol{V}$ represent the query, key, and value matrices, respectively [144–146]. The vision transformer [147] successfully adapted this model to CV by treating an image as a sequence of fixed-size patches, which are then linearly embedded into tokens analogous to words. The success of vision transformer on large-scale datasets demonstrated that the strong inductive biases of CNNs (e.g., locality) are not indispensable, as a more general, sequence-based model can learn these properties directly from data. However, the extremely data-hungry "tabula rasa" nature of transformers and the continued efficiency of CNNs on smaller datasets spurred the development of hybrid solutions aiming to combine the best of both worlds [147,148]. These include using convolution for low-level feature extraction, reintroducing a hierarchy by shifted-window self-attention (e.g., swin transformer), and augmenting CNNs with lightweight attention-like modules (e.g., convolutional block attention module, squeeze-and-excitation, attention

U-Net) [149–152].

The primary application of DL models in the biomedical domain is the comprehensive analysis of a wide spectrum of imaging data, spanning the segmentation and classification of anatomical, tissue-level, cellular, or pathological structures from a diverse array of sources and modalities. This includes large-scale radiological data (computed tomography, magnetic resonance imaging, X-ray, ultrasound), high-resolution microscopic and optical data (histopathological slides, endoscopy-colonoscopy; and ophthalmology sources like optical coherence tomography and color fundus photography), and functional or interventional data (single photon emission computed tomography, invasive coronary angiography). Beyond direct structural analysis, these models also enable advanced methodological applications such as human-in-the-loop interactive segmentation, image registration, synthesis, and cross-modality transformations for data augmentation, and biomarker quantification [153,154].

While these advanced architectures have yielded exceptional performance, their practical utility is constrained by a key bottleneck: a profound dependency on vast, meticulously annotated data. This dependency causes critical challenges, like mitigating overfitting, ensuring robustness against unseen distributions, and addressing the pervasive issues of data scarcity (quantity) as well as imbalance and limited representativeness (quality) [155–160]. These hurdles are particularly acute in high-stakes, annotation-heavy domains like histology and medical imaging, where creating granular ground truth (GT) requires immense resources, time investment, and specialized domain expertise [153,154]. In response, the research focus has shifted towards a suite of complementary, data-efficient strategies [155–160].

Data augmentation expands the dataset by generating synthetic yet plausible exemplars, thereby increasing dataset size, representational richness, and fidelity to the real-world distribution. Consequently, it has evolved from an auxiliary technique into a core component of modern DL frameworks, acting as a powerful regularizer to improve model robustness and generalization [155–158]. In CV, input-space augmentations are often classified as classical or advanced. Classical methods include a wide array of geometric transformations (e.g., rotation, translation, shearing, warping, and non-linear elastic deformations), photometric alternations (e.g., brightness changes, color jittering), and pixel-level conversions (e.g., random noise addition, application of image filters) [156,157]. Advanced strategies involve complex manipulations, such as image-mixing and regional erasure [161]. A pioneering mixing technique, MixUp [162], linearly interpolates between images and their labels, a concept that spawned derivatives like Manifold Mixup [163] and patch-based extensions such as CutMix [164]. Subsequent advancements include strategies for mixing one or more samples at a pixel- or patch-level to enhance generalization, alongside techniques that improve plausibility by either using

saliency and activation maps for guidance or refining the boundaries of combined regions for a seamless blend [161]. Another advanced strategy employs generative models, which learn the underlying data distribution to sample entirely new, synthetic training data. The evolution of these models from variational autoencoders and generative adversarial networks to state-of-the-art diffusion models (e.g., DALL-E 3, Midjourney) and generative pre-trained transformer series has enabled the synthesis of high-fidelity, photorealistic images, also offering a powerful tool for dataset expansion [165]. In the biomedical domain, these strategies are critical to address: strict legal and ethical constraints on data acquisition; the immense variability of the data itself, spanning both sample properties (e.g., high intra- and low inter-class variance, scarce controls, normal anatomical variations, disease rarity) and diverse imaging modalities (e.g., technical differences, domain shift, and domain-specific data types like 3D volumes); and the significant bottleneck of costly, expert annotation [166–168].

Beyond data augmentation, a second pillar of data-efficient strategies involves leveraging alternative forms of supervision. By generating training signals from unlabeled data, self-supervised learning has become a cornerstone of representation learning, redefining the transfer learning paradigm; while supervised pre-training on datasets like ImageNet was the standard, modern foundation models are built upon the resulting robust representations, enabling new capabilities like zero-shot learning and culminating in powerful multimodal systems. Semi- and weakly supervised methods aim to leverage small amounts of labeled data or cheaper, inexact/incomplete/inaccurate labels, respectively [88–92,159]. Weakly supervised object localization and semantic segmentation (WSOL and WSSS) with image-level labels bridges the gap between expensive pixel-level annotation and weak labels by following a two-stage process: first, a classifier generates coarse localization maps extracting implicit information (e.g., saliency maps; class activation maps, CAMs [169]; attention maps), which are then post-processed and/or used as pseudo-masks to train a dedicated segmenter [159]. The inherent coarseness of these initial maps, compounded by the architectural biases of CNNs, poses a significant challenge, often resulting in issues akin to imperfect or noisy supervision [160]. Boundary recovery mitigates this issue by acting as a refinement step that sharpens class transitions and aligns the coarse segmentation with underlying image contours [160]. Refinement strategies include using superpixels or conditional random fields [160,170–172]; architectural solutions like multiscale feature fusion [173]; training-based approaches like using boundary-aware loss functions [174,175,143], exploiting multiple annotation candidates [176], and applying spatially structured soft labeling techniques [177–180].

Consequently, alternative supervision approaches are increasingly applied in biomedical imaging to localize and segment target structures from weak labels [171,173,181–193]. Separately, localization maps from classification models serve as vital interpretability tools, enabling experts to visualize

and validate predictive evidence to address the 'black-box' problem [194–203]. Both data-efficient learning and model transparency are critical for advancing research in high-impact areas, such as the analysis of neuropathological features in AD [204–207].

1.6 Supplementary context for collaborative studies[II., III.]

1.6.1 Cellular morphology as an indicator of microglial activation[II.]

Microglial cells are the resident macrophage-like cells of the central nervous system, acting as its primary immune sentinels [208,209]. The morphology of microglia is highly plastic and serves as a key indicator of their functional state; under physiological conditions, they typically display a resting, ramified morphology with fine, motile processes for monitoring the microenvironment. From this surveillant state, they could transform into simplified activated forms in response to injury or inflammatory signals, such as those induced by lipopolysaccharide (LPS), a shift associated with effector functions like phagocytosis and cytokine release [210–214]. Previous studies conducted both *in vivo* and *in vitro* had established that N-(2-(dimethylamino)ethyl)-3-(morpholinomethyl)-4-hydroxyquinoline-2-carboxamide (SZR104), a synthetic, brain-penetrable analog of the endogenous metabolite kynurenic acid (KYNA), exhibits broad anti-inflammatory properties, including the inhibition of phagocytosis and the downregulation of inflammatory marker protein expression levels [215–217]. However, the precise cytomorphological changes underlying these well-documented anti-inflammatory effects of SZR104 have not been quantitatively characterized, creating a significant research gap that warrants a comparative microscopic analysis of microglial morphology under different experimental conditions related to their activation characteristics. Addressing this gap requires a computational image analysis specifically for immunofluorescence micrographs of SZR104-treated microglial cell cultures, in order to objectively quantify and statistically compare the set of well-established morphological parameters previously described for characterizing microglial activation states [218,219].

1.6.2 Autophagy regulation in microglia under different activation states[III.]

Autophagy is a critical cellular homeostatic process that prevents cell damage through the clearance of harmful cytoplasmic material by forming autophagosomes, which fuse with lysosomes to degrade these components via resident hydrolases [220,221]. As a central element of the innate immunity in the central nervous system, microglial activation is a hallmark of neuroinflammation and neurodegenerative diseases; beyond the initial protective role of these microglial responses, excessive pro-inflammatory activity is increasingly recognized as a pathogenic factor [208,222]. Autophagy and inflammation exhibit a bidirectional molecular relationship, with their pathways intersecting at key regulatory molecules such as sequestosome 1 (p62/SQSTM1) [223–225]. The cellular levels of p62/SQSTM1 cargo protein generally correlates inversely with autophagic activity, as p62/SQSTM1

itself is degraded by the process, decreasing upon autophagy induction accumulating upon autophagy inhibition [226–228], it serves as a crucial marker for monitoring autophagic dynamics, and it also can be detected as discrete intracellular puncta [225,227]. Investigating the effects of various stimuli, such as the pro-inflammatory LPS [229,230] and anti-inflammatory drugs like rosuvastatin (RST) [231–235], on microglial cultures provides insight into differences of the autophagy regulation during homeostatic and critical conditions. The use of cellular autophagy inhibitors like the ionophore macrolide antibiotic bafilomycin A1 (BAF), which blocks autophagosome-lysosome fusion through V-ATPase inhibition, is a common strategy to study the dynamics of the autophagy pathway *in vitro* [236–238]. Beyond the measurement of the marker protein levels, accurate identification and counting of the p62/SQSTM1-positive puncta per cell from immunofluorescent images is a crucial step in related investigations.

2. Aims of the study

A. The primary aim of this study was to develop and validate a novel, two-stage WSSS framework for the accurate and automated pixel-level segmentation of ThioS-positive amyloid plaques from human brain histology micrographs. The central hypothesis was that inexpensive, rapidly generated, image-level labels (presence/absence of pathology) are sufficient to train a DL pipeline capable of producing high-fidelity segmentations, thereby circumventing the major bottleneck of costly and labor-intensive manual annotation in quantitative neuropathology. To this end, the following specific objectives were established:

1. To implement a robust image preprocessing and intensity correction pipeline to mitigate common fluorescence microscopy artifacts ensuring data integrity for downstream tasks.
2. To train a lightweight classifier (SqueezeNet), optimized with a thresholded average pooling (TAP) layer, to generate robust, high-resolution CAMs that serve as coarse spatial localization priors from the weak, patch-wise image labels.
3. To develop a sophisticated, on-the-fly data generation process that leverages these CAM-derived priors for an advanced object-level augmentation strategy, including creating object and BG scene databanks; and integrating a contour perturbation technique with a soft-copy and soft-paste (Soft-CP) blending method to generate a diverse and anatomically plausible training set.
4. To train a canonical segmentation network (U-Net) exclusively on these synthetic pseudo-labeled exemplars for the final, pixel-level refinement into precise object masks.
5. To rigorously validate the end-to-end performance of the complete WSSS framework against manually annotated, dense GT masks using a stringent, patient-wise cross-validation scheme to assess the generalization capabilities of the model to unseen individuals.

B. As a secondary, exploratory aim, the study sought to demonstrate the practical utility of the segmentations by performing a comprehensive, object-level morphometric analysis to investigate differences in plaque morphology across cortical regions and dementia statuses.

C. Furthermore, this dissertation includes methodological contributions to two collaborative, co-authored studies, with the following objectives:

1. The development of a morphometric profiling workflow to objectively quantify changes in the anti-inflammatory phenotype of cultured microglia.
2. The creation of a puncta-counting pipeline to accurately assess autophagy modulation by quantifying p62/SQSTM1-positive autophagosomes within individual microglial cells.

3. Materials and methods

3.1 Human brain tissue samples and ethical declaration[I.]

The human brain tissue samples used in this study were obtained from the Netherlands Brain Bank (Nederlandse Hersenbank/Netherlands Institute for Neuroscience, Meibergdreef 47, 1105 BA Amsterdam, The Netherlands). All tissue samples were collected from donors for or from whom a written informed consent for brain autopsy for research purposes had been obtained, and permission was granted for the use of tissue samples and for the anonymous use of clinical information. The study was approved by the local ethics committee and conducted in accordance with the Declaration of Helsinki (Project ID: 598/2009). The paraffin-embedded tissue sections originated from the parietal and temporal cortices (or subfields of these regions) of elderly subjects diagnosed with AD and age-matched, non-demented controls. All samples were supplemented with anonymized clinical and pathological information; some of these are included in Publication I./Supplementary Table S6.

3.2 Image acquisition and preprocessing[I.]

For the present study, 7–8 μm thick paraffin-embedded brain sections were utilized [239]. Following an initial screening of available brain regions and cases, our work was focused exclusively on the superior temporal and parietal gyri of seven individuals, as only these areas provided sufficient quantity and quality of ThioS-positive parenchymal amyloid structures for the analysis. The final dataset comprised a total of fourteen sections (one from each region per case), representing the two distinct experimental groups of cases: non-demented (Braak 2) and advanced AD (Braak 5–6).

The prepared brain sections were stained with the amyloid-fibril-binding fluorescent dye ThioS to visualize plaques and other deposits [35–37], following a histological protocol based on the Krutsay method [53]. Prior to staining, sections underwent deparaffinization using cyclohexane isomers of xylene (3 × 15 min), were washed in absolute ethanol (3 × 2 min), and subsequently rehydrated through a descending ethanol series (96%, 70%, and 50% for 1 min each) before a final rinse in

distilled water. The rehydrated sections were then completely immersed in a freshly filtered 1 g/10 mL aqueous ThioS solution (Reanal, Budapest, Hungary) for 10 minutes at room temperature. Following a brief differentiation step in alcohol and a subsequent rinse in distilled water, the sections were coverslipped with an aqueous mounting medium (Vectashield, Vector Laboratories, Peterborough, UK). To minimize photobleaching and preserve signal integrity, all stained slides were stored in dark, refrigerated conditions (4°C) and imaged within two weeks.

High-resolution digital micrographs were acquired using a Leica DMLB epifluorescence microscope (Leica Microsystems CMS GmbH, Wetzlar, Germany) equipped with an apochromatic objective (40×/0.75 ∞/0.17), a Leica DFC7000 T CCD camera, and LAS X Leica Application Suite X computer software (version 3.9.28093.0) (Leica Microsystems CMS GmbH, Wetzlar, Germany). Images of the amyloid deposits were captured in the green channel with a fixed exposure time of 45 ms and saved as 1920 × 1440 pixels (75 dpi) TIFF files, each embedded with a scale bar, with care taken to minimize spatial overlap during the systematic acquisition process.

A reliable quantitative analysis of the acquired histological micrographs necessitated a robust preprocessing pipeline to correct for two primary sources of fluorescence imaging artifacts: uneven illumination (i.e., vignetting or radial intensity gradient) and BG noise from complex sources (out-of-focus fluorescence from adjacent tissue planes, electronic noise from the detector, stray light within the optical path, and endogenous tissue autofluorescence), both of which can significantly compromise downstream segmentation and morphometric analysis [60–62]. While conventional prospective methods like flat-field correction (white referencing) are well-established, their reliance on precisely replicated reference images for normalization, often in conjunction with shutter-closed dark-frame subtraction to model sensor-specific dark current, makes them impractical for many biological applications (often infeasible due to factors such as inconsistencies in the histological workflow, device anomalies and sample-specific chemical environments) [60,61,63]. Consequently, retrospective methods, which estimate the bias directly from the acquired images, offer a more robust alternative. These range from simpler, single-image techniques like pseudo-flat-field correction (which rely on the assumption of a near-uniform signal distribution across the image [61]) to more sophisticated multi-image strategies that generate an illumination correction function (ICF) by averaging multiple images and subsequently smoothing the result (e.g., with a large-kernel median filter) to produce a robust approximation for normalization [60,61,63–65]. Similarly, standard intensity thresholding (e.g., Otsu thresholding) [66] or morphological operations-based (e.g., "rolling ball" algorithm with size-based structuring element) [67] BG correction methods often fail on micrographs with overlapping foreground (FG) and BG intensity distributions and high object-size heterogeneity [59]. More advanced statistical approaches, like the Silver Mountain Operator (SMO) [59] provide a robust

solution by directly restoring an unbiased and representative subset of the BG pixel distribution from the image itself. It employs a robust statistical procedure to select a set of BG pixels; the core of the algorithm involves simple mathematical operations, computing a moving average (the single parameter is the size of the kernel) over the normalized intensity gradients, followed by the extraction of their magnitudes.

Our work implements a two-stage correction pipeline that adapts and combines these robust techniques from the literature (Figure 1A). First, to address uneven illumination, a multi-image ICF was generated by averaging 45 selected micrographs with predominantly clear tissue areas, which was then refined using Gaussian blur and median filtering to isolate the low-frequency gradients and produce a robust approximation of the illumination non-uniformity [60,64,65]. Each micrograph was subsequently corrected via pixel-wise division by this ICF and scaled by the global spatial average of the ICF. Second, for BG estimation, we employed the SMO [59] configured with a 7-pixel averaging window and a 5^{th} percentile threshold, without prior smoothing. Calculation was constrained to image regions excluding saturated (≥ 255) or empty (≤ 5) pixels. The per-image median of the estimated BG distribution was then subtracted from the entire unmasked image area, and the entire set of corrected images was collectively rescaled to a global 0–255 grayscale range and saved as 8-bit TIFF files.

Following the image-wide intensity adjustments, the corrected micrographs served as the foundation for a two-tiered annotation and dataset curation strategy designed for our WSSS framework by the generation of two distinct types of labels for training and evaluation.

The primary dataset for model training was generated via a systematic patch extraction process using ImageJ (v1.47). A total of 6329 square regions of interest (ROIs) of 800 × 800 pixels, a size chosen to reflect the heterogeneous plaque size and density, were manually cropped from the 1607 original micrographs (1920 × 1440), aiming to minimize spatial redundancy, although complete non-overlap was often impractical. Each extracted patch was then assigned a weak, image-level binary label: '1' for the presence of visible ThioS-positive parenchymal pathology, and '0' for its absence. To ensure anatomical diversity and balanced representation, positive and negative patches were systematically extracted from both investigated brain regions for each of the 7 subjects, resulting in a final training set of 2978 positive and 3350 negative patches. This rapid, coarse-grained annotation strategy was underpinned by a key design choice to ensure model robustness: by defining the negative class solely by the absence of parenchymal deposits, confounding structures such as vascular amyloid and staining artifacts were intentionally included in both classes. This forces the model to learn the specific features of parenchymal plaques as the sole discriminative signal, preventing it from learning spurious correlations.

The central hypothesis of this work is that such weak, image-level labels are sufficient for training

a WSSS framework to extract precise, pixel-level object masks dramatically accelerating large-scale pathological data collection and subsequent quantitative analysis. For the final, independent evaluation of the complete WSSS pipeline, a secondary, dense GT dataset was meticulously created. In contrast to the initial patch-level weak labels used for training, this involved a labor-intensive, semi-automated ImageJ-based process to generate precise, pixel-level binary segmentation masks for the entire, uncropped micrograph dataset. These masks, created with extensive manual oversight (e.g., visual inspection, fine-grained adjustments), were reserved exclusively for the final validation stage and were not used during training. Their sole purpose is to serve as the benchmark for the final evaluation, where the full-image segmentation maps, reassembled from the patch-level predictions, are directly compared against these GT masks using a comprehensive set of standard segmentation metrics.

The computational workflow for all preprocessing and correction stages was implemented in Python (v3.10), leveraging standard scientific libraries (NumPy and OpenCV) [240–242], alongside the specific SMO Python package (https://github.com/maurosilber/smo) [59]. All intensive computations were executed within the Google Colaboratory cloud environment (https://colab.research.google.com) [243]. The manual annotation tasks, encompassing both the weak patch-level labeling and the dense pixel-wise segmentation, were conducted using ImageJ (v1.47) (https://imagej.net/ij/docs/guide/user-guide.pdf) [244].

3.3 Deep learning models and experimental setup[I.]

3.3.1 Overview: Architectures and methodological design[I.]

While DL has significantly advanced medical image segmentation, its reliance on costly, dense pixel-level labels remains a major bottleneck. Weakly supervised pipelines, which leverage inexpensive image-level labels, offer a pragmatic alternative. The core of our study is a WSSS approach designed to progress from weak, image-level labels to precise, pixel-level segmentation masks. The overall logic of this approach involves two distinct DL models operating in sequence. First, a lightweight classification network is trained on image-level binary labels to identify the presence or absence of parenchymal amyloid pathology. This classifier is then used to generate CAMs, which provide a coarse spatial localization of the discriminative features. These CAMs serve as the source for generating noisy but informative pseudo-labels, which, following an advanced dynamic augmentation process, are used to train a second, powerful segmentation network for refinement, a U-Net, tasked with producing the final, high-fidelity pixel-wise object masks.

A foundational technique in this domain is the CAM method [169], which is designed to extract localization information from a model trained solely on classification tasks by identifying and

visualizing the image subregions that are most discriminative for a particular class prediction. Its mechanism involves computing a class-specific weighted sum of the spatially informative feature maps from the final convolutional layer of a trained classifier to produce a coarse localization map, which can then be upsampled, often via bilinear interpolation, into a heatmap highlighting the most influential areas to the outcome. The value of the CAM $\boldsymbol{M}_c$ at a spatial location (x, y) for a given class c is generated using the formula $M_c(x, y) = \sum_k w_k^c f_k(x, y)$, where $f_k(x, y)$ is the activation of the k-th feature map at that location (x, y), and w_k^c is the weight corresponding to class c for that feature map [169]. These class-specific weights are learned by the final FC-layer of a deep classifier, which produces the final class scores by applying a linear transformation and a nonlinear activation function (e.g., sigmoid or softmax) to a feature vector created by a preceding global pooling operation (e.g., global average pooling – GAP) that condenses each feature map into a single scalar value [169]. While standard CNN classifiers used FC-layers for this final step, the introduction of global pooling represented a significant conceptual advance [245], as it reduces overfitting, enhances generalization, and improves model interpretability by establishing a direct correspondence between feature maps and class categories, a quality especially valuable in medical imaging, where explainability is crucial [245,246]. Despite its ingenuity, the standard CAM approach is hindered by two major limitations for direct application in precise segmentation: its inherently coarse-grained localization due to the low mapping resolution of conventional CNNs, and the rigid architectural constraint imposed by the requisite GAP layer, which often necessitates substantial and potentially performance-degrading model modifications [169,247].

To address the limitations of the standard CAM, the SqueezeNet architecture was selected for the classification and initial localization stage (Figure 1B). As a compact and modular CNN, SqueezeNet is known for achieving AlexNet-level accuracy with an approximately 50-fold reduction in parameters [248]. This parameter efficiency is accomplished through its core building blocks, the "fire modules," which employ a "squeeze-and-expand" strategy using 1 × 1 and 3 × 3 filters to reduce the complexity and size of the model. Unlike larger networks that require significant modification (the removal of layers) to preserve spatial detail and increase their mapping resolution (e.g., AlexNet-GAP, VGGNet-GAP, GoogLeNet-GAP - increasing from 6 × 6 to 13 × 13 for a 227 × 227 input, or from 7 × 7 to 14 × 14 for a 224 × 224 input), the design of this classifier intrinsically delays downsampling, naturally producing a higher-resolution final feature maps (13 × 13 for a 224 × 224 input), and it also includes a global pooling layer by default [248]. For our pipeline, the 800 × 800 input patches were resized to 572 × 572 and normalized to the interval [0, 1], achieving a mapping resolution of 34 × 34 and aligning with the subsequent U-Net refinement. We adopted the "simple bypass" variant of the

architecture, which incorporates skip connections around "fire modules" (3–9) to enhance performance without increasing model size, adding a final sigmoid activation for our binary classification task. To further improve localization quality based on the work of [247], the standard GAP layer was replaced with a TAP layer, averaging activations above a threshold to balance the broad coverage of GAP with the focused precision of global max pooling (GMP), and negative weight clamping was employed during CAM generation, a technique which provides a cleaner localization by suppressing BG noise while preserving the entire object extent, including its less discriminative parts.

In addition to the architectural design, the training strategy for the SqueezeNet classifier incorporated an extensive on-the-fly data augmentation protocol to improve generalization. Beyond standard geometric transformations (rotation, shearing, zooming, horizontal and vertical flipping), this protocol was complemented by mixup regularization. A key finding of our preliminary experiments was the necessity of a class-context-dependent parameterization for the symmetric Beta-distribution used to sample the mixup coefficient, λ. For intra-class mixing, a Beta($\alpha = 0.8, \beta = 0.8$) distribution was used to generate strongly interpolated examples. For inter-class mixing, however, the standard approach [162] proved counterproductive due to the presence of weakly staining amyloid deposits. Mixing positive signals with negative samples produced attenuated images that visually resembled naturally weak positives yet were assigned disproportionately low soft labels, an effect akin to manifold intrusion. To avoid creating supervisory ambiguity, a Beta distribution with low concentration parameters ($\alpha = \beta = 0.2$) was employed to keep the mixing minimal, thereby preventing the model from learning to penalize the defining features of these diffuse plaques.

Following model fitting, CAMs were extracted from the classifier and prepared for the subsequent refinement process involving U-Net training. Initially, the 34 × 34-pixel maps were upsampled to 572 × 572 to align with a standard U-Net architecture and then normalized on a per-sample basis to a range of [0, 1], a process simplified to scaling by the maximum activation value as the preceding negative weight clamping had already guaranteed a minimum of zero [169,247]. To create dedicated object and BG databanks for dynamic image synthesis, pixel-level pseudo-masks and their corresponding image patches were generated based on the scaled heatmaps using a simple two-level thresholding. First, a high-confidence FG mask prior was generated for each CAM by applying a strict threshold of > 0.5. The contours of the resulting binary regions, detected via cv2.findContours [242], were then used to extract the corresponding object priors, along with their local context, from the micrograph patches, populating a dedicated object-level image bank. In a parallel process designed to synthesize BG-only scenes, a more lenient threshold of > 0.2 was applied to the CAMs. These initial regions were then dilated using a 25-pixel circular structuring element to create expanded buffer zones, and the resulting expanded mask was then removed from the image. These irregular holes were

inpainted using the Shift-Map algorithm (OpenCV 4.2.0) [242], a method that reconstructs missing regions by optimizing a Markov random field energy function based on dominant patch offsets [249], notably without requiring additional DL models. These completed, object-free images were then aggregated into a unified BG bank, supplementing the original set of negative samples.

For the pixel-wise refinement stage of our WSSS framework (Figure 1C), we selected the canonical U-Net [143] as the backbone, widely regarded as a well-documented benchmark for biomedical segmentation tasks [250–252], and we implemented its standard 'vanilla' architecture with a patch-based training manner from scratch. Its proven effectiveness in data-scarce scenarios and robust symmetric encoder–decoder design provides a solid foundation, allowing the focus to remain on our advanced data-centric approach and the challenges of weak label handling, rather than on complex architectural modifications.

The contracting path of the network consists of repeating blocks of 3 × 3 convolutions with valid padding and 2 × 2 max pooling operations, which extract high-level semantic representations and progressively reduce the spatial resolution while increasing the number of feature channels. This downsampling process culminates in a bottleneck layer at the lowest resolution. Conversely, the expansive path systematically restores spatial resolution through blocks that first perform a 2 × 2 up-convolution and then combine the resulting feature maps with those from the corresponding contracting path level, which are first cropped for spatial alignment before being transferred using shortcut connections. Finally, a 1 × 1 convolutional layer is used to generate the pixel-level class probabilities from which the final segmentation is produced [143,250].

To ensure the generalization capabilities of the segmenter network, we developed an extensive object-level augmentation pipeline, recognizing that robust augmentation is paramount for achieving optimal performance in segmentation tasks [143,250]. The pixel-level supervisory signal for the U-Net training was provided by synthetically generated pseudo-mask and image pairs, assembled on-the-fly from previously curated object and BG databanks.

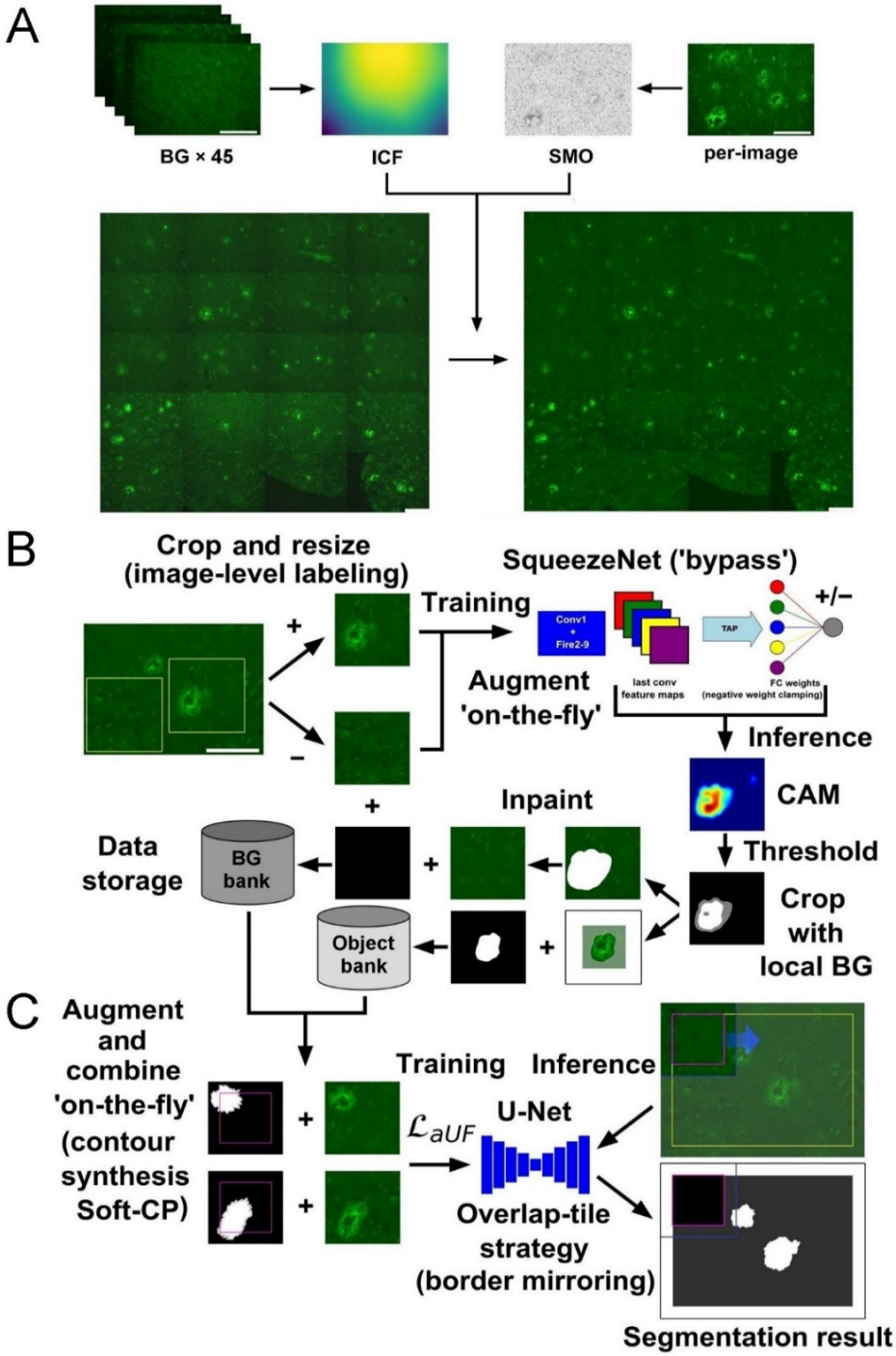

Figure 1. Schematic of the three-stage pipeline for weakly supervised amyloid plaque segmentation. (**A**) The first stage involves robust image preprocessing of micrographs stained with ThioS, where an ICF mitigates uneven illumination and the SMO estimates and corrects for BG noise. (**B**) In the second stage, a SqueezeNet classifier incorporating a TAP layer is trained on weakly labeled image patches (presence/absence of amyloid) to generate CAMs. These maps undergo post-processing (e.g., negative weight clamping, thresholding) to create databanks of FG object priors and inpainted, object-free BG images. (**C**) The third stage utilizes these databanks for on-the-fly synthesis of training exemplars, combining objects and BGs with advanced augmentation techniques like Soft-CP and contour synthesis. A U-Net segmentation model is then trained on these synthetic pseudo-labels, optimized with an asymmetric unified focal loss ($\mathcal{L}_{aUF}$), and final full-image masks are produced using an overlap-tile inference strategy and border mirroring. Our framework enables to semantically distinguish parenchymal amyloid pathology from confounding elements using only weak supervision, thereby surpassing the limitations of methods that rely solely on ThioS-staining intensity. All scale bars shown consistently represent a length of 100 micrometers, and their size is adjusted to match the corresponding image panels.

These databanks, as described in the preceding sections, were created utilizing the CAMs of the positively labeled images from the SqueezeNet classifier and subsequently stored for the training phase. Our modular approach decouples image components and maximizes the environmental and contextual diversity available for object insertion, providing a foundation for large-scale dynamic synthetic data creation via object-level augmentation [253–260]. Specifically, during the U-Net training phase, a random number of object instances (between 0 and 5) were inserted into these BG scenes to address data scarcity and class imbalance, while their corresponding pseudo-masks were handled similarly, allowing for a combinatorial synthesis of data that augments the critical boundaries between objects and their environment.

To further enhance diversity, particularly at object boundaries, a contour perturbation step was integrated into the pipeline prior to the cut-and-paste operation. A synthetic contour was generated for each pseudo-object mask and subsequently used both to update the mask itself and to crop the corresponding grayscale image region from its local surroundings. While contour randomization has been explored in radiomics to assess feature robustness against delineation uncertainty [261,262], and synthetic contour generation has been used in texture segmentation (e.g., hematoxylin/eosin lymphoma mosaics) [263], our approach is novel in repurposing these concepts specifically for object-level data augmentation in a weakly supervised setting. The applied perturbation adapts the restorable contour synthesis algorithm proposed in [264] by modifying its core mechanism to enhance both structural integrity and variability, though it was primarily developed to generate restorable GT approximations for evaluation tools also has a suggested potential for augmentation. To achieve this, instead of injecting Gaussian noise in arbitrary directions as in the original method [264], we constrained keypoint-displacement to be perpendicular to an approximation of the local contour tangent, a strategy that ensures perturbations occur along the normal vector, effectively preventing self-intersections and maintaining a coherent, plausible shape outline even when introducing a greater degree of variability (standard deviation parameter). The keypoints for the polygonal approximation were sampled at intervals of 5–10 pixels along the original contour, and the magnitude of the applied noise was directly proportional to this sampling gap size.

Finally, to ensure the natural-looking integration of the objects, the Soft-CP blending strategy was applied [258]. This technique smooths object mask edges through a sequence of erosion and dilation operations (5 iterations each) and weights the mask values based on their distance from the contour boundary, while using this soft mask to blend the input images for seamless visual transition. In our application, while the blending was applied to the input image, the transitional regions of the soft masks were ignored during loss computation, analogously to the trimap technique. These unlabeled zones encourage the U-Net to infer the surrounding, uncertain areas by using the hard, high-

confidence pseudo-mask regions as "seeds" and propagating the labels from the core regions.

Once the U-Net was trained on these synthetically generated exemplars, a standardized inference and post-processing pipeline was employed to generate the final segmentation for the entire micrographs. First, to prevent edge artifacts, an overlapping tiling strategy with border mirroring was employed, dividing each micrograph into tiles that were resized for prediction before their resulting masks were reassembled into a single segmentation map. This raw map subsequently underwent a binary thresholding (at 0.5), hole-filling, and the removal of both sub-3500-pixel and image-boundary-adjacent particles.

3.3.2 Implementation details: Training and evaluation strategy[I.]

The SqueezeNet-TAP classification model was trained from scratch using the cropped histopathological patches and their corresponding image-level binary GT-labels (presence/absence of parenchymal amyloid) with on-the-fly augmentation. The training was performed using the root mean square propagation (RMSprop) optimizer with a fixed learning rate of 5×10^{-6} and a batch size of 64, over 800 epochs. The objective was to minimize the binary cross-entropy loss ($\mathscr{L}_{\mathrm{BC}}$), a standard loss function for binary classification tasks that measures the divergence between the true labels (y) and the predicted probabilities (p):

$$\mathscr{L}_{\mathrm{BC}} = -\frac{1}{N}\sum_{i=1}^{N}[y_i \log(p_i) + (1 - y_i)\log(1 - p_i)]$$

The U-Net segmentation model was subsequently trained using exclusively the on-the-fly generated synthetic dataset sourced from the databanks of the objects and scenes produced based on SqueezeNet-CAMs. For this task, the optimization was performed using the adaptive moment estimation (Adam) optimizer, configured with a learning rate of 0.001 and standard $\beta 1 = 0.9$, $\beta 2 = 0.999$, $\varepsilon = 1 \times 10^{-7}$ parameters. The model was trained for 30 epochs with a batch size of 16. To further address the significant pixel-wise class imbalance inherent in our dataset, a generalized loss function, the asymmetric unified focal loss ($\mathscr{L}_{\mathrm{aUF}}$) was chosen [265] that provides a unified framework integrating the benefits of modern region-, distribution-based, and compound losses requiring only three hyperparameters to control its behavior, which were set to their proposed values of $\lambda = 0.5$ (component weighting), $\delta = 0.6$ (balancing), and $\gamma = 0.5$ (focusing parameter). Its asymmetric formulation introduces a beneficial bias towards the FG class at the expense of the BG. In our implementation, the standard $\mathscr{L}_{\mathrm{aUF}}$ was adapted for the training data to account for the presence of ignored pixels (i.e., the trimap regions), ensuring that these areas did not contribute to the final loss. The formal definition of the $\mathscr{L}_{\mathrm{aUF}}$ involves its two components, the modified asymmetric focal loss ($\mathscr{L}_{\mathrm{maF}}$) and the modified asymmetric focal Tversky loss ($\mathscr{L}_{\mathrm{maFT}}$):

$$\mathscr{L}_{\mathrm{aUF}} = \lambda \mathscr{L}_{\mathrm{maF}} + (1 - \lambda)\mathscr{L}_{\mathrm{maFT}}$$

$$\mathscr{L}_{\mathrm{maF}} = -\frac{\delta}{N} y_{i:r} \log(p_{t,r}) - \frac{1-\delta}{N} \sum_{c \neq r} (1 - p_{t,c})^{\gamma} \log(p_{t,r})$$

$$\mathscr{L}_{\mathrm{maFT}} = \sum_{c \neq r} (1 - \mathrm{mTI}) + \sum_{c = r} (1 - \mathrm{mTI})^{1-\gamma}$$

Here, N denotes the total number of pixels, while y and p are the labels and predicted values. The term p_t represents the probability of predicting the true values. Furthermore, i, c, and r are the respective indices for the pixel, class, and rare class. Finally, mTI is the modified Tversky index, which is given by:

$$\mathrm{mTI} = \frac{\sum_{i=1}^{N} p_{0i} g_{0i}}{\sum_{i=1}^{N} p_{0i} g_{0i} + \delta \sum_{i=1}^{N} p_{0i} g_{1i} + (1-\delta) \sum_{i=1}^{N} p_{1i} g_{0i}}$$

In this index, p_{0i} and p_{1i} represent the predicted probabilities for BG and FG, while g_{0i} and g_{1i} are the respective indicators of the GT (taking a value of 1 for true, 0 otherwise) [265].

To rigorously assess the performance, a unified experimental setup was established for both the classification and segmentation models (SqueezeNet, U-Net), based on a patient-wise 7-fold cross-validation scheme with each fold representing a distinct subject (i.e., a leave-one-subject-out approach), ensuring methodological consistency and data integrity. This patient-level splitting was deliberately chosen to prevent any form of data leakage between subjects, thereby providing a realistic estimate of how well the models generalize to new, unseen individuals, which is a critical requirement in clinical applications. A key aspect of our evaluation strategy was the strict preservation of these cross-validation folds across both modeling tasks, made essential by the sequential nature of our pipeline, where the classification model is tasked with generating localization priors (CAMs) for the subsequent training of the segmentation model. By maintaining the same data splits, we ensured that for any given subject (fold) as a test set, the priors used to train the segmenter were generated exclusively by a classifier that had never been exposed to that subject's samples. In this setup, the dataset was partitioned into seven folds, where each fold contained all the image patches from a single, unique subject (including all image samples from the patient's two brain regions). The models were then trained iteratively seven times (resulting in seven distinct trained models for each task); in each iteration, six folds (subjects) were used for training, while the remaining one was held out for testing. The final performance metrics were calculated by averaging the results obtained across these seven independent test folds.

Within each cross-validation loop, a robust procedure was followed for model training and selection. For the SqueezeNet classifier, a development (or validation) set was created by randomly sampling 10% of the data from the six active training folds to guard against overfitting. After training for 800 epochs, with checkpoints saved periodically, the model state that achieved the lowest validation loss on this development set was selected for the final evaluation on the held-out test subject (and

CAM generation for the U-Net training). In contrast, for the U-Net segmenter, a different strategy was employed. While a similar 10% development set was used for training dynamics monitoring, it served exclusively for observing stability; due to the computational demands of the augmentation pipeline, training was limited to a fixed duration of 30 epochs. Consequently, model selection was not based on its performance; instead, the model checkpoint from a fixed, predetermined epoch (the 30^{th}) was consistently used for the final evaluation. This development set also underwent the full image augmentation process, ensuring it reflected the synthetic boundary variations present in the training images.

The evaluation of the pipeline focused on its end-to-end segmentation performance, validating the final assembled and postprocessed predictions against our manually annotated full-field GT-masks under the rigorous protocol described. Beyond the direct evaluation of the classification performance of the SqueezeNet, the effectiveness of its localization priors was measured implicitly by their downstream impact on the final segmentation performance. This decision was informed by the significant computational cost of the rigorous evaluation and by several challenging characteristics of the patch-based dataset that would complicate any fair comparison. The performance of both the classifier and segmenter was quantified using standard metrics derived from a confusion matrix; distinction lies in the evaluation level: image-level for the SqueezeNet classifier and pixel-level for the U-Net segmenter. To present these metrics in a unified and non-redundant manner, the following table (Table 1) uses a combined notation where the *c/s* indicates that the formula applies to both classification (*c*) and segmentation (*s*) contexts, using the appropriate confusion matrix elements.

The entire training and evaluation pipeline was implemented in Python using the TensorFlow framework, supported by standard libraries for data handling and augmentation [240–242,266]. All high-intensity computations were performed on an NVIDIA GeForce RTX 4090 GPU with 24 GB of dedicated memory.

Table 1. Overview of Performance Evaluation Metrics. The table defines the standard metrics used to assess the performance of both the classification and segmentation models, with all formulas derived from the confusion matrix elements: true positives (*TP*), true negatives (*TN*), false positives (*FP*), and false negatives (*FN*). The subscript *c/s* is used to denote applicability to both the image-level classification (*c*) and pixel-level segmentation (*s*) contexts, respectively.

Accuracy / Pixel-level Accuracy (PA): $\frac{TP_{c/s}+TN_{c/s}}{TP_{c/s}+TN_{c/s}+FP_{c/s}+FN_{c/s}}$	*This metric represents the overall fraction of correctly identified items (either image patches for classification or pixels for segmentation). While providing a general measure of reliability, it can be misleadingly high in scenarios with significant class imbalance, a common issue in pixel-level segmentation.*
Precision: $\frac{TP_{c/s}}{TP_{c/s}+FP_{c/s}}$	*This metric quantifies the proportion of true positive predictions among all instances identified as positive. For classification, it indicates the reliability of patches flagged as containing pathology. For segmentation, it reflects the fraction of pixels correctly identified as deposit within the prediction.*

Recall (Sensitivity): $\frac{TP_{c/s}}{TP_{c/s}+FN_{c/s}}$	*This metric measures the model's ability to identify all true positive instances. In the classification context, it shows the proportion of actual deposit-containing patches that were successfully detected. In segmentation, it measures the fraction of true deposit pixels that the model successfully captured.*
F1-Score / Dice Score Coefficient (DSC): $\frac{2*TP_{c/s}}{2*TP_{c/s}+FP_{c/s}+FN_{c/s}}$	*This metric is defined as the harmonic mean of precision and recall and provides a balanced assessment of performance. It is commonly referred to as the F1-score in classification tasks, where it is particularly informative for imbalanced datasets, and as the DSC in segmentation, where it serves as a standard measure of agreement widely used in biomedical imaging to quantify the spatial overlap between prediction and GT.*
Jaccard Index (IoU): $\frac{TP_s}{TP_s+FP_s+FN_s}$	*This metric, also known as intersection over union, provides a stricter assessment of spatial overlap than DSC. It calculates the ratio of the intersection to the union of the predicted and GT positive regions.*
Specificity: $\frac{TN_s}{TN_s+FP_s}$	*This metric measures the model's ability to correctly identify true negative (BG) pixels. High specificity is crucial for avoiding over-segmentation, ensuring non-deposit regions are correctly ignored.*
Negative Predictive Value (NPV): $\frac{TN_s}{TN_s+FN_s}$	*This metric indicates the proportion of correctly identified negative pixels among all instances predicted as negative, measuring the reliability of a negative prediction.*
False Positive Rate (FPR): $\frac{FP_s}{FP_s+TN_s}$	*This metric quantifies the proportion of negative pixels that were incorrectly classified as positive.*
False Discovery Rate (FDR): $\frac{FP_s}{FP_s+TP_s}$	*This metric indicates the proportion of incorrect positive predictions among all instances predicted as positive.*
False Negative Rate (FNR): $\frac{FN_s}{FN_s+TP_s}$	*This metric represents the fraction of actual positive pixels that the model failed to detect.*
False Omission Rate (FOR): $\frac{FN_s}{FN_s+TN_s}$	*This metric measures the proportion of false negatives among all instances predicted as negative, quantifying the risk of a negative prediction being incorrect.*

3.4 Morphometric profiling of amyloid deposits: Particle analysis[I.]

A detailed morphometric analysis was conducted on parenchymal amyloid deposits, comparing samples across both cortical regions (parietal and temporal) and dementia statuses (dementia and non-dementia). The methodology involved delineating plaque subregions based on the corrected staining intensity, extracting a comprehensive set of object-level morphometric parameters, and performing a comparative statistical analysis. To quantitatively differentiate plaque components based on a non-specific stain alone, we followed a method from prior work [55]. We delineated compact and diffuse subregions for each plaque using fixed intensity thresholds derived from the 80th and 50th percentiles of the global intensity distribution, which was calculated from all pixels within the previously segmented deposit masks across the entire dataset. These binary masks, along with the original grayscale data, formed the basis for all feature extraction.

In total, 19 morphometric parameters were extracted using ImageJ and its FracLac plugin (https://imagej.net/ij/plugins/fraclac/FLHelp/Introduction.htm) [244,267,268]. While 7 of these extracted measures have been previously applied to the analysis of amyloid plaques [24,30–32,44,55,269], this study introduces 12 additional descriptors from general biological (cellular or tissue-level) analysis workflows to offer novel insights into the structural organization of the amyloid deposits. These parameters were grouped into four functional categories:

- **Size-related metrics:** All size-related metrics were log-transformed (base 10) to manage the characteristic log-normal size distribution of amyloid plaques. This category included core metrics including **deposit area**, **compact area** (in μm^2), calculated from pixel counts, and the **perimeter** (in µm), representing the boundary length, as well as **convex hull metrics** (features were derived from the convex hull, the minimal convex polygon enclosing the deposit) capturing overall plaque dimensions. These latter included **hull area** (μm^2), **hull perimeter** (µm), **bounding circle diameter** (µm), **maximum span** (µm), and **mean radius** (µm).
- **Structural complexity descriptors:** Size-invariant features were measured to quantify intricate spatial patterns and irregularity of plaques. These included **fractal dimension** (quantifying complexity via a box-counting algorithm) and **lacunarity** (measuring spatial heterogeneity or "gappiness") were computed using the FracLac plugin with a binary scanning method, averaged over 12 randomized grid positions for robustness to assess complexity and heterogeneity), as well as further core- and hull-derived metrics like **roughness** (perimeter-to-hull-perimeter ratio, capturing boundary jaggedness), **circularity** (area-perimeter relationship, similarity to a perfect circle), and **solidity** (deposit-to-hull-area ratio, indicating compactness).
- **Geometric and symmetry features:** These convex hull-based parameters characterized the overall shape and elongation of deposits, including the **span ratio** (major-to-minor axis ratio), **max/min radii ratio**, and **hull circularity**.
- **Intensity-based characteristics:** These parameters captured information related to staining intensity and distribution, including the **mean gray value**, **integrated density** (product of the area and the mean gray value, also log-transformed), and the **diffuseness index** (the proportion of the non-compact area relative to the total deposit area.

The extracted morphometric data were then subjected to a comparative statistical analysis across four experimental groups defined by cortical region and dementia status: (1) parietal/non-dementia, (2) parietal/dementia, (3) temporal/non-dementia, and (4) temporal/dementia. Prior to analysis, all parameters were standardized via z-score transformation (SciKit-Learn StandardScaler) [270], and a small constant was added to features with zero values (e.g., compact area) to permit the required log-transformation [271,272]. The statistical workflow involved employing PCA to reduce the

dimensionality of the feature space and identify the dominant modes of morphometric variation. The principal components (PCs) explaining most of the data variance were then selected for group-wise comparisons using an analysis of variance (ANOVA) to detect significant differences in the average PC scores across the four experimental groups, followed by a Tukey post-hoc test for pairwise comparisons. All statistical procedures were performed using Python (with libraries such as scikit-learn, matplotlib, pandas, and scipy) and R (stats package) to ensure reproducibility [240,270,273–276]. The ImageJ software and its FracLac plugin can be accessed via their respective official documentation websites [244,267,268].

3.5 Supplementary methodological contributions to collaborative studies[II., III.]

3.5.1 Ethical declarations[II., III.]

All animal experiments were carried out in strict compliance with the European Council Directive (86/609/EEC) and EC regulations (O.J. of EC No. L 358/1, 18/12/1986) regarding the care and use of laboratory animals for experimental procedures and followed relevant Hungarian and local legislation requirements. Our experimental protocols were approved by the Institutional Animal Welfare Committee of the University of Szeged (II./1131/2018). Pregnant Sprague–Dawley rats were maintained under standard housing conditions and fed ad libitum.

3.5.2 Quantitative morphological analysis of microglia[II.]

In addition to the primary research presented in this thesis, I contributed as a co-author to a collaborative study investigating the cytomorphological effects of the anti-inflammatory compound SZR104. My primary objective and contribution to this project was to design and execute a computational image analysis workflow for immunofluorescence micrographs to objectively quantify and statistically compare a set of morphological parameters.

The analysis was performed on two-channel digital micrographs (.tif format) provided by the collaborating laboratory. These images captured secondary microglial cultures derived from newborn rat forebrains, where cell nuclei were labeled with 2-[4-(aminoiminomethyl)phenyl]-1H-indole-6-carboximidamide hydrochloride (DAPI; blue channel), and the cytoplasm of microglia was identified with an anti-CD11b/c primary antibody visualized by an Alexa Fluor 568-conjugated secondary antibody (red channel). My workflow, designed to extract robust quantitative data from these images, was implemented primarily in ImageJ (v1.47) and its FracLac plugin [244,267,268], with all subsequent statistical analysis conducted in Python [240].

The process involved splitting the multi-channel images, converting each channel to 8-bit grayscale, and binarizing them using a consistent threshold. A key challenge, a frequently observed weaker cytoplasmic staining intensity in the perinuclear region, was overcome with a two-channel segmentation

strategy. First, the separate binary silhouettes for nuclei and cytoplasm were subjected to a series of automated cleaning operations (hole filling, watershed separation, size- and edge-exclusion) and manual editing where required for heavily clustered cells. Then, the cleaned nuclear and cytoplasmic masks were merged to generate a final, solid cell silhouette for quantification, effectively filling any potential gap in the cytoplasmic signal.

From these final silhouettes, a comprehensive set of morphometric parameters was quantified using the ImageJ and FracLac plugin [244,267,268]. The definitions for most of the quantified parameters (including area, perimeter, convex hull metrics, and fractal analysis) are described in detail in Chapter 3.4 of this dissertation and are therefore not reiterated here. This analysis specifically included the transformation index, the reciprocal of circularity, as a conventional descriptor of microglia morphology [218]. Conversely, metrics primarily used for the characterization of amyloid plaques in the main body of this thesis, such as compact area and diffuseness index, were not applied in this cellular context, nor were the intensity-based measurements also performed in that study. It is noted, however, that for fractal dimension measurements, the solid binary silhouettes were first converted to single-pixel outlines as required by the box-counting algorithm to quantify the complexity of the cellular boundary [219] (Publication II./Supplementary Figures S2–S4).

Finally, I conducted the statistical analysis on the full dataset (Publication II./Supplementary Table S1), comprising 974 individual microglial cells across six experimental groups. This was performed in a Google Colaboratory notebook using Python (v3.7.13), leveraging the SciPy, Pandas (v1.4,.4), and NumPy (v1.23.0) libraries [240,241,243,273,274]. To test for differences between the groups, a non-parametric Kruskal–Wallis H-test was applied, followed by post-hoc Mann–Whitney U tests with Bonferroni correction for multiple comparisons.

3.5.3 Quantitative analysis of autophagosomes in microglia[III].

In a second collaborative study, to which I contributed as a co-author, the project aimed to investigate the regulation of autophagy in microglia under different inflammatory conditions. My specific role in this project was to develop and apply an image analysis workflow to accurately identify and count p62/SQSTM1-positive puncta per cell from the provided immunofluorescent images.

The analysis was performed on three-channel immunofluorescent digital micrographs (.tif format) provided by the collaborating laboratory. These images captured secondary microglia-enriched cultures where microglia were identified with an anti-Iba1 antibody visualized by an Alexa Fluor 568-conjugated secondary antibody (red channel), autophagosomes were labeled with an anti-p62/SQSTM1 antibody visualized by an Alexa Fluor 488-conjugated secondary antibody (green channel), and nuclei were stained with DAPI (blue channel). My contribution was to develop and

execute a specific workflow in ImageJ [244] to quantify the number of p62/SQSTM1 puncta within the cytoplasm of individual Iba1-positive microglial cells across the different experimental conditions.

The initial and most critical step after scaling was the accurate segmentation of individual microglial cells to create ROIs for the analysis. To achieve this, a multi-step, fully automated process was developed and performed under identical settings for each image to extract the contours of Iba1-positive cells and their corresponding nuclei. The process involved splitting the image channels, converting them to 8-bit grayscale, and then applying noise reduction, BG correction, and consistent thresholding, followed by binary morphological operations and filtering to create clean masks. A key step for separating touching cells was using the Find Maxima on the unthresholded DAPI channel to generate segmenting lines, which were then applied to the binarized Iba1 and DAPI masks, ensuring that puncta counts could be reliably assigned to unique, intact cells.

Once the cytoplasmic ROI for each of the 1350 identified microglial cells was defined, the analysis focused on the green (p62/SQSTM1) channel. To enhance the puncta signal against diffuse cytosolic staining (soluble component of the p62/SQSTM1 pool) and BG noise, a rolling ball BG subtraction algorithm was applied, with the radius parameter set based on the upper bound of the known autophagosome size range (0.75 μm = 4.215 pixels). Subsequently, the images were binarized, and watershed and fill holes operations were used to separate individual puncta. A critical quality control step was the automated filtering of detected objects based on size. Following the literature and the established scale for the images (1 μm = 5.62 pixels), the known diameter of autophagosomes (0.5–1.5 μm) was converted into a pixel area range (6 to 56 pixels²), calculated using the formula $A = r^2\pi = \frac{d^2\pi}{4}$ (where A = area, r = radius, d = diameter) and assuming near-spherical objects. Only objects falling within this specific range were counted as valid puncta using ImageJ's Analyze Particles function.

This final count was performed individually for each cell, ensuring that only signals located within the previously defined cytoplasmic ROIs were included (Publication III./Supplementary Table S2). The statistical significance of the differences between experimental groups was determined using the Kruskal-Wallis H-test followed by Dunn's multiple comparison test with Bonferroni adjustment for post-hoc analysis.

4. Results

4.1 Classification performance of the SqueezeNet model[I.]

The initial step of our WSSS pipeline involved training a SqueezeNet-based binary classifier that detects the presence of the ThioS-positive parenchymal amyloid in the micrograph crops. Its primary purpose within the pipeline was not to perform direct segmentation, but rather to generate robust localization cues (CAMs) from image-level labels of ThioS-stained histological image patches.

Accordingly, this section evaluates its performance strictly as a binary classifier, a critical prerequisite for generating reliable localization priors. The core architecture was completed with a simple bypass structure, and a TAP layer was added instead of a conventional GAP layer to enhance localization.

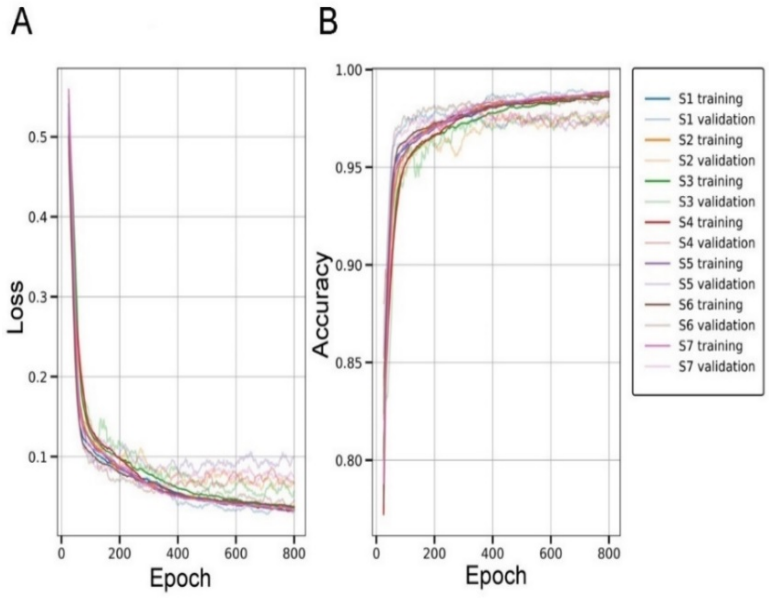

Figure 2. Performance monitoring of the SqueezeNet classifier across the seven training iterations of a patient-wise cross-validation. For each iteration, one subject's data served as the held-out test fold and was excluded from the training process shown here. The plots display the (**A**) binary cross-entropy loss and (**B**) accuracy curves for the training data (compiled from six subjects, darker shades) and the corresponding development (or validation) data (a 10% split of the data from these six subjects, lighter shades). Each color represents a unique training iteration. To enhance the clarity of performance trends, moving average is applied to all curves with a window size of 25 epochs.

Performance was assessed using a rigorous patient-wise 7-fold cross-validation to simulate generalization to new individuals and prevent data leakage. Within each fold, the model achieving the lowest loss on a 10% development set (validation data) over a maximum of 800 epochs (best performing checkpoint) was selected for testing (Figure 2). The classifier demonstrated excellent reliability in identifying patches containing parenchymal amyloid pathology, achieving a mean accuracy of 0.9794, precision of 0.9853, recall of 0.9699, and an F1-score of 0.9774 across all test folds (Publication I./Supplementary Table S1). These high classification scores, supported by visual inspection (Figure 3), confirmed the capability of the model to generate accurate localization priors for the subsequent segmentation stage.

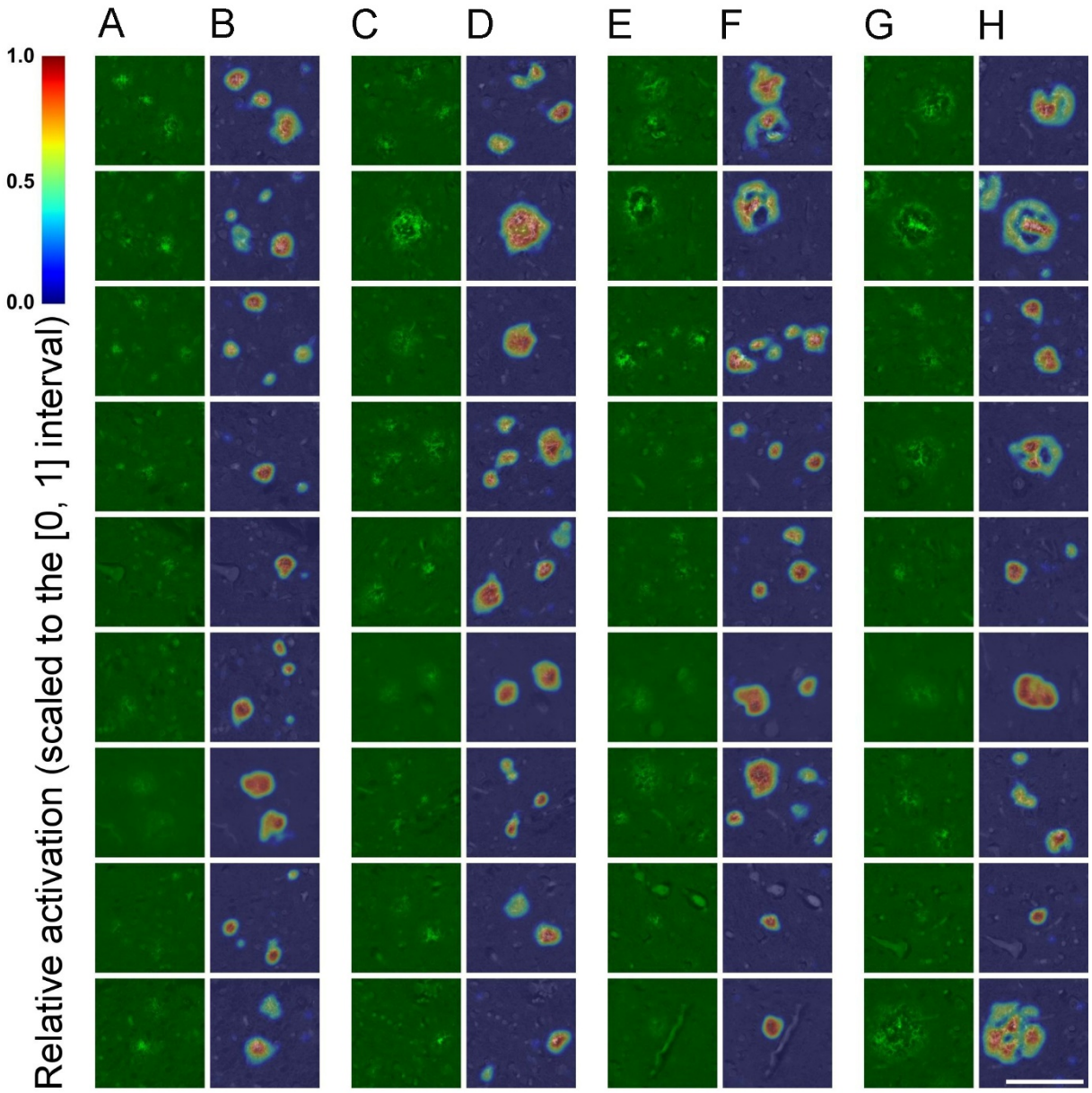

Figure 3. Visualization of localization priors (CAMs) from the final SqueezeNet-TAP model trained on the complete dataset. The composite image shows representative exemplars of positive patches arranged into four pairs of columns, where each pair consists of original input patches on the left (**A**, **C**, **E**, **G**) and their corresponding heatmaps overlaid on the source images on the right (**B**, **D**, **F**, **H**). Production of the heatmaps involved negative weight-clamping, upsampling to 572 × 572 pixels, and normalization to a range [0, 1], with the 'jet' colormap representing activation intensity (**blue** = low, **red** = high). The maps visualize the image regions the model identified as containing discriminative features of parenchymal amyloid deposits, which were subsequently utilized to guide the training of the segmentation model. The scale bar represents 100 micrometers.

4.2 Segmentation performance of the U-Net model[I]

For the pixel-level segmentation of ThioS-positive amyloid deposits in full-field micrographs, a U-Net model was trained in a weakly supervised manner. Its training relied exclusively on pseudo-labels derived from the CAMs of the previously trained SqueezeNet classifier. Crucially, while training was weakly supervised, guided by coarse localization priors, the final performance was validated against manually annotated GT masks that were completely held out from the training process.

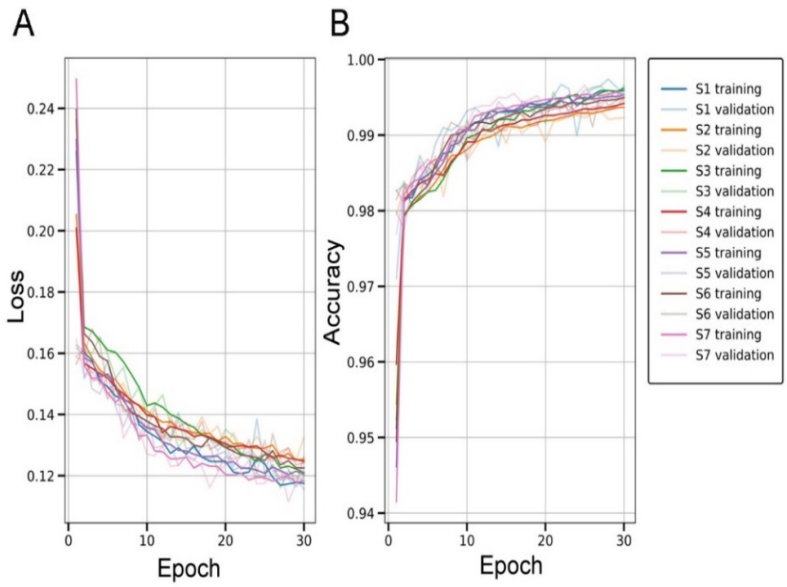

Figure 4. Performance monitoring of the U-Net segmenter during the seven training iterations of a patient-wise cross-validation. For each iteration, one subject's data served as the held-out test fold and was entirely excluded from the training process illustrated. The plots display the (**A**) asymmetric unified focal loss and (**B**) PA curves for the training data (compiled from the remaining six subjects, darker shades) and the corresponding development data (a 10% split of the data from these six subjects, lighter shades). Each color corresponds to a unique training iteration.

Adhering to the same 7-fold cross-validation structure, the CAMs from each classifier fold were post-processed into pseudo-masks. Based on these pseudo-masks, the image patches were then subjected to extensive on-the-fly object-level augmentation, where the identified FG objects were removed and randomly reinserted to diversify boundaries and spatial contexts. The U-Net was trained for a fixed duration of 30 epochs per fold, a decision informed by the computational demands of the augmentation pipeline. A 10% development set was used solely for monitoring training trends, not for model selection; the model from the 30th epoch was consistently used for evaluation (Figure 4).

The segmentation model achieved robust performance across the seven folds, yielding a mean Dice Similarity Coefficient (DSC) of 0.763, a Jaccard Index (intersection over union - IoU) of 0.639, a recall of 0.721, and a precision of 0.877. While pixel-level accuracy (PA) (0.990) and specificity (0.997) were high, their utility is limited by the severe class imbalance inherent in the pathology segmentation task. Key error rates included a false positive rate (FPR) of 0.003, a false discovery rate (FDR) of 0.123, and a false negative rate (FNR) of 0.279 (Publication I./Supplementary Table S2). These results demonstrate that our WSSS pipeline, leveraging CAM-derived pseudo-labels and object-level augmentation, can effectively approximate dense segmentation, establishing a feasible and high-throughput approach for producing robust pixel-level annotations for pathology micrographs with negligible expert labeling effort (Figures 5 and 6).

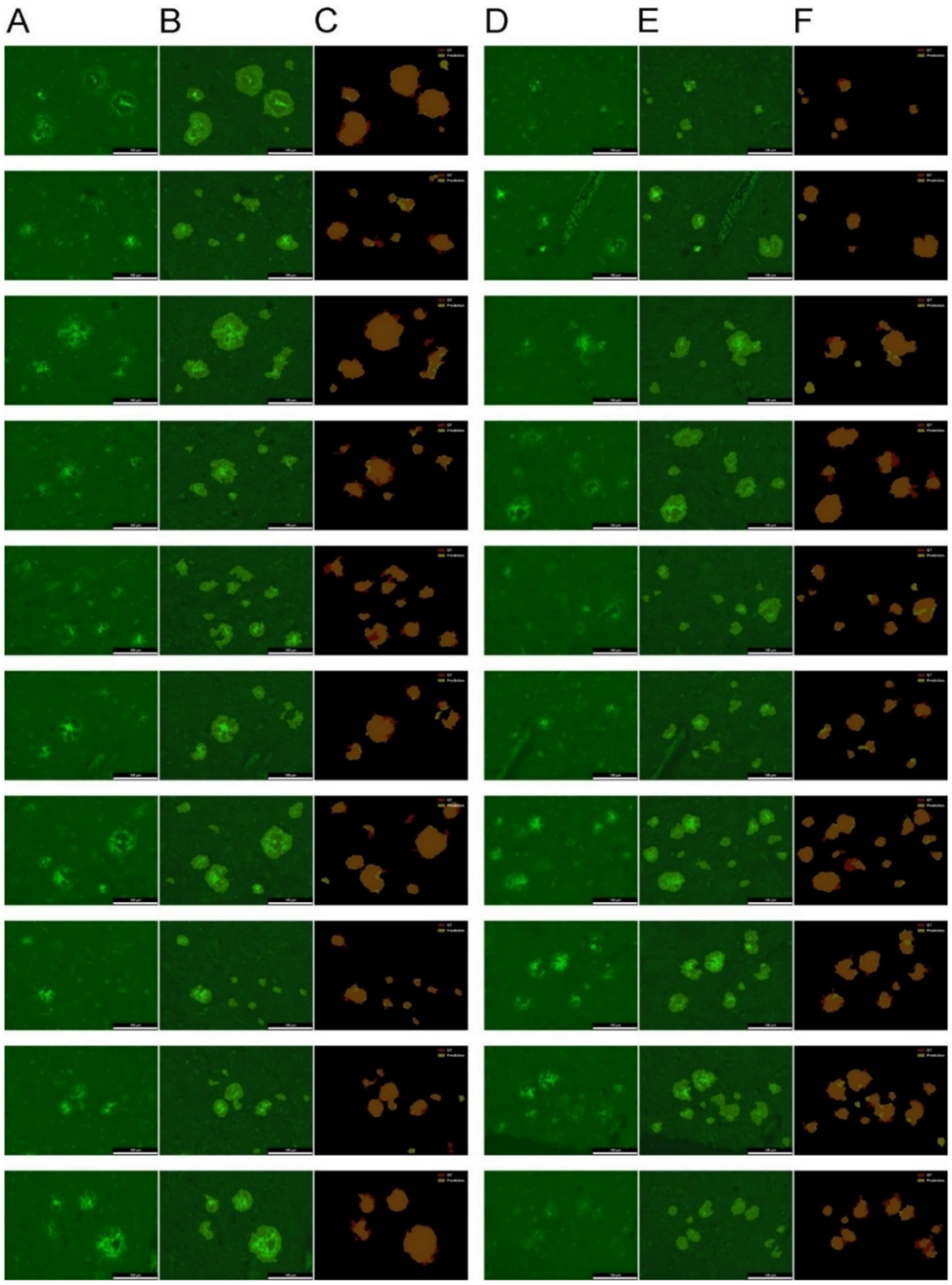

Figure 5. Qualitative assessment of the final U-Net segmentation results on fluorescent micrographs. The composite image shows representative exemplars in three sets of columns: original fluorescent micrograph images (**A**, **D**), the corresponding post-processed predictions (assembled from output patches) overlaid on the source images (**B**, **E**), and a comparison of the positive predictions (yellow) against the GT masks (red) (**C**, **F**). The orange color in the comparison panels indicates overlap (agreement, true positive pixels) between the prediction and the GT. The model demonstrates a strong ability to capture diverse plaque morphologies. Notably, it correctly identifies highly fluorescent vascular regions as BG elements, showcasing its capacity to distinguish parenchymal amyloid pathology from confounding structures based on learned semantic differences, a task not achievable based on solely fluorescence ThioS staining intensity thresholding. Minor discrepancies (materially fewer red and yellow areas, i.e., false negatives and false positives), discernible only upon detailed examination, are primarily located near challenging regions like vessels, small fragmented or uncertain structures, and clearance zones; and include deposits that were erroneously omitted from the original GT. The scale bar represents 100 micrometers.

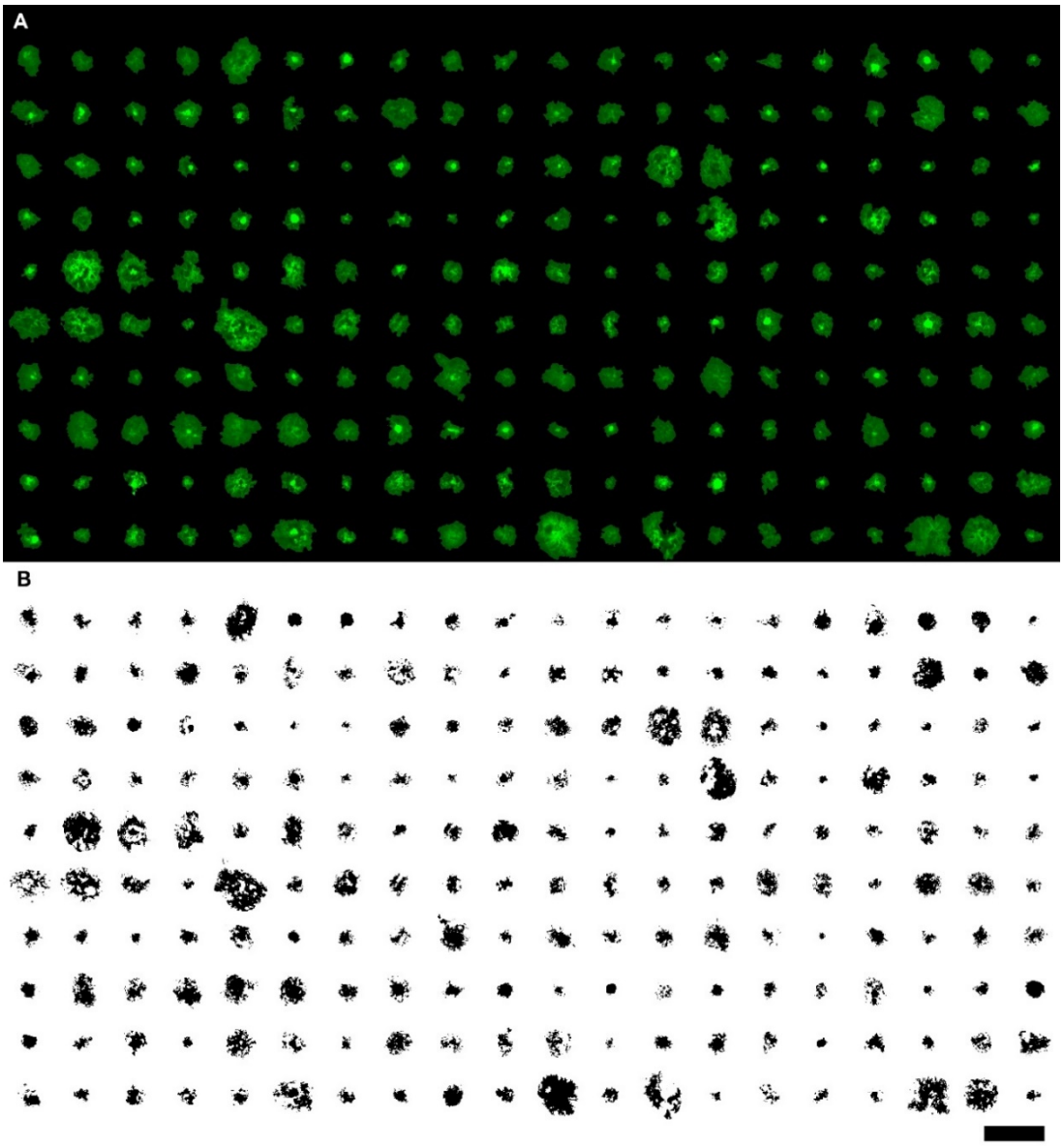

Figure 6. Visualization of segmented parenchymal amyloid deposits and their thresholded counterparts. (**A**) The composite image shows a gallery of representative amyloid deposits, automatically extracted by the final segmentation pipeline (with models trained on the complete dataset) from the intensity corrected full-field micrographs. To enhance visual detail, the gray scale objects are rendered in a uniformly contrast-adjusted green channel on a black background, showcasing the vast morphological diversity targeted by the framework. (**B**) The composite image shows the corresponding binary images for each deposit, generated by applying a global intensity percentile threshold to their grayscale counterparts. These binarized representations of the total deposit area, along with the compact area representations and the grayscale data, formed the basis for the subsequent morphometric profiling. A single scale bar, representing 100 micrometers, applies to all objects.

4.3 Morphometric analysis of the amyloid deposit characteristics[I.]

To investigate morphological differences in ThioS-stained deposits, a final segmentation model trained on the entire dataset was used to generate binary masks for detailed particle analysis (Figure 6). A set of 19 morphometric parameters was extracted from each deposit (Publication I./Supplementary Data) using ImageJ and its FracLac plugin, derived from a diverse array of measurement approaches, including basic binary particle analysis, convex hull metrics, grayscale intensity calculations, box-counting measurements (Figure 7), and various composite ratios.

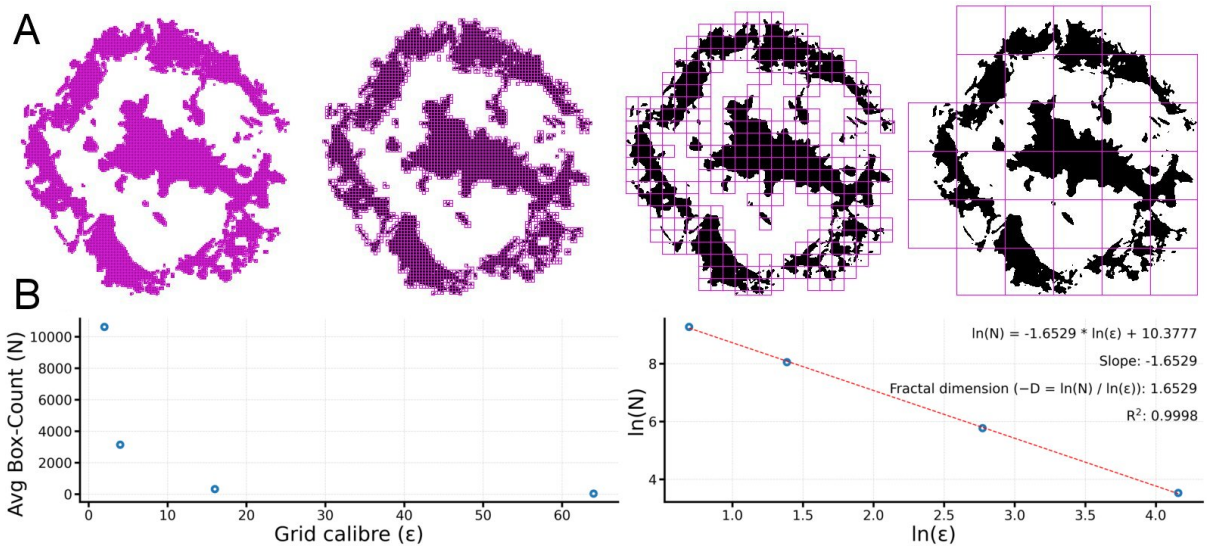

Figure 7. Illustration of the box-counting method for fractal dimension calculation. (**A**) Visualization of the binary box-counting algorithm applied to a representative thresholded deposit image. The panel demonstrates how the structure is covered by a series of grid calibers (box-sizes, ε) derived from the power series scaling, all shown for a single, representative grid position out of the 12 used in the calculations. (**B**) The resulting data are plotted. The **left** plot shows the average box counts (N) (across all 12 grid positions for each caliber) against the scale (ε) on linear axes. The **right** plot displays the same data points on a ln-ln scale, where the slope of the linear regression line fitted to the data (**red dashed line**) determines the final fractal dimension (D). The equation of the regression line, the coefficient of determination (R^2), and the formula for D are also shown.

PCA was applied to this feature set, successfully reducing its dimensionality by identifying three PCs that collectively accounted for over 85% of the total data variance (Figure 8A). An analysis of the component loadings (Publication I./Supplementary Table S3) revealed distinct morphological signatures:

- **PC1** was strongly associated with **overall size**, showing high loadings for deposit area (0.315), integrated density (0.314), and hull area (0.304).
- **PC2** captured **structural complexity and spatial heterogeneity**, with dominant loadings from solidity (0.395), circularity (0.372), fractal dimension (0.313), and negative contributions from lacunarity (−0.370).
- **PC3** represented **global geometry and elongation**, primarily driven by span ratio (0.520), max/min radii ratio (0.469), and hull circularity (−0.511).

Group-wise comparisons of the PC scores revealed significant differences across both brain regions and dementia statuses (ANOVA; PC1: $F = 7.29$, $p < 0.001$; PC2: $F = 33.72$, $p < 0.001$; PC3: $F = 35.82$, $p < 0.001$). Post-hoc Tukey tests provided further insights (Figure 8B; Publication I./Supplementary Tables S4 and S5):

- For **PC1**, scores were significantly higher in both dementia groups (parietal and temporal) compared to the parietal non-dementia group ($p < 0.001$), suggesting an increase in overall deposit size with dementia.

- For **PC2**, the parietal dementia group showed significantly increased complexity compared to all other groups ($p < 0.05$). Notably, the temporal dementia group had significantly lower complexity scores than all others ($p < 0.001$), indicating a region-specific morphological divergence in the presence of dementia.
- For **PC3**, scores were highest in the parietal dementia group compared to all others ($p < 0.001$). Within both brain regions, the dementia groups exhibited significantly higher scores than their non-dementia counterparts ($p < 0.001$), reinforcing the relevance of this component in capturing dementia-associated traits.

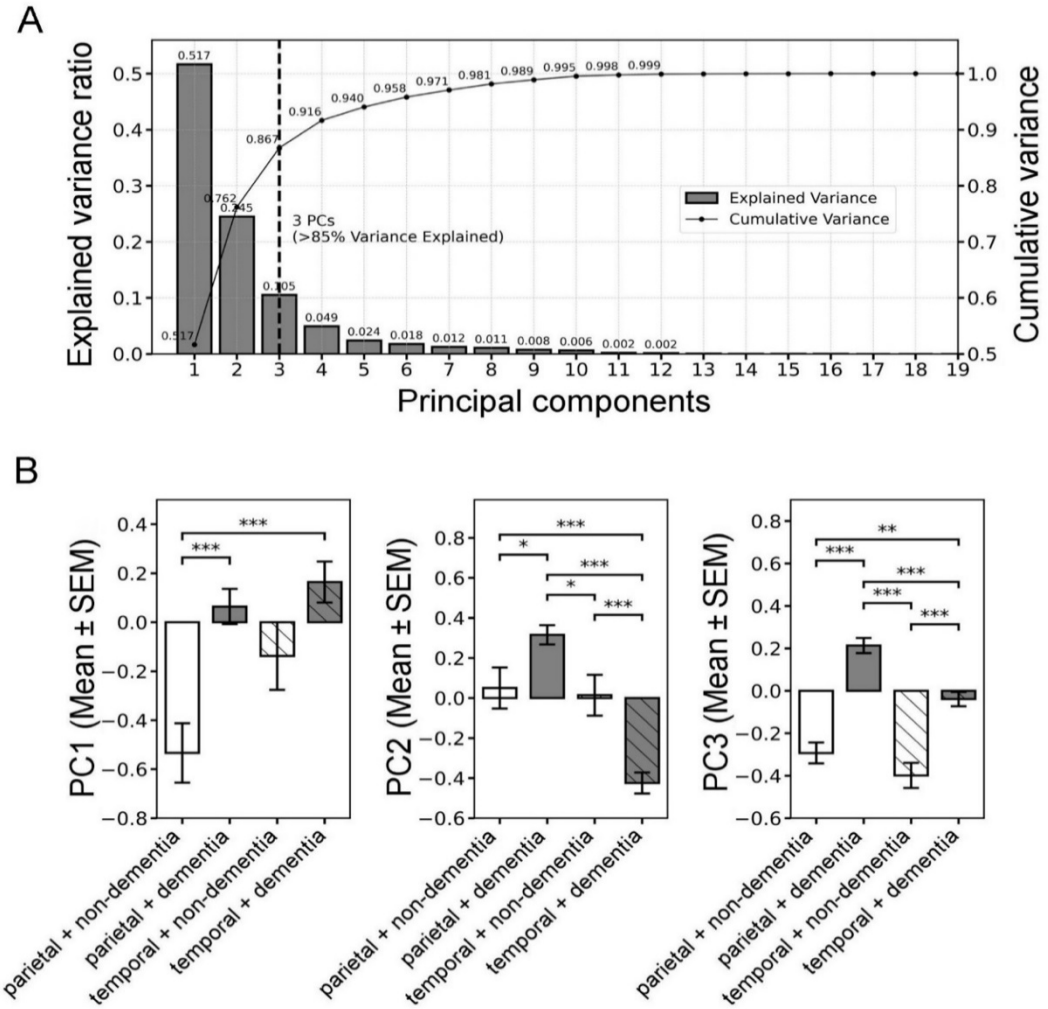

Figure 8. PCA of deposit morphometry elucidates region- and dementia-specific tendencies. (**A**) The scree plot illustrates the proportion of variance explained by each PC derived from the 19 morphometric features (**bars**) and the cumulative variance captured by successive components (**line**). The first three PCs collectively capture over 85% of the total variance, with PC1 alone accounting for more than 50%. (**B**) A group-wise comparison of the scores for these three PCs, which correspond to size-related metrics (PC1), structural complexity (PC2), and geometric symmetry (PC3). Data are presented as bar plots of the mean ± SEM PC-score per plaque, stratified by brain region (parietal = **solid**, temporal = **striped**) and cognitive status (dementia = **dark**, non-dementia = **light**). Asterisks denote levels of statistical significance (* $p < 0.05$, ** $p < 0.01$, *** $p < 0.001$). The results indicate a consistent elevation of scores in the parietal dementia group across all three PCs, suggesting that these plaques are larger, more structurally complex, and geometrically irregular than their non-demented counterparts, though regional differences foreshadow more intricate interplays.

In summary, the analysis of all three PCs indicates that deposit morphology is significantly influenced by both brain region and dementia status. This exploratory quantitative analysis yielded findings consistent with the established heterogeneity of amyloid pathology; it thereby demonstrates the sensitivity of our morphometric profiling methodology to capture biologically relevant variations, supporting the well-documented link between plaque architecture, anatomical location, and the presence of dementia. However, given the limited number of donor cases, these exploratory findings must be interpreted with considerable caution. While the observed trends are intriguing, their generalizability remains to be confirmed, and rigorous validation in larger, more representative cohorts is an essential next step.

4.4 Supplementary findings from collaborative studies[II., III.]

4.4.1 Anti-inflammatory morphological phenotype induced by SZR104[II.]

The quantitative analysis of 974 microglial silhouettes provided a multi-faceted morphological profile of the cell response to the different treatments and statistical evidence for the potent effect of the synthetic compound SZR104 on cellular morphology (Publication II./Supplementary Table S1 and S2). The measurements revealed that while the pro-inflammatory challenge with LPS induced a shift towards a smaller, more amoeboid phenotype, treatment with SZR104 promoted a distinct hypertrophic morphology.

Fundamental metrics of size and shape clearly demonstrated this hypertrophic shift. For instance, a significant, nearly two-fold increase in cellular area was observed (710.79 ± 34.92 μm² vs. 356.08 ± 18.10 μm² in the control condition). Complementing this, the dimensionless transformation index, which quantifies the deviation of a shape from a perfect circle, was also significantly elevated in SZR104-treated cells (2.54 ± 0.10 vs. 2.23 ± 0.11 in control), indicating a more elaborate and less compact cell form. This trend was further substantiated by the analysis of convex hull-based parameters, which characterize the overall spatial footprint of the cell. As a key metric from this category, the convex hull area showed one of the largest significant differences between the control and SZR104-treated conditions. Furthermore, derived dimensionless metrics also captured the increased intricacy of the cell boundary; the roughness, for example, was significantly higher in the SZR104-treated condition (1.3347 ± 0.0173) than in any other experimental setting, reflecting a more detailed cell perimeter. Finally, analysis of morphological complexity using box-counting methods solidified these findings. Such as the fractal dimension, a key parameter quantifying the complexity of a pattern, showed a highly significant ($p < 0.001$) increase in SZR104-treated cells (1.0878 ± 0.0032) compared to the control condition (1.0697 ± 0.0034).

4.4.2 Modulation of p62/SQSTM1 puncta in microglia[III].

The quantitative analysis of p62/SQSTM1-immunoreactive puncta provided key insights into how the autophagic process is modulated by both pro- and anti-inflammatory stimuli in microglia.

A key finding from the analysis was that treatment with the anti-inflammatory agent RST alone led to a significant decrease in the number of p62/SQSTM1-positive puncta per cell ($p < 0.01$ vs. control). This effect, however, was abolished when the final stage of autophagy, autophagosome-lysosome fusion, was inhibited by BAF pretreatment. In the BAF + RST-treated condition, the number of puncta increased significantly ($p < 0.01$) compared to that observed with RST treatment alone, indicating an accumulation of autophagosomes that could not be degraded. Notably, the combined treatment with LPS + RST also resulted in a significant increase ($p < 0.01$) in autophagosome puncta when compared to the decreased levels observed with RST treatment alone. For a comprehensive interpretation of the object-level findings, it is essential to consider the results from the Western blot analysis of total protein levels; however, it should be noted that I did not contribute to this part of the experimental work, which was performed entirely by the collaborating laboratory. The analysis of total soluble p62/SQSTM1 protein levels via Western blot revealed a different, yet related, regulatory pattern. While most treatments without BAF pretreatment only non-significantly increased cytoplasmic p62/SQSTM1 levels, the combined treatment of LPS + RST resulted in a significant increase ($p < 0.05$) over the control; an elevation that was significantly reversed ($p < 0.05$) in the BAF-pretreated LPS + RST group.

5. Discussion

5.1 Weakly supervised segmentation framework[I].

Our findings demonstrate that a weakly supervised pipeline, combining a CAM-based localization model with a U-Net trained on synthetically augmented data, can effectively learn to delineate parenchymal amyloid deposits from histology images. Despite relying on coarse, image-level training labels, the final segmentation model generalized well to manually annotated, pixel-level GT, achieving a robust average DSC of 0.763 across a rigorous, patient-wise cross-validation scheme. This result validates the core premise of our framework: that accurate segmentation of complex histological pathology can be achieved even when supervision is indirect. The SqueezeNet-TAP classifier proved highly effective in its primary role, distinguishing patches with and without parenchymal amyloid with high fidelity (mean F1-score: 97.74%), establishing a reliable foundation for the subsequent stages. Furthermore, the impressive precision (0.877) and recall (0.721) values of the final U-Net model suggest a strong ability to accurately differentiate between deposit and non-deposit regions, a capability directly attributable to the advanced, object-level augmentation strategy. The mild under-

segmentation is a multifaceted and expected outcome of the framework. A primary contributor is the demonstrated ability of the model to rigorously distinguish parenchymal pathology, as confirmed by its exceptionally high specificity (FPR = 0.003), which allows it to correctly exclude confounding vascular elements that are often imprecisely delineated in the semi-automated GT masks. This parenchyma-specific focus, while a key strength of the pipeline, lowers the recall score when measured against this imperfect reference. The residual under-segmentation is an anticipated consequence of the weakly supervised approach, which was never exposed to manually annotated data and employs strict CAM thresholds to prioritize precision.

The design of our prior localization stage was informed by a review of existing CAM methodologies. The landscape of mapping approaches for WSOL is broadly divided into two main families: pooling-based and gradient-based techniques. Pooling-based methods build on the fundamental dichotomy between GAP, which captures the full extent of an object but can dilute key signals, and GMP, which identifies the most discriminative part but ignores the rest [169,277]. This has led to numerous other pooling strategies (e.g., log-sum-exp pooling, Top-K Max-Pooling, Top-GAP, deep-generalized pooling, TAP) [278–281,247]. In parallel, generalized, gradient-based methods offer greater architectural flexibility (e.g., Grad-CAM, Grad-CAM++, Score-CAM, Poly-CAM, HR-CAM) [246,282–285], but their computational overhead, along with persistent mapping resolution limitations or added complexity often make simple pooling-based approaches a more pragmatic choice in WSOL [247]. In the context of our study, our choices were pragmatically driven by the primary goal of training a robust binary classifier for parenchymal amyloid detection. We therefore favored the computational efficiency of a pooling-based CAM, specifically selecting the TAP layer for its ability to retain high activation specificity without discarding lower-activation regions, an approach architecturally supported by our model selection of SqueezeNet, given its inherent suitability due to a default global pooling layer and delayed downsampling. This overall consideration was crucial, given the faint and morphologically heterogeneous presentation of ThioS-positive parenchymal pathology. Our results confirmed that this SqueezeNet + TAP framework learned discriminative representations from a relatively small and heterogeneous dataset, demonstrating robust classification in a rigorous, subject-wise cross-validation scheme. However, as with all weakly supervised methods, a key limitation is the trade-off between classification accuracy and localization precision. Despite our optimizations, the final CAMs, while suitable as coarse initializations for the subsequent segmentation stage, were still limited in spatial resolution. It is also notable that a direct quantitative evaluation of these CAM-derived pseudo-labels was not performed, as this would require substantial additional complexity and offer limited interpretability due to numerous confounding factors (e.g., partial tile overlap, two-level thresholding, and resolution mismatch) inherent in our patch-based, weakly

supervised setup. Nevertheless, the framework provided an effective and efficient solution for generating interpretable activation maps to guide the subsequent segmentation refinement.

In our framework, the coarse localization maps generated by this SqueezeNet-TAP classifier serve as the initial pseudo-labels for a subsequent final refinement stage. For this task, a canonical U-Net architecture was employed to learn the mapping from these noisy, low-resolution heatmaps to precise, pixel-level segmentation masks. The central challenge, however, lies in training this segmentation network effectively without dense, manually annotated GT. To bridge this supervisory gap, our pipeline relies on a sophisticated, on-the-fly synthetic data generation process built upon the principles of object-level augmentation.

The evolution of advanced image-mixing data augmentation strategies, building upon foundational works (e.g., MixUp, CutMix) [162,164] has progressed towards more sophisticated, context-aware, and object-level strategies, particularly for complex tasks like WSSS and medical imaging. A key direction involves the strategic combination of FG objects and BG scenes to combinatorially expand sample diversity (ClassMix, Context Decoupling) [286,287] and the maintenance of local structural integrity for segmentation tasks (e.g., LCAMix, HSMix) [288,289]. A particularly powerful strategy is object-level augmentation, a paradigm largely defined by "Copy-Paste" methodologies. Foundational methods like Cut-Paste-and-Learn [253] established the core pipeline: extracting and storing objects and BGs in databanks, applying transformations, and blending (e.g., Gaussian, Poisson smoothing) them to reduce boundary artifacts. This concept was later simplified by omitting complex context modeling (Simple Copy-Paste) [254], while other approaches have focused on object-aware transformations using BG-inpainting (ObjectAug) [255], varying BGs while preserving FG components (KeepMask and KeepMix) [256], or demonstrating the effectiveness of inter-patient copy-pasting (TumorCP) [257]. A notable refinement is Soft-CP [258], which introduces a sophisticated, erosion/dilation-based blending technique that preserves lesion structure without distorting critical medical information.

Inspired by this rich body of work, our own object-level augmentation pipeline was designed to combine the robustness and advantages of these copy-paste strategies with a novel contour perturbation technique for boundary refinement. Specifically, we integrated a contour perturbation step, adapted from the Restorable Contour Synthesis framework, prior to the Soft-CP blending, to algorithmically generate anatomically plausible shape variations. By embedding a variable number of synthetically altered objects into novel, inpainted BG scenes, our method directly addresses the severe pixel-wise class imbalance of the dataset. Furthermore, by treating the blended boundaries of these embedded objects as unlabeled trimap regions, the pipeline enables the model to infer the uncertain transitional zones. Our method drives the U-Net to learn robust representations and generalize to true

object contours instead of merely overfitting on the overly smooth artifacts characteristic of upscaled CAMs. This approach of using synthetic contours for augmentation adapts a concept employed in texture segmentation, where synthetic mosaics are commonly generated for model training. The goal of this process is to enable the network, once trained on these exemplars with synthetic FG-BG transitions, to accurately segment the fine-grained boundaries of amyloid deposits in their original, in-situ histological context during inference, a capability validated by our rigorous patient-wise cross-validation.

Despite the promising performance of the proposed framework, validated by a stringent patient-wise cross-validation, it is important to acknowledge its primary methodological limitations. The evaluation lacks direct performance comparisons, both against established baseline methods and against a vast array of conceivable alternative approaches (such as those utilizing different model architectures and variants, correction and normalization strategies, loss functions, pooling strategies, augmentation, localization, or refinement techniques, etc.). Furthermore, a comprehensive ablation study to isolate the contribution of each component to the pipeline, most notably, a direct quantitative validation of the CAM-derived priors against the GT, was not performed. The following sections will elaborate on the practical and conceptual rationale that informed these design choices.

A key consideration in the methodology of this study was the trade-off between exhaustive methodological comparison and the practical constraints imposed by a computationally demanding evaluation protocol. The validation framework, which employed a patient-wise 7-fold cross-validation (necessitated training of 7 models) for two sequentially trained models (a classifier and a segmenter) with on-the-fly data augmentation, was inherently resource-intensive. As this setup already necessitated the training of 14 distinct models (7 folds × 2 stages), incorporating additional variants, baseline or extensive ablation studies would have multiplicatively increased the required computational cost and training time, which was deemed beyond the scope of this proof-of-concept study.

Furthermore, constructing a fair and direct comparison against a conventional, fully supervised baseline is a non-trivial task, complicated by several dataset-specific factors that would compromise the transparency and validity of such an analysis. These challenges, stemming from the inherent nature of our patch-based, weakly supervised setup, affect both the training and evaluation phases. A primary obstacle is the severe FG-BG imbalance, present at both the full-image and patch levels, which is known to destabilize the training of standard segmentation models without advanced augmentation and/or specialized loss functions. Our preliminary experiments confirmed this, where the sparse occurrence of amyloid deposits often led to model collapse and null predictions, a failure mode that our object-level augmentation strategy was specifically designed to mitigate. Additional complications arise from the patch-based sampling strategy itself. A baseline trained on a re-sampled,

densely annotated version of the patch dataset would face a different data distribution than our weakly supervised model. Moreover, any patch-level evaluation, whether on the original or a re-sampled version of the dataset, would be confounded by the redundancy from partially overlapping tiles. Training a baseline on the original patch dataset is particularly challenging, as the high proportion (~50%) of entirely plaque-free negative patches further exacerbates the pixel-wise imbalance. Finally, the quality of the semi-automated GT annotations poses its own challenge. The semi-automated GT masks are often less refined in distinguishing plaques from adjacent or embedded vascular elements. Consequently, a baseline trained on this imperfect data could be penalized for correctly separating these structures, thus limiting the value of a direct comparison. (Though multi-expert labeling could add value in future work.) Given these profound methodological challenges, we concluded that a simple baseline would not provide a meaningful or fair benchmark for our framework.

A further methodological limitation of this study is the omission of a direct quantitative validation of the CAM-derived priors, which could be considered a form of ablation experiment. While such an evaluation could offer valuable insights in weakly supervised setups, it was deemed infeasible due to several insurmountable technical and conceptual barriers inherent in our methodological design. A direct comparison at the patch level is also confounded by the partially overlapping nature of the tiles, which introduces a minor but non-negligible redundancy (that can also be considered a form of augmentation), complicating the interpretation of per-patch metrics. Furthermore, objects are overrepresented in positive patches causing FG-BG distributional bias compared to the full-image context. A meaningful evaluation of negative, plaque-free patches is itself problematic, as the relative min-max normalization of CAM intensities would still produce apparent "positive" regions even in the complete absence of a target signal (due to the lack of a separate weight set for the BG class in the binary classifier). Alternatively, reconstructing full-image pseudo-labels from the patch-based CAMs for a more direct comparison is a non-trivial task. The original CAMs are low-resolution and reflect relative intensity distributions rather than precise object boundaries. Such a reconstruction would introduce complex challenges in aligning intensity scales across patches and ensuring their seamless integration. These issues would require substantial architectural adaptations or additional post-processing, particularly given that a single plaque may appear in multiple (overlapping or adjacent) patches with slightly different activations due to contextual variance (e.g., partial visibility or the presence of more prominent visual cues within the patch). The issue of normalizing plaque-free patches, as mentioned earlier, would persist even in a full-image reconstruction scenario. Furthermore, we highlight that the pseudolabel generation process involved a deliberately strict primary threshold to define confident positive regions, while a secondary threshold was used to exclude uncertain areas. As a result, these thresholded CAMs are not directly comparable to binary GT masks in a conventional sense.

Therefore, it is important to emphasize that the CAMs in our framework are not intended as final segmentation outputs, but rather as coarse, spatially informative priors to initialize the refinement model. The purpose of the subsequent U-Net stage is not merely to enhance resolution and sharpen object contours, but to learn the mapping from these noisy initializations to reconstruct the high-fidelity full-image segmentation in a patch-based manner. Thus, there is no straightforward way to perform a comparison analogous to an ablation study with the final UNet-based segmentation without introducing substantial technical complexity and limited interpretability.

Consequently, we opted to treat the pipeline as a unified system and evaluate its final, end-to-end performance rather than engaging in per-module benchmarking against baseline methods or through ablation studies. This approach, validated through stringent patient-wise cross-validation, yields metrics that most accurately reflect the practical utility of the framework. As a proof-of-concept, the primary objective was not to optimize for state-of-the-art segmentation performance in absolute terms, but to demonstrate the viability of a WSSS pipeline for segmenting ThioS-positive amyloid plaques in human tissue sections using relatively straightforward, reproducible methods. Our framework combines well-established benchmark architectures (SqueezeNet and a vanilla U-Net) with an extensive object-level augmentation strategy. The novelty of our work lies in the effective integration of these components into a weakly supervised framework tailored to the specific challenges of ThioS-stained histopathology. The focus was therefore placed on general applicability across individuals, biological interpretability, and feasibility in low-annotation regimes, while the framework was intentionally kept modular and lightweight to facilitate further fine-tuning, extension, or adaptation to other contexts in future work.

While a direct, component-wise benchmarking against baseline or alternative model variants was beyond the scope of this study for the reasons previously outlined, placing our results in the context of recent, related works can help assess the performance of our framework. Although the results from these studies are only partially comparable due to substantial methodological differences (e.g., in staining, annotation strategies, and data sources), they address the shared challenge of weakly supervised amyloid plaque segmentation and thus serve as valuable points of reference. The first, by Chen et al. (2023) [204], applied a weakly supervised approach to segment whole-brain 3D data from a single transgenic rat model using Congo Red staining, achieving a DSC of 0.78 and a recall of 0.84 in the cortex. Despite some conceptual similarities, our study faced considerably more challenging conditions: we analyzed 2D histological sections from multiple human donors, contending with significant anatomical variability, high BG noise, marked vasculature, staining artifacts, and the complex morphological heterogeneity of human plaques. In this more challenging context, our average DSC of 0.763 and recall of 0.721 can be considered highly competitive. A second recent work by Müller

et al. (2025) [206] analyzed unstained human tissue using thresholded immunohistochemical labeling to generate GT, and reported a segmentation precision of 0.57, a metric where our framework achieved a substantially higher score of 0.877. While their classification module reached an F1-score of 0.94, ours performed comparably at 0.977 at the patch level.

However, given the profound differences in tissue preparation, staining, and annotation protocols, these numerical comparisons should not be overinterpreted as direct performance rankings. Rather, they underscore the diversity of current approaches in the field and highlight the practical relevance and robustness of our pipeline, particularly when applied to the technically complex domain of ThioS-stained human brain sections.

5.2 Heterogeneity of amyloid deposits[I.]

The concluding phase of our work involved a comprehensive, object-level morphometric profiling of amyloid deposits, leveraging the high-fidelity, automatically segmented masks to provide a detailed perspective on their characteristics across spatial extent, internal structural arrangement, shape symmetry, and staining properties. Utilizing a rich set of 19 distinct parameters derived from each segmented deposit, we investigated these features as a function of both brain region and cognitive status. This approach uncovered latent variations in the dataset, which were elucidated through dimensionality reduction technique and subsequent statistical analysis. PCA successfully decomposed the high-dimensional morphometric dataset into a simplified, low-dimensional representation defined by three orthogonal components (PC1–3), each of which isolated a distinct, biologically meaningful aspect of plaque architecture. Subsequent group-wise statistical comparisons of these PCs revealed significant differences between the experimental groups, as detailed in the following sections.

The first component (PC1), which accounted for the largest portion of the variability (>50%), was predominantly driven by physical dimensions of the amyloid aggregates. The group of metrics quantifying magnitude in log-scale (e.g., area, perimeter, and convex hull metrics) exhibited uniform, strong contributions to this component, confirming its interpretation as a general "size-related" axis. Consistently, integrated density as the total fluorescence measure, also correlated strongly with PC1, reinforcing the relationship between overall fluorescent staining uptake and plaque size. Our results indicated that PC1 scores were markedly greater in the dementia groups, particularly in the parietal cortex, where the difference was statistically significant, aligning with established neuropathological evidence linking increased cortical amyloid accumulation to severe stages of the disease and cognitive impairment [4]. This finding implies that the sheer physical extent of these structures constitutes the foremost characteristic for their differentiation and is likely related to their pathogenic impact or their indicative role in the overall disease progression.

The second component (PC2) was primarily defined by metrics of morphological and architectural complexity and heterogeneity. This axis was determined by a combination of non-linear, scale-invariant descriptors including fractal dimension and lacunarity, as well as measures of compactness, including circularity and solidity. Fractal dimension, which loaded positively onto PC2, provides insight into structural complexity and self-similarity properties of biological structures and textures, and is widely applied in the analysis of both cellular and non-cellular components, including the Aβ aggregates in AD [24,267,268,290–292]. Our findings regarding fractal dimension are partly consistent with prior reports of increased complexity in advanced dementia [24], a trend we also observed in the parietal region. However, the opposing trend in the temporal dementia group suggests the presence of region-specific pathological trajectories. It is also pertinent to consider that our methodological decision to strictly exclude vasculature during segmentation could have influenced this metric, as such elements can contribute to the perceived structural complexity. Lacunarity, conversely, exhibited a strong negative loading on PC2, indicating a tendency opposite to the complexity captured by fractal dimension, potentially reflecting either the presence of looser, more fragmented diffuse structures or the internal structural heterogeneity of the compact forms. Similarly, boundary variability, as measured by roughness, also loaded negatively on this axis. In stark contrast, circularity and solidity showed strong positive weightings, as higher values for these metrics are indicative of greater compactness and a simpler, denser morphology. Indeed, circularity has previously been leveraged for the morphological classification of ThioS-positive plaques as a direct measure of their compactness [44,269]. The diffuseness index, which quantifies the proportion of faintly stained, diffuse subregions [55], also loaded negatively onto PC2, underscoring its role in capturing spatial dispersion and a lack of compactness. The observed increase of PC2 scores in the parietal dementia cases, coupled with their decrease in the temporal lobe, may therefore signify a region-specific morphological divergence. This suggests a shift towards more compact, well-organized, and geometrically structured plaques in the parietal cortex of dementia patients, while those in the temporal region potentially develop more irregular, fragmented characteristics. This complex interplay of these morphometric features suggests that PC2 reflects nuanced, region-specific changes in plaque maturation and organization.

The third component (PC3) captured global geometric information, primarily related to plaque elongation and asymmetry. Driven by increases in anisotropy measures (including span ratio and max/min radius, which loaded positively) and decreases in shape symmetry properties (represented by hull circularity, which loaded negatively), the significant elevation of PC3 scores in both dementia groups collectively suggests a morphological shift towards more elongated and asymmetrical plaque forms in the diseased brain, regardless of region. While these geometric descriptors are less conventionally assessed in traditional neuropathology of amyloid plaques, prior observations of region-

specific patterns do exist [204]. Therefore, these features may offer additional insight into plaque growth dynamics, potentially reflecting underlying pathological processes such as vascular interactions or factors promoting anisotropic deposition.

In summary, our high-dimensional morphometric profiling successfully decoupled general dementia-associated trends from more nuanced, region-specific alterations in plaque morphology. While increased plaque size and geometric anisotropy emerged as consistent trends associated with the dementia status, the analysis of structural complexity revealed intricate, divergent pathological trajectories between cortical regions. This finding underscores that amyloid pathology is a spatially heterogeneous phenomenon, likely shaped by local microenvironmental factors. Crucially, this level of insight was only achievable by incorporating a rich set of non-traditional descriptors (e.g., scale-invariant, and convex hull-based measurements), demonstrating the potential of high-content morphometrics to provide more sensitive readouts for understanding the multifaceted nature of AD.

It is crucial to contextualize these findings within the limitations of the present study. While the number of individual deposits analyzed was substantial, the analysis was based on a small cohort of seven donor cases. Consequently, all statistical comparisons must be considered exploratory, and making broad claims about differences between the experimental groups should be approached with considerable prudence, as the limited scope of the dataset precludes definitive generalizations to the broader population. The primary objective of this morphometric analysis was therefore not to establish definitive biomarker-level relationships, but rather to demonstrate the technical viability and potential of our automated segmentation and analysis pipeline. Viewed from this perspective, the consistent patterns observed across the PCs should be regarded as promising, hypothesis-generating findings rather than conclusive evidence. They support the utility of high-content morphometric profiling as a valuable addition to the neuropathological research toolkit and illustrate the feasibility and scalability of our framework. However, the statistical robustness of these patterns remains fundamentally constrained. Future work incorporating larger and more diverse patient populations across multiple brain areas will be essential to validate, refine, and ultimately explore the true histopathological potential of these initial findings.

5.3 Future directions[I.]

The presented weakly supervised framework serves as a robust proof-of-concept, its strong generalization in a rigorous, patient-wise cross-validation stems from its demonstrated ability to distinguish parenchymal pathology from confounding elements like vascular amyloid based on learned semantic features. This enables the object-level profiling of individual plaques, a task not feasible for automated analysis based on the ThioS stain alone.

Its future technical development should therefore focus on enhancing this methodological sophistication and deepening its biological insights. A crucial next step is to move beyond the current baseline architectures and procedures through fine-tuning and by exploring more advanced, data-intensive components, such as incorporating attention mechanisms for localization and segmentation, and enhancing the augmentation pipeline with generative models to create a large-scale dataset.

The primary goal is to leverage this enhanced and validated framework on larger and more diverse patient cohorts, moving beyond the exploratory findings of this small-cohort study to establish definitive, quantitative relationships and trends between the high-content morphometric features and the neuropathological status or brain region of the tissue, thus providing a powerful and objective methodology for scalable plaque analysis.

Furthermore, this pursuit of robust, automated analysis could be particularly relevant in the context of emerging *in vivo* diagnostic applications. The foundation for *in vivo* amyloid imaging and the challenges of translating ex vivo findings are exemplified by preclinical validation studies of brain-penetrating tracers. Although the charged ThioS molecules poorly penetrate the BBB, their histological binding patterns are identical to those of the widely used *in vivo* amyloid tracer, Pittsburgh Compound B (e.g., both label vascular and parenchymal amyloid, and weakly stain diffuse deposits) [40]. Crucially, since such tracers are often also fluorescent, their *in vivo* distribution and behavior can be studied in animal models with high-resolution multiphoton microscopy, yielding a preclinical validation platform of novel *in vivo* imaging agents intended for lower-resolution clinical modalities [40], where the resulting microscopic data could present similar segmentation and analysis challenges in interpreting complex structural characteristics like ThioS-stained histological sections, highlighting the need for robust, data-efficient analysis pipelines.

Significant challenges in brain imaging have spurred the investigation of the retina as a more accessible surrogate for cerebral Aβ deposits. One recent study outlines a potential *in vivo* imaging strategy for the early detection, therapeutic response monitoring, and population screening of AD through retinal imaging. Its central innovation is an aerosolized delivery method that enables the *in vivo* application of classical Aβ-binding dyes with limited BBB permeability, like ThioS [293]. It was demonstrated in a mouse model that inhaled ThioS stains retinal Aβ deposits, which are significantly associated with retinal ganglion cells, thereby circumventing the challenges of expensive brain imaging and the development of BBB-penetrating probes, creating a pathway for a cost-effective, non-invasive (cellular-level) retinal optical imaging method, anticipating the critical importance of automation in *in vivo* image analysis. A parallel strategy aims to eliminate the need for physical dyes altogether. This study introduces a ML-based method to identify AD-associated retinal amyloid deposits, addressing the low specificity of polarimetry, which, despite detecting fibrillar structures in the

retina that reflect brain pathology, also identifies false positives alongside ThioS-positive (true positive) amyloid deposits [294]. To this end, researchers trained classical ML models (linear discriminant analysis, support vector machine, random forests) on polarimetric feature vectors extracted from pre-segmented deposits in post-mortem human retinal samples, proving that the polarimetric "fingerprint" is sufficient for the high-accuracy prediction of ThioS fluorescence, a critical step towards a future, non-invasive, dye-free optical diagnostic procedure for *in vivo* application. Such a procedure could be greatly enhanced by modern, end-to-end DL frameworks for real-time clinical analysis.

Finally, given the modular design of our framework, its methodology is not inherently stain-specific and can be adapted to other contexts where manual annotations are scarce. Future work could extend this approach to different histopathological targets (e.g., Lewy body pathology), alternative staining protocols (e.g., Congo Red), transgenic animal models, and even to other imaging modalities, including volumetric datasets and *in vivo* imaging approaches.

5.2 Supplementary implications for collaborative studies[II., III.]

5.4.1 Confirming pharmacological effects through objective cytomorphometry[II.]

Microglial cytomorphology is a widely analyzed biomarker in both *in vivo* and *in vitro* settings as a key function of cellular physiology. While *in vivo* morphology is more complex and largely influenced by environmental factors, *in vitro* analysis of digital silhouettes is facilitated by the flattened cellular structure and simplified culturing conditions. Upon activation by diverse (patho)physiological stimuli, microglia transition from a ramified to an activated, often amoeboid [208] and/or hypertrophic [212] phenotype, while dystrophic microglia without hypertrophy are also observed in AD [213].

The quantitative data from this collaborative study substantiate the established anti-inflammatory properties of SZR104. Collectively, the observed changes, indicating cellular enlargement and increased morphological complexity, are consistent with the development of a hypertrophic phenotype, which in this context is interpreted as an anti-inflammatory response. Our findings demonstrate that SZR104 not only suppresses biochemical markers but also effectively inhibits the pro-inflammatory morphological shift induced by LPS. This aligns with previous *in vivo* and *in vitro* studies establishing the ability of SZR104 to suppress inflammatory markers and phagocytosis [216,217]. The hypertrophic phenotype induced by SZR104 is remarkably similar to that caused by other well-known anti-inflammatory drugs like RST and aspirin [232,233], suggesting a shared pathway potentially involving the actin cytoskeleton [214]. Based on these quantitative parallels, the hypertrophic enlargement of the cell somata and the formation of filopodia can be interpreted as a signature of SZR104-induced anti-inflammatory processes in microglia.

Although SZR104 is a structural analog of the endogenous KYNA, it is not a complete functional

analog, differing critically in its ability to cross the BBB. Furthermore, the quantitative morphometric data strongly indicate that SZR104 has a more potent anti-inflammatory effect on microglia, positioning it as a potential target molecule for exploring the KYNA pathway *in vivo*. Ultimately, this work demonstrates that quantitative cytomorphometry analysis can provide valuable predictive information as a powerful tool for characterizing the biological activity of pharmacological compounds, offering an objective and reproducible alternative to subjective visual assessment.

5.4.2 Unraveling complex cellular dynamics via quantitative puncta analysis[III].

The quantitative analysis of p62/SQSTM1 puncta proved essential for interpreting the complex, multifaceted regulatory pattern of autophagy observed in the second collaborative study. Notably, beyond its role in autophagy, p62/SQSTM1 participates in complex signaling pathways, including proteasomal degradation and the regulation of protein aggregate formation. [225,227,228]. Pharmacological autophagy inhibitors like BAF, which block the final autophagosome-lysosome fusion stage, are indispensable tools for quantifying autophagic activity under different conditions [236,237]; additionally, the observed effects of BAF in our study were consistent with its established cytostatic properties described in the literature [238].

The literature presents a complex and contradictory picture of autophagy regulation, as exemplified by the conflicting effects of both inflammatory stimuli like LPS, which can have either inhibitory or inductive effects in microglia depending on the experimental context [224,225,229,230], and anti-inflammatory pharmacological agents like statins, where different compounds (e.g., RST vs. atorvastatin) have been reported to yield opposing results in different cell lines [234,235]. Our findings may help to interpret these inconsistencies, as we observed that while RST alone significantly decreased the number of p62/SQSTM1-labeled puncta, this effect was abolished by BAF pretreatment, resulting in a significant accumulation compared to RST alone, demonstrating a genuine modulation of the autophagic process, while the total p62/SQSTM1 levels showed only a negligible, non-significant increase (regardless of BAF pretreatment) in the same treatment groups. This accumulation of autophagosomes highlights the distinct dynamics between the soluble and aggregated pools of p62/SQSTM1 that may not be captured by bulk biochemical assays. Our study further revealed complex regulatory effects. The combined LPS and RST treatment led to an accumulation of both total p62/SQSTM1 protein (an elevation reversed by BAF) and autophagic puncta. In contrast, when applied individually, these treatments tended to decrease the number of puncta (a significant reduction with RST), pointing towards divergent, context-dependent regulatory mechanisms where the interaction of inflammatory and anti-inflammatory stimuli alters the autophagic outcome. The final number of puncta is likely governed by intricate regulatory networks and given that the effects of such

compounds are not always straightforward, this detailed, object-level analysis proved essential for mapping these complex dynamics and revealing the nuanced nature of autophagy regulation in microglia.

6. Acknowledgements

I would first like to express my sincere gratitude to my PhD supervisor, Professor Károly Gulya, for his invaluable guidance, professional mentorship, and unwavering support throughout my research. My scientific work was conducted within the institutional frameworks of the Department of Cell Biology and Molecular Medicine and the Department of Medical Physics and Informatics. I am particularly grateful to Dr. József Tolnai, Dr. Tibor Nyári, Dr. Edina Petákné Rátkai, Professor László Tiszlavicz and Professor Balázs Gulyás, the few individuals whose professional integrity and constructive scientific dialogues were of genuine value. I also wish to extend my special thanks to Dr. István Pesti and Dr. Melinda Szabó, the lead authors of our collaborative studies, for the productive teamwork and the opportunity to contribute to their research projects. I am also grateful to the institutional staff for their invaluable technical support. Finally, deepest thanks to my family for their unwavering encouragement.

This Thesis is based on research funded by the following resources: Ministry of National Resources (GINOP 2.3.2-15-2016-00030 and 2.3.2-15-2016-00034) through the European Union Cohesion Fund; the Netherlands Brain Bank, Netherlands Institute for Neuroscience, Amsterdam (for providing the human brain tissue to the cooperation between the Department of Clinical Neuroscience, Karolinska Institute, Stockholm, Sweden, and the Department of Cell Biology and Molecular Medicine, Szeged, Hungary); the Doctoral School of Experimental and Preventive Medicine (formerly Doctoral School of Theoretical Medicine), Albert Szent-Györgyi Medical School, University of Szeged, for providing my stipendium.

7. References

1. Braak, H., & Braak, E. (1991). Neuropathological stageing of Alzheimer-related changes. Acta Neuropathologica, 82(4), 239–259. https://doi.org/10.1007/bf00308809
2. Arendt, T., Stieler, J., & Ueberham, U. (2017). Is sporadic Alzheimer's disease a developmental disorder? Journal of Neurochemistry, 143(4), 396–408. https://doi.org/10.1111/jnc.14036
3. DeTure, M. A., & Dickson, D. W. (2019). The neuropathological diagnosis of Alzheimer's disease. Molecular Neurodegeneration, 14(1), 32. https://doi.org/10.1186/s13024-019-0333-5
4. Walker, L. C. (2020). Aβ plaques. Free neuropathology, 1, 31. https://doi.org/10.17879/freeneuropathology-2020-3025
5. Koychev, I., Hofer, M., & Friedman, N. (2020). Correlation of Alzheimer Disease Neuropathologic Staging with Amyloid and Tau Scintigraphic Imaging Biomarkers. Journal of Nuclear Medicine, 61(10), 1413–1418. https://doi.org/10.2967/jnumed.119.230458
6. Serrano-Pozo, A., Frosch, M. P., Masliah, E., & Hyman, B. T. (2011). Neuropathological alterations in Alzheimer disease. Cold Spring Harbor Perspectives in Medicine, 1(1), a006189. https://doi.org/10.1101/cshperspect.a006189
7. Farfara, D., Lifshitz, V., & Frenkel, D. (2008). Neuroprotective and neurotoxic properties of glial cells in the pathogenesis of Alzheimer's disease. Journal of Cellular and Molecular Medicine, 12(3), 762–780. https://doi.org/10.1111/j.1582-4934.2008.00314.x
8. Thal, D. R., Rüb, U., Orantes, M., & Braak, H. (2002). Phases of Aβ-deposition in the human brain and its relevance for the development of AD. Neurology, 58(12), 1791–1800. https://doi.org/10.1212/wnl.58.12.1791
9. Thal, D. R., Capetillo-Zarate, E., Del Tredici, K., & Braak, H. (2006). The Development of Amyloid β Protein Deposits in the Aged Brain. Science of Aging Knowledge Environment, 2006(6), re1. https://doi.org/10.1126/sageke.2006.6.re1
10. Fakhoury, M. (2018). Microglia and astrocytes in Alzheimer's disease: Implications for therapy. Current Neuropharmacology, 16(5), 508–518. https://doi.org/10.2174/1570159x15666170720095240
11. Almeida, Z. L., Vaz, D. C., & Brito, R. M. M. (2025). Morphological and molecular profiling of amyloid-B species in Alzheimer's pathogenesis. Molecular Neurobiology, 62(4), 4391–4419. https://doi.org/10.1007/s12035-024-04543-4
12. Armstrong, R. (1998). B-Amyloid plaques: stages in life history or independent origin? Dementia and Geriatric Cognitive Disorders, 9(4), 227–238. https://doi.org/10.1159/00001705
13. Mirra, S. S., Heyman, A., McKeel, D., Sumi, S. M., Crain, B. J., Brownlee, L. M., Vogel, F. S., Hughes, J. P., van Belle, G., & Berg, L. (1991). The Consortium to Establish a Registry for Alzheimer's Disease (CERAD). Part II. Standardization of the neuropathologic assessment of Alzheimer's disease. Neurology, 41(4), 479–486. https://doi.org/10.1212/wnl.41.4.479
14. Jankovska, N., Olejar, T., & Matej, R. (2021). Extracellular protein aggregates colocalization and neuronal dystrophy in comorbid Alzheimer's and Creutzfeldt–Jakob disease: A micromorphological pilot study on 20 brains. International Journal of Molecular Sciences, 22(4), 2099. https://doi.org/10.3390/ijms22042099
15. Hyman, B. T., Phelps, C. H., Beach, T. G., Bigio, E. H., Cairns, N. J., Carrillo, M. C., Dickson, D. W., Duyckaerts, C., Frosch, M. P., Masliah, E., Mirra, S. S., Nelson, P. T., Schneider, J. A., Thal, D. R., Thies, B., Trojanowski, J. Q., Vinters, H. V., & Montine, T. J. (2012). National Institute on Aging-Alzheimer's Association guidelines for the neuropathologic assessment of Alzheimer's disease. Alzheimer's & Dementia, 8(1), 1–13. https://doi.org/10.1016/j.jalz.2011.10.007
16. Montine, T. J., Phelps, C. H., Beach, T. G., Bigio, E. H., Cairns, N. J., Dickson, D. W., Duyckaerts, C., Frosch, M. P., Masliah, E., Mirra, S. S., Nelson, P. T., Schneider, J. A., Thal, D. R., Trojanowski, J. Q., Vinters, H. V., & Hyman, B. T. (2012). National Institute on Aging–Alzheimer's Association guidelines for the neuropathologic assessment of Alzheimer's disease: a

practical approach. Acta Neuropathologica, 123(1), 1–11. https://doi.org/10.1007/s00401-011-0910-3
17. Cole, S. L., & Vassar, R. (2007). The Alzheimer's disease Beta-secretase enzyme, BACE1. Molecular Neurodegeneration, 2(1), 22. https://doi.org/10.1186/1750-1326-2-22
18. Mawuenyega, K. G., Kasten, T., Sigurdson, W., & Bateman, R. J. (2013). Amyloid-beta isoform metabolism quantitation by stable isotope-labeled kinetics. Analytical Biochemistry, 440(1), 56–62. https://doi.org/10.1016/j.ab.2013.04.031
19. Lauritzen, I., Pardossi-Piquard, R., Bauer, C., Brigham, E., Abraham, J. D., Ranaldi, S., Fraser, P., St-George-Hyslop, P., Le Thuc, O., Espin, V., Chami, L., Dunys, J., & Checler, F. (2012). The β-secretase-derived C-terminal fragment of βAPP, C99, but not Aβ, is a key contributor to early intraneuronal lesions in triple-transgenic mouse hippocampus. Journal of Neuroscience, 32(46), 16243–1655a. https://doi.org/10.1523/jneurosci.2775-12.2012
20. Kametani, F., & Hasegawa, M. (2018). Reconsideration of amyloid hypothesis and tau hypothesis in Alzheimer's disease. Frontiers in Neuroscience, 12, 25. https://doi.org/10.3389/fnins.2018.00025
21. Hardy, J., & Selkoe, D. J. (2002). The amyloid hypothesis of Alzheimer's disease: progress and problems on the road to therapeutics. Science, 297(5580), 353–356. https://doi.org/10.1126/science.1072994
22. Jiang, Q., Lee, C. Y., Mandrekar, S., Wilkinson, B., Cramer, P., Zelcer, N., Mann, K., Lamb, B., Willson, T. M., Collins, J. L., Richardson, J. C., Smith, J. D., Comery, T. A., Riddell, D., Holtzman, D. M., Tontonoz, P., & Landreth, G. E. (2008). ApoE promotes the proteolytic degradation of Abeta. Neuron, 58(5), 681–693. https://doi.org/10.1016/j.neuron.2008.04.010
23. Koistinaho, M., Lin, S., Wu, X., Esterman, M., Koger, D., Hanson, J., Higgs, R., Liu, F., Malkani, S., Bales, K. R., & Paul, S. M. (2004). Apolipoprotein E promotes astrocyte colocalization and degradation of deposited amyloid-beta peptides. Nature Medicine, 10(7), 719–726. https://doi.org/10.1038/nm1058
24. Pirici, D.; Van Cauwenberghe, C.; Van Broeckhoven, C.; Kumar-Singh, S. (2009). Fractal analysis of amyloid plaques in Alzheimer's disease patients and mouse models. Neurobiology of Aging, 32(9), 1579–1587. https://doi.org/10.1016/j.neurobiolaging.2009.10.010
25. Boon, B., Bulk, M., Jonker, A. J., Morrema, T., van den Berg, E., Popovic, M., Walter, J., Kumar, S., van der Lee, S. J., Holstege, H., Zhu, X., Van Nostrand, W. E., Natté, R., van der Weerd, L., Bouwman, F. H., van de Berg, W., Rozemuller, A., & Hoozemans, J. (2020). The coarse-grained plaque: a divergent Aβ plaque-type in early-onset Alzheimer's disease. Acta Neuropathologica, 140(6), 811–830. https://doi.org/10.1007/s00401-020-02198-8
26. Dickson, T., & Vickers, J. (2001). The morphological phenotype of β-amyloid plaques and associated neuritic changes in Alzheimer's disease. Neuroscience, 105(1), 99–107. https://doi.org/10.1016/s0306-4522(01)00169-5
27. Kuo, Y. M., Kokjohn, T. A., Beach, T. G., Sue, L. I., Brune, D., Lopez, J. C., Kalback, W. M., Abramowski, D., Sturchler-Pierrat, C., Staufenbiel, M., & Roher, A. E. (2001). Comparative analysis of amyloid-beta chemical structure and amyloid plaque morphology of transgenic mouse and Alzheimer's disease brains. Journal of Biological Chemistry, 276(16), 12991–12998. https://doi.org/10.1074/jbc.M007859200
28. Röhr, D., Boon, B., Schuler, M., Kremer, K., Hoozemans, J., Bouwman, F. H., El-Mashtoly, S. F., Nabers, A., Großerueschkamp, F., Rozemuller, A., & Gerwert, K. (2020). Label-free vibrational imaging of different Aβ plaque types in Alzheimer's disease reveals sequential events in plaque development. Acta Neuropathologica Communications, 8(1), 222. https://doi.org/10.1186/s40478-020-01091-5
29. Huang, Y., Happonen, K. E., Burrola, P. G., O'Connor, C., Hah, N., Huang, L., Nimmerjahn, A., & Lemke, G. (2021). Microglia use TAM receptors to detect and engulf amyloid β plaques. Nature Immunology, 22(5), 586–594. https://doi.org/10.1038/s41590-021-00913-5

30. Armstrong, R. A., Myers, D., & Smith, C. U. (1997). Factors determining the size frequency distribution of beta-amyloid (A beta) deposits in Alzheimer's disease. Experimental Neurology, 145(2 Pt 1), 574–579. https://doi.org/10.1006/exnr.1997.6465
31. Hyman, B. T., West, H. L., Rebeck, G. W., Buldyrev, S. V., Mantegna, R. N., Ukleja, M., Havlin, S., & Stanley, H. E. (1995). Quantitative analysis of senile plaques in Alzheimer disease: observation of log-normal size distribution and molecular epidemiology of differences associated with apolipoprotein E genotype and trisomy 21 (Down syndrome). Proceedings of the National Academy of Sciences, 92(8), 3586–3590. https://doi.org/10.1073/pnas.92.8.3586
32. Nilsson, L. N., Bales, K. R., DiCarlo, G., Gordon, M. N., Morgan, D., Paul, S. M., & Potter, H. (2001). Alpha-1-antichymotrypsin promotes beta-sheet amyloid plaque deposition in a transgenic mouse model of Alzheimer's disease. Journal of Neuroscience, 21(5), 1444–1451. https://doi.org/10.1523/JNEUROSCI.21-05-01444.2001
33. Reinke, A. A., & Gestwicki, J. E. (2011). Insight into amyloid structure using chemical probes. Chemical Biology & Drug Design, 77(6), 399–411. https://doi.org/10.1111/j.1747-0285.2011.01110.x
34. Luo, Z., Xu, H., Liu, L., Ohulchanskyy, T. Y., & Qu, J. (2021). Optical imaging of Beta-Amyloid plaques in Alzheimer's disease. Biosensors, 11(8), 255. https://doi.org/10.3390/bios11080255
35. MacKeigan, T. P., Morgan, M. L., & Stys, P. K. (2023). Quantitation of tissue amyloid via fluorescence spectroscopy using controlled concentrations of Thioflavin-S. Molecules, 28(11), 4483. https://doi.org/10.3390/molecules28114483
36. Sun, A., Nguyen, X. V., & Bing, G. (2002). Comparative analysis of an improved thioflavin-s stain, Gallyas silver stain, and immunohistochemistry for neurofibrillary tangle demonstration on the same sections. Journal of Histochemistry and Cytochemistry, 50(4), 463–472. https://doi.org/10.1177/002215540205000403
37. Rajamohamedsait, H. B., & Sigurdsson, E. M. (2012). Histological staining of amyloid and pre-amyloid peptides and proteins in mouse tissue. Methods in Molecular Biology, 849, 411–424. https://doi.org/10.1007/978-1-61779-551-0_28
38. Ly, P. T., Cai, F., & Song, W. (2011). Detection of neuritic plaques in Alzheimer's disease mouse model. Journal of Visualized Experiments, (53), 2831. https://doi.org/10.3791/2831
39. Groenning M. (2010). Binding mode of Thioflavin T and other molecular probes in the context of amyloid fibrils-current status. Journal of Chemical Biology, 3(1), 1–18. https://doi.org/10.1007/s12154-009-0027-5
40. Bacskai, B. J., Hickey, G. A., Skoch, J., Kajdasz, S. T., Wang, Y., Huang, G. F., Mathis, C. A., Klunk, W. E., & Hyman, B. T. (2003). Four-dimensional multiphoton imaging of brain entry, amyloid binding, and clearance of an amyloid-beta ligand in transgenic mice. Proceedings of the National Academy of Sciences, 100(21), 12462–12467. https://doi.org/10.1073/pnas.2034101100
41. Xu, M. M., Ren, W. M., Tang, X. C., Hu, Y. H., & Zhang, H. Y. (2016). Advances in development of fluorescent probes for detecting amyloid-β aggregates. Acta Pharmacologica Sinica, 37(6), 719–730. https://doi.org/10.1038/aps.2015.155
42. Klunk, W. E., Engler, H., Nordberg, A., Wang, Y., Blomqvist, G., Holt, D. P., Bergström, M., Savitcheva, I., Huang, G. F., Estrada, S., Ausén, B., Debnath, M. L., Barletta, J., Price, J. C., Sandell, J., Lopresti, B. J., Wall, A., Koivisto, P., Antoni, G., Mathis, C. A., & Långström, B. (2004). Imaging brain amyloid in Alzheimer's disease with Pittsburgh Compound-B. Annals of Neurology, 55(3), 306–319. https://doi.org/10.1002/ana.20009
43. Piña, R., Santos-Díaz, A. I., Orta-Salazar, E., Aguilar-Vazquez, A. R., Mantellero, C. A., Acosta-Galeana, I., Estrada-Mondragon, A., Prior-Gonzalez, M., Martinez-Cruz, J. I., & Rosas-Arellano, A. (2022). Ten approaches that improve immunostaining: A review of the latest

advances for the optimization of immunofluorescence. International Journal of Molecular Sciences, 23(3), 1426. https://doi.org/10.3390/ijms23031426
44. Yuan, P., Condello, C., Keene, C. D., Wang, Y., Bird, T. D., Paul, S. M., Luo, W., Colonna, M., Baddeley, D., & Grutzendler, J. (2016). TREM2 haplodeficiency in mice and humans impairs the microglia barrier function leading to decreased amyloid compaction and severe axonal dystrophy. Neuron, 90(4), 724–739. https://doi.org/10.1016/j.neuron.2016.05.003
45. Kumar-Singh, S., Cras, P., Wang, R., Kros, J. M., van Swieten, J., Lübke, U., Ceuterick, C., Serneels, S., Vennekens, K., Timmermans, J. P., Van Marck, E., Martin, J. J., van Duijn, C. M., & Van Broeckhoven, C. (2002). Dense-core senile plaques in the Flemish variant of Alzheimer's disease are vasocentric. American Journal of Pathology, 161(2), 507–520. https://doi.org/10.1016/S0002-9440(10)64207-1
46. Estaun-Panzano, J., Dembitskaya, Y., Calaresu, I., Nandi, S., Gresil, Q., Doudnikoff, E., Leste-Laserre, T., Amedee, T., Cognet, L., Groc, L., Nagerl, V., & Bezard, E. (2025). Decoding Amyloid Plaque Penetrability: Exploring extracellular space and rheology in plaque-rich cortex. bioRxiv 2025.08.24.671960, (Cold Spring Harbor Laboratory). https://doi.org/10.1101/2025.08.24.671960
47. Sehlin, D., Fang, X. T., Cato, L., Antoni, G., Lannfelt, L., & Syvänen, S. (2016). Antibody-based PET imaging of amyloid beta in mouse models of Alzheimer's disease. Nature Communications, 7, 10759. https://doi.org/10.1038/ncomms10759
48. Sehlin, D., Hultqvist, G., Michno, W., Aguilar, X., Dahlén, A. D., Cerilli, E., Bucher, N. M., Lopes van den Broek, S., & Syvänen, S. (2025). Bispecific brain-penetrant antibodies for treatment of Alzheimer's disease. Journal of Prevention of Azheimers Disease, 12(8), 100214. https://doi.org/10.1016/j.tjpad.2025.100214
49. Sumbria, R. K., Hui, E. K., Lu, J. Z., Boado, R. J., & Pardridge, W. M. (2013). Disaggregation of amyloid plaque in brain of Alzheimer's disease transgenic mice with daily subcutaneous administration of a tetravalent bispecific antibody that targets the transferrin receptor and the Abeta amyloid peptide. Molecular Pharmaceutics, 10(9), 3507–3513. https://doi.org/10.1021/mp400348n
50. Bonvicini, G., Syvänen, S., Andersson, K. G., Haaparanta-Solin, M., López-Picón, F., & Sehlin, D. (2022). ImmunoPET imaging of amyloid-beta in a rat model of Alzheimer's disease with a bispecific, brain-penetrating fusion protein. Translational Neurodegeneration, 11(1), 55. https://doi.org/10.1186/s40035-022-00324-y
51. Chapleau, M., Iaccarino, L., Soleimani-Meigooni, D., & Rabinovici, G. D. (2022). The role of amyloid PET in imaging neurodegenerative disorders: A review. Journal of Nuclear Medicine : official publication, Society of Nuclear Medicine, 63(Supplement 1), 13S–19S. https://doi.org/10.2967/jnumed.121.263195
52. Mathis, C. A., Mason, N. S., Lopresti, B. J., & Klunk, W. E. (2012). Development of positron emission tomography β-amyloid plaque imaging agents. Seminars in Nuclear Medicine, 42(6), 423–432. https://doi.org/10.1053/j.semnuclmed.2012.07.001
53. Krutsay, M. Patológiai Technika; Medicina: Budapest, Hungary, 1999; ISBN 963 242 434 4
54. Wilcock, D. M., Gordon, M. N., & Morgan, D. (2006). Quantification of cerebral amyloid angiopathy and parenchymal amyloid plaques with Congo red histochemical stain. Nature Protocols, 1(3), 1591–1595. https://doi.org/10.1038/nprot.2006.277
55. Meilandt, W. J., Ngu, H., Gogineni, A., Lalehzadeh, G., Lee, S. H., Srinivasan, K., Imperio, J., Wu, T., Weber, M., Kruse, A. J., Stark, K. L., Chan, P., Kwong, M., Modrusan, Z., Friedman, B. A., Elstrott, J., Foreman, O., Easton, A., Sheng, M., & Hansen, D. V. (2020). Trem2 deletion reduces late-stage amyloid plaque accumulation, elevates the Aβ42:Aβ40 ratio, and exacerbates axonal dystrophy and dendritic spine loss in the PS2APP Alzheimer's mouse model. Journal of Neuroscience, 40(9), 1956–1974. https://doi.org/10.1523/jneurosci.1871-19.2019

56. Liu, P., Reichl, J. H., Rao, E. R., McNellis, B. M., Huang, E. S., Hemmy, L. S., Forster, C. L., Kuskowski, M. A., Borchelt, D. R., Vassar, R., Ashe, K. H., & Zahs, K. R. (2017). Quantitative comparison of dense-core amyloid plaque accumulation in amyloid-β protein precursor transgenic mice. Journal of Alzheimer's Disease, 56(2), 743–761. https://doi.org/10.3233/JAD-161027
57. Irizarry, B. A., Davis, J., Zhu, X., Boon, B. D. C., Rozemuller, A. J. M., Van Nostrand, W. E., & Smith, S. O. (2021). Human cerebral vascular amyloid contains both antiparallel and parallel in-register Aβ40 fibrils. Journal of Biological Chemistry, 297(5), 101259. https://doi.org/10.1016/j.jbc.2021.101259
58. Rutgers, K. S., van Remoortere, A., van Buchem, M. A., Verrips, C. T., Greenberg, S. M., Bacskai, B. J., Frosch, M. P., van Duinen, S. G., Maat-Schieman, M. L., & van der Maarel, S. M. (2009). Differential recognition of vascular and parenchymal beta amyloid deposition. Neurobiology of Aging, 32(10), 1774–1783. https://doi.org/10.1016/j.neurobiolaging.2009.11.012
59. Silberberg, M., & Grecco, H. E. (2023). Robust and unbiased estimation of the background distribution for automated quantitative imaging. Journal of the Optical Society of America. A, Optics, image science, and vision, 40(4), C8–C15. https://doi.org/10.1364/JOSAA.477468
60. Piccinini, F., Lucarelli, E., Gherardi, A., & Bevilacqua, A. (2012). Multi-image based method to correct vignetting effect in light microscopy images. Journal of Microscopy, 248(1), 6–22. https://doi.org/10.1111/j.1365-2818.2012.03645.x
61. Singh, S., Bray, M. A., Jones, T. R., & Carpenter, A. E. (2014). Pipeline for illumination correction of images for high-throughput microscopy. Journal of Microscopy, 256(3), 231–236. https://doi.org/10.1111/jmi.12178
62. Waters, J. C., & Wittmann, T. (2014). Concepts in quantitative fluorescence microscopy. Methods in cell biology, 123, 1–18. https://doi.org/10.1016/B978-0-12-420138-5.00001-X
63. Likar, B., Maintz, J. B., Viergever, M. A., & Pernus, F. (2000). Retrospective shading correction based on entropy minimization. Journal of Microscopy, 197(Pt 3), 285–295. https://doi.org/10.1046/j.1365-2818.2000.00669.x
64. Leong, F. J., Brady, M., & McGee, J. O. (2003). Correction of uneven illumination (vignetting) in digital microscopy images. Journal of Clinical Pathology, 56(8), 619–621. https://doi.org/10.1136/jcp.56.8.619
65. Lee, S. C., & Bajcsy, P. (2006). Intensity correction of fluorescent confocal laser scanning microscope images by mean-weight filtering. Journal of Microscopy, 221(Pt 2), 122–136. https://doi.org/10.1111/j.1365-2818.2006.01546.x
66. Otsu, N. (1979). A threshold selection method from gray-level histograms. IEEE Transactions on Systems, Man, and Cybernetics, 9(1), 62–66. https://doi.org/10.1109/TSMC.1979.4310076
67. Sternberg, N. (1983). Biomedical image processing. Computer, 16(1), 22–34. https://doi.org/10.1109/MC.1983.1654163
68. LeCun, Y., Bengio, Y., & Hinton, G. (2015). Deep learning. Nature, 521(7553), 436–444. https://doi.org/10.1038/nature14539
69. Russell, S. J., & Norvig, P. (2021). Artificial intelligence: A Modern Approach, Global Edition. Pearson Higher Education. ISBN 9781292401133
70. Goodfellow, I., Bengio, Y., & Courville, A. (Eds.) (2016). Deep learning. In MIT Press eBooks. https://dl.acm.org/citation.cfm?id=3086952
71. Jordan, M. I., & Mitchell, T. M. (2015). Machine learning: Trends, perspectives, and prospects. Science, 349(6245), 255–260. https://doi.org/10.1126/science.aaa8415
72. Xu, Y., Liu, X., Cao, X., Huang, C., Liu, E., Qian, S., Liu, X., Wu, Y., Dong, F., Qiu, C. W., Qiu, J., Hua, K., Su, W., Wu, J., Xu, H., Han, Y., Fu, C., Yin, Z., Liu, M., Roepman, R., Dietmann, S., Virta, M., Kengara, F., Zhang, Z., Zhang, L., Zhao, T., Dai, J., Yang, J., Lan, L., Luo, M., Liu, Z., An, T., Zhang, B., He, X., Cong, S., Liu, X., Zhang, W., Lewis, J. P., Tiedje, J. M., Wang, Q., A, Z., Wang, F., Zhang, L., Huang, T., Lu, C., Cai, Z., Wang, F., & Zhang, J. (2021).

Artificial intelligence: A powerful paradigm for scientific research. The Innovation, 2(4), 100179. https://doi.org/10.1016/j.xinn.2021.100179
73. Tripathi, D., Hajra, K., Mulukutla, A., Shreshtha, R., & Maity, D. (2025). Artificial intelligence in biomedical engineering and its influence on healthcare structure: Current and future prospects. Bioengineering, 12(2), 163. https://doi.org/10.3390/bioengineering12020163
74. Habehh, H., & Gohel, S. (2021). Machine learning in healthcare. Current Genomics, 22(4), 291–300. https://doi.org/10.2174/1389202922666210705124359
75. Ali, O., Abdelbaki, W., Shrestha, A., Elbasi, E., Alryalat, M. a. A., & Dwivedi, Y. K. (2023). A systematic literature review of artificial intelligence in the healthcare sector: Benefits, challenges, methodologies, and functionalities. Journal of Innovation & Knowledge, 8(1), 100333. https://doi.org/10.1016/j.jik.2023.100333
76. Ali, N. A., & Mashwani, N. W. K. (2023). A supervised machine learning algorithms: Applications, challenges, and recommendations. Proceedings of Pakistan Academy of Sciences a Physical and Computational Sciences, 60(4). https://doi.org/10.53560/ppasa(60-4)831
77. Chinecherem, N. O. O., Esther, N. U. N., & Chigbundu, N. K. (2023). Comprehensive review of supervised machine learning algorithms to identify the best and error free. International Journal of Scholarly Research in Engineering and Technology, 2(1), 013–019. https://doi.org/10.56781/ijsret.2023.2.1.0028
78. Barhate, A., Tale, A., Jikar, N., Verma, P., Kumar, P., & Yesankar, P. (2024). A comprehensive review of supervised learning algorithms in healthcare applications. 2nd DMIHER International Conference on Artificial Intelligence in Healthcare, Education and Industry (IDICAIEI), Wardha, India, 1–6. https://doi.org/10.1109/idicaiei61867.2024.10842845
79. Ono, S., & Goto, T. (2022). Introduction to supervised machine learning in clinical epidemiology. Annals of Clinical Epidemiology, 4(3), 63–71. https://doi.org/10.37737/ace.22009
80. Roy, S., Meena, T., & Lim, S.-J. (2022). Demystifying supervised learning in healthcare 4.0: A new reality of transforming diagnostic medicine. Diagnostics, 12(10), 2549. https://doi.org/10.3390/diagnostics12102549
81. Zhang, M. (2022). Unsupervised learning algorithms in big data: An overview. In Advances in Social Science, Education and Humanities Research/Advances in social science, education and humanities research (pp. 910–931). https://doi.org/10.2991/978-2-494069-89-3_107
82. Yazici, İ., Shayea, I., & Din, J. (2023). A survey of applications of artificial intelligence and machine learning in future mobile networks-enabled systems. Engineering Science and Technology an International Journal, 44, 101455. https://doi.org/10.1016/j.jestch.2023.101455
83. Naeem, S., Ali, A., Anam, S., & Ahmed, M. M. (2023). An unsupervised machine learning algorithms: Comprehensive review. International Journal of Computing and Digital Systems, 13(1), 911–921. https://doi.org/10.12785/ijcds/130172
84. Trezza, A., Visibelli, A., Roncaglia, B., Spiga, O., & Santucci, A. (2024). Unsupervised learning in precision medicine: Unlocking personalized healthcare through AI. Applied Sciences, 14(20), 9305. https://doi.org/10.3390/app14209305
85. François-Lavet, V., Henderson, P., Islam, R., Bellemare, M. G., & Pineau, J. (2018). An introduction to deep reinforcement learning. Foundations and Trends® in Machine Learning, 11(3–4), 219–354. https://doi.org/10.1561/2200000071
86. Terven, J. (2025). Deep reinforcement learning: A chronological overview and methods. AI, 6(3), 46. https://doi.org/10.3390/ai6030046
87. Jayaraman, P., Desman, J., Sabounchi, M., Nadkarni, G. N., & Sakhuja, A. (2024). A primer on reinforcement learning in medicine for clinicians. NPJ Digital Medicine, 7(1), 337. https://doi.org/10.1038/s41746-024-01316-0
88. Yang, X., Song, Z., King, I., & Xu, Z. (2022). A survey on deep semi-supervised learning. IEEE Transactions on Knowledge and Data Engineering, 35(9), 8934–8954. https://doi.org/10.1109/tkde.2022.3220219

89. Zhang, X., Wang, J., Wei, J., Yuan, X., & Wu, M. (2025). A review of non-fully supervised deep learning for medical image segmentation. Information, 16(6), 433. https://doi.org/10.3390/info16060433
90. Hospedales, T. M., Antoniou, A., Micaelli, P., & Storkey, A. J. (2021). Meta-learning in neural networks: A survey. IEEE Transactions on Pattern Analysis and Machine Intelligence, 1. https://doi.org/10.1109/tpami.2021.3079209
91. Yakimovich, A., Beaugnon, A., Huang, Y., & Ozkirimli, E. (2021). Labels in a haystack: Approaches beyond supervised learning in biomedical applications. Patterns (New York, N.Y.), 2(12), 100383. https://doi.org/10.1016/j.patter.2021.100383
92. Cheplygina, V., de Bruijne, M., & Pluim, J. P. W. (2019). Not-so-supervised: A survey of semi-supervised, multi-instance, and transfer learning in medical image analysis. Medical Image Analysis, 54, 280–296. https://doi.org/10.1016/j.media.2019.03.009
93. Bengio, Y., Simard, P., & Frasconi, P. (1994). Learning long-term dependencies with gradient descent is difficult. IEEE Transactions on Neural Networks, 5(2), 157–166. https://doi.org/10.1109/72.279181
94. Cybenko, G. (1989). Approximation by superpositions of a sigmoidal function. Mathematics of Control Signals and Systems, 2(4), 303–314. https://doi.org/10.1007/bf02551274
95. Hornik, K., Stinchcombe, M., & White, H. (1989). Multilayer feedforward networks are universal approximators. Neural Networks, 2(5), 359–366. https://doi.org/10.1016/0893-6080(89)90020-8
96. Montufar, G. F., Pascanu, R., Cho, K., & Bengio, Y. (2014). On the number of linear regions of deep neural networks. arXiv (Cornell University). https://doi.org/10.48550/arxiv.1402.1869
97. Szegedy, C., Liu, W., Jia, Y., Sermanet, P., Reed, S., Anguelov, D., Erhan, D., Vanhoucke, V., & Rabinovich, A. (2014). Going deeper with convolutions. arXiv (Cornell University). https://doi.org/10.48550/arxiv.1409.4842
98. McCulloch, W. S., & Pitts, W. (1943). A logical calculus of the ideas immanent in nervous activity. The Bulletin of Mathematical Biophysics, 5(4), 115–133. https://doi.org/10.1007/bf02478259
99. Rosenblatt, F. (1958). The perceptron: A probabilistic model for information storage and organization in the brain. Psychological Review, 65(6), 386–408. https://doi.org/10.1037/h0042519
100. Rumelhart, D. E., Hinton, G. E., & Williams, R. J. (1986). Learning representations by back-propagating errors. Nature, 323(6088), 533–536. https://doi.org/10.1038/323533a0
101. Hassabis, D., Kumaran, D., Summerfield, C., & Botvinick, M. (2017). Neuroscience-inspired artificial intelligence. Neuron, 95(2), 245–258. https://doi.org/10.1016/j.neuron.2017.06.011
102. Yang, Z., & Yang, Z. (2014). Artificial neural networks. In Elsevier eBooks (pp. 1–17). https://doi.org/10.1016/b978-0-444-53632-7.01101-1
103. Baba, A. (2024). Neural networks from biological to artificial and vice versa. Biosystems, 235, 105110. https://doi.org/10.1016/j.biosystems.2023.105110
104. Hasson, U., Nastase, S. A., & Goldstein, A. (2020). Direct fit to nature: An evolutionary perspective on biological and artificial neural networks. Neuron, 105(3), 416–434. https://doi.org/10.1016/j.neuron.2019.12.002
105. Mienye, I. D., & Swart, T. G. (2024). A comprehensive review of deep learning: Architectures, recent advances, and applications. Information, 15(12), 755. https://doi.org/10.3390/info15120755
106. Islam, M., Chen, G., & Jin, S. (2019). An overview of neural network. American Journal of Neural Networks and Applications, 5(1), 7. https://doi.org/10.11648/j.ajnna.20190501.12
107. Bishop, C. M. (2007). Pattern recognition and machine learning. Journal of Electronic Imaging, 16(4), 049901. https://doi.org/10.1117/1.2819119
108. Alzubaidi, L., Zhang, J., Humaidi, A. J., Al-Dujaili, A., Duan, Y., Al-Shamma, O., Santamaría, J., Fadhel, M. A., Al-Amidie, M., & Farhan, L. (2021). Review of deep learning: concepts,

CNN architectures, challenges, applications, future directions. Journal of Big Data, 8(1). https://doi.org/10.1186/s40537-021-00444-8
109. Gallego, V., & Insua, D. R. (2021). Current advances in neural networks. Annual Review of Statistics and Its Application, 9(1), 197–222. https://doi.org/10.1146/annurev-statistics-040220-112019
110. Shahid, N., Rappon, T., & Berta, W. (2019). Applications of artificial neural networks in health care organizational decision-making: A scoping review. PloS one, 14(2), e0212356. https://doi.org/10.1371/journal.pone.0212356
111. Weiss, R., Karimijafarbigloo, S., Roggenbuck, D., & Rödiger, S. (2022). Applications of neural networks in biomedical data analysis. Biomedicines, 10(7), 1469. https://doi.org/10.3390/biomedicines10071469
112. Emmanuel, C., Jonhson, K. & Allison, J. (2025). The evolution of computer vision: From pixels to perception. https://www.researchgate.net/publication/390066290_The_Evolution_of_Computer_Vision_From_Pixels_to_Perception (accessed on November 3, 2025)
113. Shelke, N. S. M., Pathak, N. I. S., Sangai, N. a. P., Lunge, N. D. V., Shahale, N. K. A., & Vyawahare, N. H. R. (2023). A review paper on computer vision. International Journal of Advanced Research in Science Communication and Technology, 673–677. https://doi.org/10.48175/ijarsct-8901
114. Laad, M., Maurya, R., & Saiyed, N. (2024). Unveiling the vision: A comprehensive review of computer vision in AI and ML. IEEE Conference Publication | IEEE Xplore. https://ieeexplore.ieee.org/document/10533631
115. Shan, D., Qu, F., Wang, Z., Ji, Y., & Xu, J. (2025). A review of the application of computer vision techniques in sustainable engineering of open pit mines. Sustainability, 17(7), 3051. https://doi.org/10.3390/su17073051
116. Salau, A. O., & Jain, S. (2019). Feature extraction: A survey of the types, techniques, applications. International Conference on Signal Processing and Communication (ICSC), NOIDA, India, 158–164. https://doi.org/10.1109/icsc45622.2019.8938371
117. Kumar, G., & Bhatia, P. K. (2014). A detailed review of feature extraction in image processing systems. Fourth International Conference on Advanced Computing & Communication Technologies, Rohtak, India, 5–12. https://doi.org/10.1109/acct.2014.74
118. Jing, J., Liu, S., Wang, G., Zhang, W., & Sun, C. (2022). Recent advances on image edge detection: A comprehensive review. Neurocomputing, 503, 259–271. https://doi.org/10.1016/j.neucom.2022.06.083
119. Xu, Y., Quan, R., Xu, W., Huang, Y., Chen, X., & Liu, F. (2024). Advances in medical image segmentation: A comprehensive review of traditional, deep learning and hybrid approaches. Bioengineering, 11(10), 1034. https://doi.org/10.3390/bioengineering11101034
120. Katiyar, S. K., & Arun, P. V. (2014). Comparative analysis of common edge detection techniques in context of object extraction. arXiv (Cornell University). https://doi.org/10.48550/arxiv.1405.6132
121. Desai, B., Paliwal, M., & Nagwanshi, K. K. (2022). Study on image filtering -- Techniques, algorithm and applications. arXiv (Cornell University). https://doi.org/10.48550/arxiv.2207.06481
122. Chandel, R.C., & Gupta, G. (2013). Image filtering algorithms and techniques: A review. International Journal of Advanced Research in Computer Science and Software Engineering, vol. 3, no. 10, 2013. https://api.semanticscholar.org/CorpusID:212459099
123. Armi, L., & Fekri-Ershad, S. (2019). Texture image analysis and texture classification methods - A review. arXiv (Cornell University). https://doi.org/10.48550/arxiv.1904.06554
124. Rai, M., & Rivas, P. (2020). A review of convolutional neural networks and Gabor filters in object recognition. 2021 International Conference on Computational Science and Computational Intelligence (CSCI), 1560–1567. https://doi.org/10.1109/csci51800.2020.00289

125. Lowe, D. (1999). Object recognition from local scale-invariant features. Proceedings of the Seventh IEEE International Conference on Computer Vision, Kerkyra, Greece, 1150–1157 vol.2. https://doi.org/10.1109/iccv.1999.790410
126. Kortli, Y., Jridi, M., Falou, A. A., & Atri, M. (2018). A comparative study of CFs, LBP, HOG, SIFT, SURF, and BRIEF for security and face recognition. In IOP Publishing eBooks (pp. 13–22). https://doi.org/10.1088/978-0-7503-1457-2ch13
127. Tsalera, E., Papadakis, A., Samarakou, M., & Voyiatzis, I. (2022). Feature extraction with handcrafted methods and convolutional neural networks for facial emotion recognition. Applied Sciences, 12(17), 8455. https://doi.org/10.3390/app12178455
128. Nanni, L., Ghidoni, S., & Brahnam, S. (2017). Handcrafted vs. non-handcrafted features for computer vision classification. Pattern Recognition, 71, 158–172. https://doi.org/10.1016/j.patcog.2017.05.025
129. Jiang, X. (2009). Feature extraction for image recognition and computer vision. 2nd IEEE International Conference on Computer Science and Information Technology, Beijing, China, 1–15. https://doi.org/10.1109/iccsit.2009.5235014
130. Sivic, N., & Zisserman, N. (2003). Video Google: a text retrieval approach to object matching in videos. Proceedings Ninth IEEE International Conference on Computer Vision, Nice, France, 1470–1477 vol.2. https://doi.org/10.1109/iccv.2003.1238663
131. Koniusz, P., Yan, F., Gosselin, P., & Mikolajczyk, K. (2016). Higher-order occurrence pooling for Bags-of-Words: Visual concept detection. IEEE Transactions on Pattern Analysis and Machine Intelligence, 39(2), 313–326. https://doi.org/10.1109/tpami.2016.2545667
132. Gidaris, S., Bursuc, A., Komodakis, N., Pérez, P., & Cord, M. (2020). Learning representations by predicting bags of visual words. arXiv (Cornell University). https://doi.org/10.48550/arxiv.2002.12247
133. Voulodimos, A., Doulamis, N., Doulamis, A., & Protopapadakis, E. (2018). Deep learning for computer vision: A brief review. Computational Intelligence and Neuroscience, 2018, 7068349. https://doi.org/10.1155/2018/7068349
134. Chai, J., Zeng, H., Li, A., & Ngai, E. W. (2021). Deep learning in computer vision: A critical review of emerging techniques and application scenarios. Machine Learning With Applications, 6, 100134. https://doi.org/10.1016/j.mlwa.2021.100134
135. Zhao, X., Wang, L., Zhang, Y., Han, X., Deveci, M., & Parmar, M. (2024). A review of convolutional neural networks in computer vision. Artificial Intelligence Review, 57, 99. https://api.semanticscholar.org/CorpusID:268673911
136. Chen, L., Li, S., Bai, Q., Yang, J., Jiang, S., & Miao, Y. (2021). Review of image classification algorithms based on convolutional neural networks. Remote Sensing, 13(22), 4712. https://doi.org/10.3390/rs13224712
137. Hubel, D. H., & Wiesel, T. N. (1959). Receptive fields of single neurones in the cat's striate cortex. The Journal of Physiology, 148(3), 574–591. https://doi.org/10.1113/jphysiol.1959.sp006308
138. Fukushima, K. (2007). Neocognitron. Scholarpedia, 2(1), 1717. https://doi.org/10.4249/scholarpedia.1717
139. LeCun, Y., Jackel, L.D., Bottou, L., Cortes, C., Denker, J.S., Drucker, H., Guyon, I.M., Muller, U., Sackinger, E., Simard, P.Y., & Vapnik, V.N. (1995). Learning algorithms for classification: A comparison on handwritten digit recognition. https://api.semanticscholar.org/CorpusID:13411815
140. Krizhevsky, A., Sutskever, I., & Hinton, G. E. (2012). ImageNet classification with deep convolutional neural networks. Neural Information Processing Systems, 25, 1097–1105. http://books.nips.cc/papers/files/nips25/NIPS2012_0534.pdf

141. Simonyan, K., & Zisserman, A. (2014). Very deep convolutional networks for large-scale image recognition. Computer Vision and Pattern Recognition. http://export.arxiv.org/pdf/1409.1556
142. He, K., Zhang, X., Ren, S., & Sun, J. (2015). Deep residual learning for image recognition. IEEE Conference on Computer Vision and Pattern Recognition (CVPR), 770-778. https://api.semanticscholar.org/CorpusID:206594692
143. Ronneberger, O., Fischer, P., & Brox, T. (2015). U-NET: Convolutional networks for biomedical image segmentation. arXiv (Cornell University). https://doi.org/10.48550/arxiv.1505.04597
144. Vaswani, A., Shazeer, N., Parmar, N., Uszkoreit, J., Jones, L., Gomez, A. N., Kaiser, L., & Polosukhin, I. (2017). Attention is all you need. arXiv (Cornell University), 30, 5998–6008. https://arxiv.org/pdf/1706.03762v5
145. Khurana, D., Koli, A., Khatter, K., & Singh, S. (2022). Natural language processing: state of the art, current trends and challenges. Multimedia Tools and Applications, 82(3), 3713–3744. https://doi.org/10.1007/s11042-022-13428-4
146. De Santana Correia, A., & Colombini, E. L. (2021). Attention, please! A survey of neural attention models in deep learning. arXiv (Cornell University). https://doi.org/10.48550/arxiv.2103.16775
147. Dosovitskiy, A., Beyer, L., Kolesnikov, A., Weissenborn, D., Zhai, X., Unterthiner, T., Dehghani, M., Minderer, M., Heigold, G., Gelly, S., Uszkoreit, J., & Houlsby, N. (2020). An image is worth 16x16 words: Transformers for image recognition at scale. arXiv (Cornell University). https://doi.org/10.48550/arxiv.2010.11929
148. Khan, A., Rauf, Z., Sohail, A., Khan, A. R., Asif, H., Asif, A., & Farooq, U. (2023). A survey of the vision transformers and their CNN-transformer based variants. Artificial intelligence Review, 56(S3), 2917–2970. https://doi.org/10.1007/s10462-023-10595-0
149. Liu, Z., Lin, Y., Cao, Y., Hu, H., Wei, Y., Zhang, Z., Lin, S., & Guo, B. (2021). Swin Transformer: Hierarchical vision transformer using shifted windows. 2021 IEEE/CVF International Conference on Computer Vision (ICCV), 9992–10002. https://doi.org/10.1109/iccv48922.2021.00986
150. Woo, S., Park, J., Lee, J., & Kweon, I. S. (2018). CBAM: Convolutional block attention module. In Lecture notes in computer science (pp. 3–19). https://doi.org/10.1007/978-3-030-01234-2_1
151. Hu, J., Shen, L., Albanie, S., Sun, G., & Wu, E. (2019). Squeeze-and-Excitation networks. IEEE Transactions on Pattern Analysis and Machine Intelligence, 42(8), 2011–2023. https://doi.org/10.1109/tpami.2019.2913372
152. Oktay, O., Schlemper, J., Folgoc, L. L., Lee, M. C. H., Heinrich, M. P., Misawa, K., Mori, K., McDonagh, S. G., Hammerla, N. Y., Kainz, B., Glocker, B., & Rueckert, D. (2018). Attention U-Net: Learning where to look for the pancreas. arXiv (Cornell University). https://doi.org/10.48550/arxiv.1804.03999
153. Yang, R., & Yu, Y. (2021). Artificial convolutional neural network in object detection and semantic segmentation for medical imaging analysis. Frontiers in Oncology, 11, 638182. https://doi.org/10.3389/fonc.2021.638182
154. Gao, Y., Jiang, Y., Peng, Y., Yuan, F., Zhang, X., & Wang, J. (2025). Medical image segmentation: A comprehensive review of deep learning-based methods. Tomography, 11(5), 52. https://doi.org/10.3390/tomography11050052
155. Zhong, Y., Zhou, W., & Wang, Z. (2025). A survey of data augmentation in domain generalization. Neural Processing Letters, 57(2). https://doi.org/10.1007/s11063-025-11747-9
156. Wang, Z., Wang, P., Liu, K., Wang, P., Fu, Y., Lu, C., Aggarwal, C. C., Pei, J., & Zhou, Y. (2024). A comprehensive survey on data augmentation. arXiv.org. https://arxiv.org/abs/2405.09591

157. Kumar, T., Brennan, R., Mileo, A., & Bendechache, M. (2024). Image data augmentation approaches: A comprehensive survey and future directions. IEEE Access, 1. https://doi.org/10.1109/access.2024.3470122
158. Ma, J., Hu, C., Zhou, P., Jin, F., Wang, X., & Huang, H. (2023). Review of image augmentation used in deep learning-based material microscopic image segmentation. Applied Sciences, 13(11), 6478. https://doi.org/10.3390/app13116478
159. Shen, W., Peng, Z., Wang, X., Wang, H., Cen, J., Jiang, D., Xie, L., Yang, X., & Tian, Q. (2023). A survey on label-efficient deep image segmentation: Bridging the gap between weak supervision and dense prediction. IEEE transactions on pattern analysis and machine intelligence, 45(8), 9284–9305. https://doi.org/10.1109/TPAMI.2023.3246102
160. Zhang, R., Li, G., Wunderlich, T., & Wang, L. (2021). A survey on deep learning-based precise boundary recovery of semantic segmentation for images and point clouds. International Journal of Applied Earth Observation and Geoinformation, 102, 102411. https://doi.org/10.1016/j.jag.2021.102411
161. Lewy, D., & Mańdziuk, J. (2022). An overview of mixing augmentation methods and augmentation strategies. Artificial Intelligence Review, 56(3), 2111–2169. https://doi.org/10.1007/s10462-022-10227-z
162. Zhang, H., Cisse, M., Dauphin, Y. N., & Lopez-Paz, D. (2017). Mixup: Beyond empirical risk minimization. arXiv (Cornell University). https://arxiv.org/pdf/1710.09412
163. Verma, V., Lamb, A., Beckham, C., Najafi, A., Courville, A., Mitliagkas, I., & Bengio, Y. (2018). Manifold Mixup: Learning better representations by interpolating hidden states. Proceedings of the 36th International Conference on Machine Learning, PMLR 97:6438-6447. https://openreview.net/pdf?id=rJlRKjActQ
164. Yun, S., Han, D., Chun, S., Oh, S. J., Yoo, Y., & Choe, J. (2019). CutMix: Regularization strategy to train strong classifiers with localizable features. IEEE/CVF International Conference on Computer Vision (ICCV), 6022–6031. https://doi.org/10.1109/iccv.2019.00612
165. Chen, Y., Yan, Z., & Zhu, Y. (2024). A comprehensive survey for generative data augmentation. Neurocomputing, 600, 128167. https://doi.org/10.1016/j.neucom.2024.128167
166. Islam, T., Hafiz, M. S., Jim, J. R., Kabir, M. M., & Mridha, M. (2024). A systematic review of deep learning data augmentation in medical imaging: Recent advances and future research directions. Healthcare Analytics, 5, 100340. https://doi.org/10.1016/j.health.2024.100340
167. Garcea, F., Serra, A., Lamberti, F., & Morra, L. (2022). Data augmentation for medical imaging: A systematic literature review. Computers in Biology and Medicine, 152, 106391. https://doi.org/10.1016/j.compbiomed.2022.106391
168. Goceri, E. (2023). Medical image data augmentation: techniques, comparisons and interpretations. Artificial Intelligence Review, 56(11), 12561–12605. https://doi.org/10.1007/s10462-023-10453-z
169. Zhou, B., Khosla, A., Lapedriza, A., Oliva, A., & Torralba, A. (2016). Learning deep features for discriminative localization. IEEE Conference on Computer Vision and Pattern Recognition (CVPR), Las Vegas, NV, USA, 2016, Pp. 2921-2929. https://doi.org/10.1109/cvpr.2016.319
170. Kwak, S., Hong, S., & Han, B. (2017). Weakly supervised semantic segmentation using superpixel pooling network. Proceedings of the AAAI Conference on Artificial Intelligence, 31(1). https://doi.org/10.1609/aaai.v31i1.11213
171. Liu, Y., Lian, L., Zhang, E., Xu, L., Xiao, C., Zhong, X., Li, F., Jiang, B., Dong, Y., Ma, L., Huang, Q., Xu, M., Zhang, Y., Yu, D., Yan, C., & Qin, P. (2022). Mixed-UNet: Refined class activation mapping for weakly-supervised semantic segmentation with multi-scale inference. Frontiers in Computer Science, 4. https://doi.org/10.3389/fcomp.2022.1036934
172. Zheng, S., Jayasumana, S., Romera-Paredes, B., Vineet, V., Su, Z., Du, D., Huang, C., & Torr, P. H. S. (2015). Conditional random fields as recurrent neural networks. IEEE International

Conference on Computer Vision (ICCV), Santiago, Chile, 2015, pp. 1529-1537. https://doi.org/10.1109/iccv.2015.179
173. Fu, J., Lu, T., Zhang, S., & Wang, G. (2023). UM-CAM: Uncertainty-weighted multi-resolution class activation maps for weakly-supervised fetal brain segmentation. In Greenspan H. et al., Medical Image Computing and Computer Assisted Intervention – MICCAI 2023. Lecture notes in computer science, Vol. 14226 (pp. 315–324). https://doi.org/10.1007/978-3-031-43990-2_30
174. Bressan, P. O., Marcato, J., Junior, Martins, J. a. C., De Melo, M. J., Gonçalves, D. N., Freitas, D. M., Ramos, A. P. M., Furuya, M. T. G., Osco, L. P., De Andrade Silva, J., Luo, Z., Garcia, R. C., Ma, L., Li, J., & Gonçalves, W. N. (2022). Semantic segmentation with labeling uncertainty and class imbalance applied to vegetation mapping. International Journal of Applied Earth Observation and Geoinformation, 108, 102690. https://doi.org/10.1016/j.jag.2022.102690
175. Kervadec, H., Bouchtiba, J., Desrosiers, C., Granger, E., Dolz, J., & Ben Ayed, I. (2021). Boundary loss for highly unbalanced segmentation. Medical Image Analysis, 67, 101851. https://doi.org/10.1016/j.media.2020.101851
176. Guo, R., Sun, X., Chen, K., Zhou, X., Yan, Z., Diao, W., & Yan, M. (2020). JMLNET: Joint multi-label learning network for weakly supervised semantic segmentation in aerial images. Remote Sensing, 12(19), 3169. https://doi.org/10.3390/rs12193169
177. Islam, M., & Glocker, B. (2021). Spatially varying label smoothing: Capturing uncertainty from expert annotations. In Lecture notes in computer science (pp. 677–688). https://doi.org/10.1007/978-3-030-78191-0_52
178. Kats, E., Goldberger, J., & Greenspan, H. (2019). Soft labeling by distilling anatomical knowledge for improved MS lesion segmentation. IEEE 19th International Symposium on Biomedical Imaging (ISBI). https://doi.org/10.1109/isbi.2019.8759518
179. Vasudeva, S. A., Dolz, J., & Lombaert, H. (2025). GeoLS: An intensity-based, geodesic soft labeling for image segmentation. The Journal of Machine Learning for Biomedical Imaging, 2(April 2025), 120–134. https://doi.org/10.59275/j.melba.2025-c1d9
180. Dang, T., Nguyen, H. H., & Tiulpin, A. (2024). SINGR: Brain tumor segmentation via signed normalized geodesic transform regression. In Lecture notes in computer science (pp. 593–603). https://doi.org/10.1007/978-3-031-72114-4_57
181. Han, C., Lin, J., Mai, J., Wang, Y., Zhang, Q., Zhao, B., Chen, X., Pan, X., Shi, Z., Xu, Z., Yao, S., Yan, L., Lin, H., Huang, X., Liang, C., Han, G., & Liu, Z. (2022). Multi-layer pseudo-supervision for histopathology tissue semantic segmentation using patch-level classification labels. Medical Image Analysis, 80, 102487. https://doi.org/10.1016/j.media.2022.102487
182. Din, N. U., & Yu, J. (2021). Training a deep learning model for single-cell segmentation without manual annotation. Scientific Reports, 11(1). https://doi.org/10.1038/s41598-021-03299-4
183. Nishimura, K., Ker, D. F. E., & Bise, R. (2019). Weakly supervised cell instance segmentation by propagating from detection response. In Lecture notes in computer science (pp. 649–657). https://doi.org/10.1007/978-3-030-32239-7_72
184. Ramananda, S. H., & Sundaresan, V. (2023). Class activation map-based weakly supervised hemorrhage segmentation using Resnet-LSTM in non-contrast computed tomography images. arXiv (Cornell University). https://doi.org/10.48550/arxiv.2309.16627
185. Li, Z., & Xia, Y. (2020). Deep reinforcement learning for weakly-supervised lymph node segmentation in CT images. IEEE Journal of Biomedical and Health Informatics, 25(3), 774–783. https://doi.org/10.1109/jbhi.2020.3008759
186. Sampaio, V., & Cordeiro, F. R. (2023). Improving mass detection in mammography images: A study of weakly supervised learning and class activation map methods. 36th SIBGRAPI Conference on Graphics, Patterns and Images, Pp. 139-144, 139–144. https://doi.org/10.1109/sibgrapi59091.2023.10347182

187. Li, Y., Yu, Y., Zou, Y., Xiang, T., & Li, X. (2022). Online easy example mining for weakly-supervised gland segmentation from histology images. In Lecture notes in computer science (pp. 578–587). https://doi.org/10.1007/978-3-031-16440-8_55
188. Sukesh, A. V., Dolz, J., & Lombaert, H. (2020). Manifold-driven attention maps for weakly supervised segmentation. arXiv (Cornell University). https://doi.org/10.48550/arxiv.2004.03046
189. Kim, J., Kim, H. J., Kim, C., Lee, J. H., Kim, K. W., Park, Y. M., Kim, H. W., Ki, S. Y., Kim, Y. M., & Kim, W. H. (2021). Weakly-supervised deep learning for ultrasound diagnosis of breast cancer. Scientific Reports, 11(1). https://doi.org/10.1038/s41598-021-03806-7
190. Kushwaha, A., Gupta, S., Bhanushali, A., & Dastidar, T. R. (2020). Rapid training data creation by synthesizing medical images for classification and localization. IEEE/CVF Conference on Computer Vision and Pattern Recognition Workshops (CVPRW), 4272–4279. https://doi.org/10.1109/cvprw50498.2020.00504
191. Zhang, A., Shailja, S., Borba, C., Miao, Y., Goebel, M., Ruschel, R., Ryan, K., Smith, W., & Manjunath, B. S. (2022). Automatic classification and neurotransmitter prediction of synapses in electron microscopy. Biological Imaging, 2. https://doi.org/10.1017/s2633903x2200006x
192. Liu, D., Zhang, D., Song, Y., Zhang, F., O'Donnell, L., Huang, H., Chen, M., & Cai, W. (2020). Unsupervised instance segmentation in microscopy images via panoptic domain adaptation and task re-weighting. 2022 IEEE/CVF Conference on Computer Vision and Pattern Recognition (CVPR). https://doi.org/10.1109/cvpr42600.2020.00430
193. Curti, N., Merli, Y., Zengarini, C., Giampieri, E., Merlotti, A., Dall'Olio, D., Marcelli, E., Bianchi, T., & Castellani, G. (2022). Effectiveness of semi-supervised active learning in automated wound image segmentation. International Journal of Molecular Sciences, 24(1), 706. https://doi.org/10.3390/ijms24010706
194. Arvaniti, E., Fricker, K. S., Moret, M., Rupp, N., Hermanns, T., Fankhauser, C., Wey, N., Wild, P. J., Rüschoff, J. H., & Claassen, M. (2018). Automated Gleason grading of prostate cancer tissue microarrays via deep learning. Scientific Reports, 8(1). https://doi.org/10.1038/s41598-018-30535-1
195. Liu, H., Wang, L., Nan, Y., Jin, F., Wang, Q., & Pu, J. (2019). SDFN: Segmentation-based deep fusion network for thoracic disease classification in chest X-ray images. Computerized Medical Imaging and Graphics, 75, 66–73. https://doi.org/10.1016/j.compmedimag.2019.05.005
196. Meng, M., Zhang, M., Shen, D., & He, G. (2022). Differentiation of breast lesions on dynamic contrast-enhanced magnetic resonance imaging (DCE-MRI) using deep transfer learning based on DenseNet201. Medicine, 101(45), e31214. https://doi.org/10.1097/md.0000000000031214
197. Sulaiman, A., Anand, V., Gupta, S., Rajab, A., Alshahrani, H., Reshan, M. S. A., Shaikh, A., & Hamdi, M. (2024). Attention based UNet model for breast cancer segmentation using BUSI dataset. Scientific Reports, 14(1). https://doi.org/10.1038/s41598-024-72712-5
198. Dornadula, B., Geetha, S., Anbarasi, L. J., & Kadry, S. (2022). A survey of COVID-19 detection from chest X-Rays using deep learning methods. International Journal of Data Warehousing and Mining, 18(1), 1–16. https://doi.org/10.4018/ijdwm.314155
199. Ullah, I., Ali, F., Shah, B., El-Sappagh, S., Abuhmed, T., & Park, S. H. (2023). A deep learning based dual encoder–decoder framework for anatomical structure segmentation in chest X-ray images. Scientific Reports, 13(1). https://doi.org/10.1038/s41598-023-27815-w
200. Wei, J. W., Wei, J. W., Jackson, C. R., Ren, B., Suriawinata, A. A., & Hassanpour, S. (2019). Automated detection of celiac disease on duodenal biopsy slides: A deep learning approach. Journal of Pathology Informatics, 10(1), 7. https://doi.org/10.4103/jpi.jpi_87_18
201. Phuong, H. N. T., Shin, C., & Jeong, H. (2021). Finding the differences in capillaries of taste buds between smokers and non-smokers using the convolutional neural networks. Applied Sciences, 11(8), 3460. https://doi.org/10.3390/app11083460

202. Richmond, D., Jost, A. P., Lambert, T., Waters, J., & Elliott, H. (2017). DeadNet: Identifying phototoxicity from label-free microscopy images of cells using deep convnets. arXiv (Cornell University). https://doi.org/10.48550/arxiv.1701.06109
203. Irmak, E. (2021). A novel implementation of deep-learning approach on malaria parasite detection from thin blood cell images. Istanbul University - Journal of Electrical & Electronics Engineering, 21(2), 216–224. https://doi.org/10.5152/electrica.2020.21004
204. Chen, Z., Zheng, W., Pang, K., Xia, D., Guo, L., Chen, X., Wu, F., & Wang, H. (2023). Weakly supervised learning analysis of Aβ plaque distribution in the whole rat brain. Frontiers in Neuroscience, 16. https://doi.org/10.3389/fnins.2022.1097019
205. Tang, Z., Chuang, K. V., DeCarli, C., Jin, L., Beckett, L., Keiser, M. J., & Dugger, B. N. (2019). Interpretable classification of Alzheimer's disease pathologies with a convolutional neural network pipeline. Nature Communications, 10(1). https://doi.org/10.1038/s41467-019-10212-1
206. Müller, D., Röhr, D., Boon, B. D. C., Wulf, M., Arto, T., Hoozemans, J. J. M., Marcus, K., Rozemuller, A. J. M., Großerueschkamp, F., Mosig, A., & Gerwert, K. (2025). Label-free Aβ plaque detection in Alzheimer's disease brain tissue using infrared microscopy and neural networks. Heliyon, 11(4), e42111. https://doi.org/10.1016/j.heliyon.2025.e42111
207. Chabrun, F., Dieu, X., Doudeau, N., Gautier, J., Luque-Paz, D., Geneviève, F., Ferré, M., Mirebeau-Prunier, D., Annweiler, C., & Reynier, P. (2021). Deep learning shows no morphological abnormalities in neutrophils in Alzheimer's disease. Alzheimer S & Dementia Diagnosis Assessment & Disease Monitoring, 13(1). https://doi.org/10.1002/dad2.12146
208. Kettenmann, H., Hanisch, U., Noda, M., & Verkhratsky, A. (2011). Physiology of microglia. Physiological Reviews, 91(2), 461–553. https://doi.org/10.1152/physrev.00011.2010
209. Prinz, M., & Priller, J. (2014). Microglia and brain macrophages in the molecular age: from origin to neuropsychiatric disease. Nature Reviews. Neuroscience, 15(5), 300–312. https://doi.org/10.1038/nrn3722
210. Saijo, K., & Glass, C. K. (2011). Microglial cell origin and phenotypes in health and disease. Nature Reviews. Immunology, 11(11), 775–787. https://doi.org/10.1038/nri3086
211. Raivich, G., Bohatschek, M., Kloss, C. U., Werner, A., Jones, L. L., & Kreutzberg, G. W. (1999). Neuroglial activation repertoire in the injured brain: graded response, molecular mechanisms and cues to physiological function. Brain Research Reviews, 30(1), 77–105. https://doi.org/10.1016/s0165-0173(99)00007-7
212. Ayoub, A. E., & Salm, A. K. (2003). Increased morphological diversity of microglia in the activated hypothalamic supraoptic nucleus. Journal of Neuroscience, *23*(21), 7759–7766. https://doi.org/10.1523/jneurosci.23-21-07759.2003
213. Shahidehpour, R. K., Higdon, R. E., Crawford, N. G., Neltner, J. H., Ighodaro, E. T., Patel, E., Price, D., Nelson, P. T., & Bachstetter, A. D. (2021). Dystrophic microglia are associated with neurodegenerative disease and not healthy aging in the human brain. Neurobiology of Aging, *99*, 19–27. https://doi.org/10.1016/j.neurobiolaging.2020.12.003
214. Szabo, M., Dulka, K., & Gulya, K. (2015). Calmodulin inhibition regulates morphological and functional changes related to the actin cytoskeleton in pure microglial cells. Brain Research Bulletin, *120*, 41–57. https://doi.org/10.1016/j.brainresbull.2015.11.003
215. Molnár, K., Lőrinczi, B., Fazakas, C., Szatmári, I., Fülöp, F., Kmetykó, N., Berkecz, R., Ilisz, I., Krizbai, I. A., Wilhelm, I., & Vécsei, L. (2021). SZR-104, a novel kynurenic acid analogue with high permeability through the blood–brain barrier. Pharmaceutics, 13(1), 61. https://doi.org/10.3390/pharmaceutics13010061
216. Lajkó, N., Kata, D., Szabó, M., Mátyás, A., Dulka, K., Földesi, I., Fülöp, F., Gulya, K., Vécsei, L., & Mihály, A. (2020). Sensitivity of rodent microglia to kynurenines in models of epilepsy and inflammation in vivo and in vitro: microglia activation is inhibited by kynurenic acid and

the synthetic analogue SZR104. International Journal of Molecular Sciences, 21(23), 9333. https://doi.org/10.3390/ijms21239333
217. Szabo, M., Lajkó, N., Dulka, K., Szatmári, I., Fülöp, F., Mihály, A., Vécsei, L., & Gulya, K. (2022). Kynurenic acid and its analog SZR104 exhibit strong antiinflammatory effects and alter the intracellular distribution and methylation patterns of H3 histones in immunochallenged Microglia-Enriched cultures of newborn rat brains. International Journal of Molecular Sciences, 23(3), 1079. https://doi.org/10.3390/ijms23031079
218. Fujita, H., Tanaka, J., Toku, K., Tateishi, N., Suzuki, Y., Matsuda, S., Sakanaka, M., & Maeda, N. (1996). Effects of GM-CSF and ordinary supplements on the ramification of microglia in culture: A morphometrical study. Glia, 18(4), 269–281. https://doi.org/10.1002/(sici)1098-1136(199612)18:4
219. Del Mar Fernández-Arjona, M., Grondona, J. M., Fernández-Llebrez, P., & López-Ávalos, M. D. (2019). Microglial morphometric parameters correlate with the expression level of IL-1B, and allow identifying different activated morphotypes. Frontiers in Cellular Neuroscience, 13. https://doi.org/10.3389/fncel.2019.00472
220. Katsuragi, Y., Ichimura, Y., & Komatsu, M. (2015). p62/SQSTM1 functions as a signaling hub and an autophagy adaptor. FEBS Journal, 282(24), 4672–4678. https://doi.org/10.1111/febs.13540
221. Komatsu, M., Kageyama, S., & Ichimura, Y. (2012). p62/SQSTM1/A170: Physiology and pathology. Pharmacological Research, 66(6), 457–462. https://doi.org/10.1016/j.phrs.2012.07.004
222. Harry, G. J., & Kraft, A. D. (2008). Neuroinflammation and microglia: considerations and approaches for neurotoxicity assessment. Expert Opinion on Drug Metabolism & Toxicology, 4(10), 1265–1277. https://doi.org/10.1517/17425255.4.10.1265
223. Jin, M., Wang, F., Qi, D., Liu, W., Gu, C., Mao, C., Yang, Y., Zhao, Z., Hu, L., & Liu, C. (2018). A critical role of autophagy in regulating microglia polarization in neurodegeneration. Frontiers in Aging Neuroscience, 10. https://doi.org/10.3389/fnagi.2018.00378
224. Ye, X., Zhu, M., Che, X., Wang, H., Liang, X., Wu, C., Xue, X., & Yang, J. (2020). Lipopolysaccharide induces neuroinflammation in microglia by activating the MTOR pathway and downregulating Vps34 to inhibit autophagosome formation. Journal of Neuroinflammation, 17(1). https://doi.org/10.1186/s12974-019-1644-8
225. Klionsky, D. J., Abdelmohsen, K., Abe, A., Abedin, M. J., Abeliovich, H., Arozena, A. A., Adachi, H., Adams, C. M., Adams, P. D., Adeli, K., Adhihetty, P. J., Adler, S. G., Agam, G., Agarwal, R., Aghi, M. K., Agnello, M., Agostinis, P., Aguilar, P. V., Aguirre-Ghiso, J., . . . Zughaier, S. M. (2016). Guidelines for the use and interpretation of assays for monitoring autophagy (3rd edition). Autophagy, 12(1), 1–222. https://doi.org/10.1080/15548627.2015.1100356
226. Bjørkøy, G., Lamark, T., Brech, A., Outzen, H., Perander, M., Øvervatn, A., Stenmark, H., & Johansen, T. (2005). p62/SQSTM1 forms protein aggregates degraded by autophagy and has a protective effect on huntingtin-induced cell death. The Journal of Cell Biology, 171(4), 603–614. https://doi.org/10.1083/jcb.200507002
227. Bjørkøy, G., Lamark, T., Pankiv, S., Øvervatn, A., Brech, A., & Johansen, T. (2009). Chapter 12 Monitoring autophagic degradation of p62/SQSTM1. Methods in Enzymology on CD-ROM/Methods in Enzymology, 181–197. https://doi.org/10.1016/s0076-6879(08)03612-4
228. Komatsu, M., Waguri, S., Koike, M., Sou, Y., Ueno, T., Hara, T., Mizushima, N., Iwata, J., Ezaki, J., Murata, S., Hamazaki, J., Nishito, Y., Iemura, S., Natsume, T., Yanagawa, T., Uwayama, J., Warabi, E., Yoshida, H., Ishii, T., Kobayashi, A., Yamamoto, M., Yue, Z., Uchiyama, Y., Kominami, E., & Tanaka, K. (2007). Homeostatic levels of p62 control cytoplasmic inclusion body formation in autophagy-deficient mice. *Cell*, *131*(6), 1149–1163. https://doi.org/10.1016/j.cell.2007.10.035

229. Chae, U., Kim, H. S., Lee, H., Lee, S., & Lee, D. (2018). Drp1-dependent mitochondrial fission regulates p62-mediated autophagy in LPS-induced activated microglial cells. *Bioscience Biotechnology and Biochemistry*, *83*(3), 409–416. https://doi.org/10.1080/09168451.2018.1549933
230. Kim, S., Oh, S., Seol, S., Davaanyam, D., & Lee, J. (2022). Cytosolic HMGB1 mediates LPS-induced autophagy in microglia by interacting with NOD2 and suppresses its proinflammatory function. *Cells*, *11*(15), 2410. https://doi.org/10.3390/cells11152410
231. Taylor, F., Huffman, M. D., Macedo, A. F., Moore, T. H., Burke, M., Smith, G. D., Ward, K., Ebrahim, S., & Gay, H. C. (2013). Statins for the primary prevention of cardiovascular disease. Cochrane Library, 2021(9). https://doi.org/10.1002/14651858.cd004816.pub5
232. Kata, D., Földesi, I., Feher, L., Hackler, L., Puskas, L., & Gulya, K. (2015). Rosuvastatin enhances anti-inflammatory and inhibits pro-inflammatory functions in cultured microglial cells. Neuroscience, 314, 47–63. https://doi.org/10.1016/j.neuroscience.2015.11.053
233. Kata, D., Földesi, I., Feher, L. Z., Hackler, L., Puskas, L. G., & Gulya, K. (2017). A novel pleiotropic effect of aspirin: Beneficial regulation of pro- and anti-inflammatory mechanisms in microglial cells. *Brain Research Bulletin*, *132*, 61–74. https://doi.org/10.1016/j.brainresbull.2017.05.009
234. Qian, L., Zhu, K., Lin, Y., An, L., Huang, F., Yao, Y., & Ren, L. (2019). Insulin secretion impairment induced by rosuvastatin partly though autophagy in INS-1E cells. *Cell Biology International*, *44*(1), 127–136. https://doi.org/10.1002/cbin.11208
235. Han, F., Xiao, Q., Peng, S., Che, X., Jiang, L., Shao, Q., & He, B. (2017). Atorvastatin ameliorates LPS-induced inflammatory response by autophagy via AKT/mTOR signaling pathway. *Journal of Cellular Biochemistry*, *119*(2), 1604–1615. https://doi.org/10.1002/jcb.26320
236. Yamamoto, A., Tagawa, Y., Yoshimori, T., Moriyama, Y., Masaki, R., & Tashiro, Y. (1998). Bafilomycin A1 prevents maturation of autophagic vacuoles by inhibiting fusion between autophagosomes and lysosomes in rat hepatomacell line, H-4-II-E cells. Cell Structure and Function, 23(1), 33–42. https://doi.org/10.1247/csf.23.33
237. Whitton, B., Okamoto, H., Packham, G., & Crabb, S. J. (2018). Vacuolar ATPase as a potential therapeutic target and mediator of treatment resistance in cancer. *Cancer Medicine*, *7*(8), 3800–3811. https://doi.org/10.1002/cam4.1594
238. Lu, X., Chen, L., Chen, Y., Shao, Q., & Qin, W. (2015). Bafilomycin A1 inhibits the growth and metastatic potential of the BEL-7402 liver cancer and HO-8910 ovarian cancer cell lines and induces alterations in their microRNA expression. Experimental and Therapeutic Medicine, 10(5), 1829–1834. https://doi.org/10.3892/etm.2015.2758
239. Gulyás, B., Sovago, J., Gomez-Mancilla, B., Jia, Z., Szigeti, C., Gulya, K., Schumacher, M., Maguire, R. P., Gasparini, F., & Halldin, C. (2014). Decrease of mGluR5 receptor density goes parallel with changes in enkephalin and substance P immunoreactivity in Huntington's disease: a preliminary investigation in the postmortem human brain. Brain Structure and Function, 220(5), 3043–3051. https://doi.org/10.1007/s00429-014-0812-y
240. van Rossum, G. (1995) Python reference manual. In Department of Computer Science; Centrum Wiskunde & Informatica: Amsterdam, The Netherlands; ISSN 0169-118X.
241. Harris, C. R., Millman, K. J., Van Der Walt, S. J., Gommers, R., Virtanen, P., Cournapeau, D., Wieser, E., Taylor, J., Berg, S., Smith, N. J., Kern, R., Picus, M., Hoyer, S., Van Kerkwijk, M. H., Brett, M., Haldane, A., Del Río, J. F., Wiebe, M., Peterson, P., Gérard-Marchant, P., Sheppard, K., Reddy, T., Weckesser, W, Abbasi, H., Gohlke, C., & Oliphant, T. E. (2020). Array programming with NumPy. Nature, 585(7825), 357–362. https://doi.org/10.1038/s41586-020-2649-2
242. Bradski, G. (2000). The OpenCV Library. Dr. Dobb's J. Software Tools, 25/11, 122–125.
243. Bisong, E. (2019). Google Colaboratory. In Apress eBooks (pp. 59–64). https://doi.org/10.1007/978-1-4842-4470-8_7

244. Schneider, C. A., Rasband, W. S., & Eliceiri, K. W. (2012). NIH Image to ImageJ: 25 years of image analysis. Nature Methods, 9(7), 671–675. https://doi.org/10.1038/nmeth.2089
245. Lin, M., Chen, Q., & Yan, S. (2013). Network in network. arXiv (Cornell University). https://doi.org/10.48550/arxiv.1312.4400
246. Selvaraju, R. R., Cogswell, M., Das, A., Vedantam, R., Parikh, D., & Batra, D. (2019). Grad-CAM: Visual explanations from deep networks via gradient-based localization. International Journal of Computer Vision, 128(2), 336–359. https://doi.org/10.1007/s11263-019-01228-7
247. Bae, W., Noh, J., & Kim, G. (2020). Rethinking class activation mapping for weakly supervised object localization. In Lecture notes in computer science (pp. 618–634). https://doi.org/10.1007/978-3-030-58555-6_37
248. Iandola, F. N., Han, S., Moskewicz, M. W., Ashraf, K., Dally, W. J., & Keutzer, K. (2016). SqueezeNet: AlexNet-level accuracy with 50x fewer parameters and <0.5MB model size. arXiv (Cornell University). https://doi.org/10.48550/arxiv.1602.07360
249. He, K., & Sun, J. (2012). Statistics of patch offsets for image completion. In Lecture notes in computer science (pp. 16–29). https://doi.org/10.1007/978-3-642-33709-3_2
250. Jiangtao, W., Ruhaiyem, N. I. R., & Panpan, F. (2025). A comprehensive review of U-Net and its variants: Advances and applications in medical image segmentation. IET Image Processing, 19(1). https://doi.org/10.1049/ipr2.70019
251. Solopov, M., Chechekhina, E., Kavelina, A., Akopian, G., Turchin, V., Popandopulo, A., Filimonov, D., & Ishchenko, R. (2025). Comparative study of deep transfer learning models for semantic segmentation of human mesenchymal stem cell micrographs. International Journal of Molecular Sciences, 26(5), 2338. https://doi.org/10.3390/ijms26052338
252. Ibragimov, A., Senotrusova, S., Markova, K., Karpulevich, E., Ivanov, A., Tyshchuk, E., Grebenkina, P., Stepanova, O., Sirotskaya, A., Kovaleva, A., Oshkolova, A., Zementova, M., Konstantinova, V., Kogan, I., Selkov, S., & Sokolov, D. (2023). Deep semantic segmentation of angiogenesis images. International Journal of Molecular Sciences, 24(2), 1102. https://doi.org/10.3390/ijms24021102
253. Dwibedi, D., Misra, I., & Hebert, M. (2017). Cut, paste and learn: Surprisingly easy synthesis for instance detection. In Proceedings of the IEEE International Conference on Computer Vision, Pp. 1310–1319, 1310–1319. https://doi.org/10.1109/iccv.2017.146
254. Ghiasi, G., Cui, Y., Srinivas, A., Qian, R., Lin, T., Cubuk, E. D., Le, Q. V., & Zoph, B. (2021). Simple Copy-Paste is a strong data augmentation method for instance segmentation. IEEE/CVF Conference on Computer Vision and Pattern Recognition (CVPR). https://doi.org/10.1109/cvpr46437.2021.00294
255. Zhang, J., Zhang, Y., & Xu, X. (2021). ObjectAUG: Object-level data augmentation for semantic image segmentation. International Joint Conference on Neural Networks (IJCNN). https://doi.org/10.1109/ijcnn52387.2021.9534020
256. Liu, X., Ono, K., & Bise, R. (2024). A data augmentation approach that ensures the reliability of foregrounds in medical image segmentation. Image and Vision Computing, 147, 105056. https://doi.org/10.1016/j.imavis.2024.105056
257. Yang, J., Zhang, Y., Liang, Y., Zhang, Y., He, L., & He, Z. (2021). TumorCP: a simple but effective object-level data augmentation for tumor segmentation. arXiv (Cornell University). https://doi.org/10.48550/arxiv.2107.09843
258. Dai, P., Dong, L., Zhang, R., Zhu, H., Wu, J., & Yuan, K. (2022). Soft-CP: a credible and effective data augmentation for semantic segmentation of medical lesions. arXiv (Cornell University). https://doi.org/10.48550/arxiv.2203.10507
259. Park, S., Choi, Y., & Hwang, H. (2023). SACuP: Sonar image augmentation with cut and paste based databank for semantic segmentation. Remote Sensing, 15(21), 5185. https://doi.org/10.3390/rs15215185

260. Brorsson, E., Åkesson, K., Svensson, L., & Bengtsson, K. (2024). ECAP: Extensive Cut-and-Paste augmentation for unsupervised domain adaptive semantic segmentation. IEEE International Conference on Image Processing (ICIP), 610–616. https://doi.org/10.1109/icip51287.2024.10647390
261. Zwanenburg, A., Leger, S., Agolli, L., Pilz, K., Troost, E. G. C., Richter, C., & Löck, S. (2019). Assessing robustness of radiomic features by image perturbation. Scientific Reports, 9(1). https://doi.org/10.1038/s41598-018-36938-4
262. Lo Iacono, F., Maragna, R., Pontone, G., & Corino, V. D. A. (2024). A novel data augmentation method for radiomics analysis using image perturbations. Deleted Journal, 37(5), 2401–2414. https://doi.org/10.1007/s10278-024-01013-0
263. De Assis Soares, L., Côco, K. F., Ciarelli, P. M., & Salles, E. O. T. (2020). A class-independent texture-separation method based on a pixel-wise binary classification. Sensors, 20(18), 5432. https://doi.org/10.3390/s20185432
264. Guan, S., Samala, R. K., Kahaki, S. M. M., & Chen, W. (2024). Restorable synthesis: Average synthetic segmentation converges to a polygon approximation of an object contour in medical images. IEEE Southwest Symposium on Image Analysis and Interpretation (SSIAI), Santa Fe, NM, USA, 2024, Pp. 77-80, 77–80. https://doi.org/10.1109/ssiai59505.2024.10508669
265. Yeung, M., Sala, E., Schönlieb, C., & Rundo, L. (2021). Unified focal loss: Generalising Dice and cross entropy-based losses to handle class imbalanced medical image segmentation. Computerized Medical Imaging and Graphics, 95, 102026. https://doi.org/10.1016/j.compmedimag.2021.102026
266. Abadi, M., Agarwal, A., Barham, P., Brevdo, E., Chen, Z., Citro, C., Corrado, G. S., Davis, A., Dean, J., Devin, M., Ghemawat, S., Goodfellow, I. J., Harp, A., Irving, G., Isard, M., Jia, Y., Józefowicz, R., Kaiser, L., Kudlur, M., Levenberg, J., Mané, D., Monga, R., Moore, S., Murray, D.G., Olah, C., Schuster, M., Shlens, J., Steiner, B., Sutskever, I., Talwar, K., Tucker, P.A., Vanhoucke, V., Vasudevan, V., Viégas, F.B., Vinyals, O., Warden, P., Wattenberg, M., Wicke, M., Yu, Y., & Zheng, X. (2016). TensorFlow: Large-Scale machine learning on heterogeneous distributed systems. arXiv (Cornell University). https://doi.org/10.48550/arxiv.1603.04467
267. Karperien, A. L., Jelinek, H. F., & Buchan, A. M. (2008). Box-counting analysis of microglia form in schizophrenia. Alzheimer's disease and affective disorder. Fractals, 16(02), 103–107. https://doi.org/10.1142/s0218348x08003880
268. Karperien, A. L., Jelinek, H. F., & Milosevic, N. T. (2011). Lacunarity analysis and classification of microglia in neuroscience. In Proceedings of the 8th European Conference on Mathematical and Theoretical Biology, European Society for Mathematical and Theoretical Biology. https://doi.org/10.13140/2.1.3576.6082
269. Puntambekar, S. S., Moutinho, M., Lin, P. B., Jadhav, V., Tumbleson-Brink, D., Balaji, A., Benito, M. A., Xu, G., Oblak, A., Lasagna-Reeves, C. A., Landreth, G. E., & Lamb, B. T. (2022). CX3CR1 deficiency aggravates amyloid driven neuronal pathology and cognitive decline in Alzheimer's disease. Molecular Neurodegeneration, 17(1). https://doi.org/10.1186/s13024-022-00545-9
270. Pedregosa, F., Varoquaux, G., Gramfort, A., Michel, V., Thirion, B., Grisel, O., Blondel, M., Prettenhofer, P., Weiss, R., Dubourg, V., Vanderplas, J., Passos, A., Cournapeau, D., Brucher, M., Perrot, M., & Duchesnay, É. (2011). SciKit-Learn: Machine learning in Python. Journal of Machine Learning Research, 12, 2825–2830. https://doi.org/10.48550/arXiv.1201.0490
271. West, R. M. (2021). Best practice in statistics: The use of log transformation. Annals of Clinical Biochemistry International Journal of Laboratory Medicine, 59(3), 162–165. https://doi.org/10.1177/00045632211050531
272. Pither, J. Tutorials for BIOL202: Introduction to biostatistics. Available online: https://ubco-biology.github.io/BIOL202/index.html

273. McKinney, W. (2010). Data structures for statistical computing in Python. Proceedings of the Python in Science Conferences, 56–61. https://doi.org/10.25080/majora-92bf1922-00a
274. Virtanen, P., Gommers, R., Oliphant, T. E., Haberland, M., Reddy, T., Cournapeau, D., Burovski, E., Peterson, P., Weckesser, W., Bright, J., Van Der Walt, S. J., Brett, M., Wilson, J., Millman, K. J., Mayorov, N., Nelson, A. R. J., Jones, E., Kern, R., Larson, E., Carey, C. J., Polat, I., Moore, E. W., VanderPlas, J., Laxade, D., Perktold, J., Cimrman, R., Henriksen, I., Quintero, E. A., Harris, C. R., Archibald, A. M., Ribeiro, A. H., Pedregosa, F., van Mulbregt, P., & SciPy 1.0 Contributors (2020). SciPy 1.0: fundamental algorithms for scientific computing in Python. Nature Methods, 17(3), 261–272. https://doi.org/10.1038/s41592-019-0686-2
275. Hunter, J. D. (2007). MatPlotLib: a 2D Graphics environment. Computing in Science & Engineering, 9(3), 90–95. https://doi.org/10.1109/mcse.2007.55
276. R Core Team. R (2012). A language and environment for statistical computing; R Foundation for Statistical Computing, ISBN 3-900051-07-0. Available online: https://www.R-pr-oject.org/
277. Oquab, M., Bottou, L., Laptev, I., & Sivic, J. (2015). Is object localization for free? - Weakly-supervised learning with convolutional neural networks. IEEE Conference on Computer Vision and Pattern Recognition (CVPR), Boston, MA, USA, 2015, Pp. 685-694. https://doi.org/10.1109/cvpr.2015.7298668
278. Pinheiro, P. O., & Collobert, R. (2014). From image-level to pixel-level labeling with convolutional networks. arXiv (Cornell University). https://doi.org/10.48550/arxiv.1411.6228
279. Dogan, Y. (2023). A new global pooling method for deep neural networks: Global Average of Top-K Max-Pooling. Traitement Du Signal, 40(2), 577–587. https://doi.org/10.18280/ts.400216
280. Nieradzik, L., Stephani, H., & Keuper, J. (2024). Top-GAP: Integrating size priors in CNNs for more interpretability, Robustness, and Bias Mitigation. arXiv (Cornell University). https://doi.org/10.48550/arxiv.2409.04819
281. Christlein, V., Spranger, L., Seuret, M., Nicolaou, A., Kral, P., & Maier, A. (2019). Deep Generalized Max Pooling. International Conference on Document Analysis and Recognition (ICDAR), Sydney, NSW, Australia, 2019, Pp. 1090-1096, 1090–1096. https://doi.org/10.1109/icdar.2019.00177
282. Chattopadhay, A., Sarkar, A., Howlader, P., & Balasubramanian, V. N. (2018). Grad-CAM++: Generalized gradient-based visual explanations for deep convolutional networks. IEEE Winter Conference on Applications of Computer Vision (WACV), Lake Tahoe, NV, USA, 2018, Pp. 839-847. https://doi.org/10.1109/wacv.2018.00097
283. Wang, H., Wang, Z., Du, M., Yang, F., Zhang, Z., Ding, S., Mardziel, P., & Hu, X. (2020). Score-CAM: Score-weighted visual explanations for convolutional neural networks. IEEE/CVF Conference on Computer Vision and Pattern Recognition Workshops (CVPRW), pp. 111-119. https://doi.org/10.1109/cvprw50498.2020.00020
284. Englebert, A., Cornu, O., & De Vleeschouwer, C. (2024). Poly-cam: high resolution class activation map for convolutional neural networks. Machine Vision and Applications, 35(4). https://doi.org/10.1007/s00138-024-01567-7
285. Shinde, S., Chougule, T., Saini, J., & Ingalhalikar, M. (2019). HR-CAM: Precise localization of pathology using multi-level learning in CNNs. arXiv (Cornell University). https://doi.org/10.48550/arxiv.1909.12919
286. Olsson, V., Tranheden, W., Pinto, J., & Svensson, L. (2021). ClassMix: Segmentation-based data augmentation for semi-supervised learning. IEEE Winter Conference on Applications of Computer Vision (WACV), Pp. 1368-1377, 1368–1377. https://doi.org/10.1109/wacv48630.2021.00141
287. Su, Y., Sun, R., Lin, G., & Wu, Q. (2021). Context decoupling augmentation for weakly supervised semantic segmentation. IEEE/CVF International Conference on Computer Vision (ICCV), pp. 6984-6994. https://doi.org/10.1109/iccv48922.2021.00692

288. Sun, D., Dornaika, F., & Charafeddine, J. (2024). LCAMix: Local-and-contour aware grid mixing based data augmentation for medical image segmentation. Information Fusion, 110, 102484. https://doi.org/10.1016/j.inffus.2024.102484
289. Sun, D., Dornaika, F., & Barrena, N. (2024). HSMix: Hard and soft mixing data augmentation for medical image segmentation. Information Fusion, 102741. https://doi.org/10.1016/j.inffus.2024.102741
290. Del Mar Fernández-Arjona, M., Grondona, J. M., Granados-Durán, P., Fernández-Llebrez, P., & López-Ávalos, M. D. (2017). Microglia morphological categorization in a RAT model of neuroinflammation by hierarchical cluster and principal components analysis. Frontiers in Cellular Neuroscience, 11. https://doi.org/10.3389/fncel.2017.00235
291. Stojić, D., Radošević, D., Rajković, N., & Milošević, N. T. (2021). 2D images of astrocytes in the human principal olivary nucleus: Monofractal analysis of the morphology. Journal of Biosciences and Medicines, 09(09), 38–48. https://doi.org/10.4236/jbm.2021.99004
292. Amin, E., Elgammal, Y. M., Zahran, M. A., & Abdelsalam, M. M. (2023). Alzheimer's disease: new insight in assessing of amyloid plaques morphologies using multifractal geometry based on Naive Bayes optimized by random forest algorithm. Scientific Reports, 13(1). https://doi.org/10.1038/s41598-023-45972-w
293. Barton, S. M., To, E., Rogers, B. P., Whitmore, C., Uppal, M., Matsubara, J. A., & Pham, W. (2021b). Inhalable thioflavin S for the detection of amyloid beta deposits in the retina. Molecules, 26(4), 835. https://doi.org/10.3390/molecules26040835
294. Qiu, Y., Jin, T., Mason, E., & Campbell, M. C. W. (2020). Predicting thioflavin fluorescence of retinal amyloid deposits associated with Alzheimer's disease from their polarimetric properties. Translational Vision Science & Technology, 9(2), 47. https://doi.org/10.1167/tvst.9.2.47

I.

International Journal of
Molecular Sciences

MDPI

Article

Automated Segmentation and Morphometric Analysis of Thioflavin-S-Stained Amyloid Deposits in Alzheimer's Disease Brains and Age-Matched Controls Using Weakly Supervised Deep Learning

Gábor Barczánfalvi [1,2], Tibor Nyári [2], József Tolnai [2], László Tiszlavicz [3], Balázs Gulyás [4,5] and Karoly Gulya [1,*]

[1] Department of Cell Biology and Molecular Medicine, University of Szeged, 6720 Szeged, Hungary; barczanfalvi.gabor@med.u-szeged.hu
[2] Department of Medical Physics and Informatics, University of Szeged, 6720 Szeged, Hungary; nyari.tibor@med.u-szeged.hu (T.N.); tolnai.jozsef@med.u-szeged.hu (J.T.)
[3] Department of Pathology, University of Szeged, 6725 Szeged, Hungary; tiszlavicz.laszlo@med.u-szeged.hu
[4] Department of Clinical Neuroscience, Karolinska Institute, 171 77 Stockholm, Sweden; balazs.gulyas@ki.se or balazs.gulyas@ntu.edu.sg
[5] Cognitive Neuroimaging Centre, Nanyang Technological University, Singapore 636921, Singapore
* Correspondence: gulyak@bio.u-szeged.hu

Abstract

Alzheimer's disease (AD) involves the accumulation of amyloid-β (Aβ) plaques, whose quantification plays a central role in understanding disease progression. Automated segmentation of Aβ deposits in histopathological micrographs enables large-scale analyses but is hindered by the high cost of detailed pixel-level annotations. Weakly supervised learning offers a promising alternative by leveraging coarse or indirect labels to reduce the annotation burden. We evaluated a weakly supervised approach to segment and analyze thioflavin-S-positive parenchymal amyloid pathology in AD and age-matched brains. Our pipeline integrates three key components, each designed to operate under weak supervision. First, robust preprocessing (including retrospective multi-image illumination correction and gradient-based background estimation) was applied to enhance image fidelity and support training, as models rely more on image features. Second, class activation maps (CAMs), generated by a compact deep classifier SqueezeNet, were used to identify, and coarsely localize amyloid-rich parenchymal regions from patch-wise image labels, serving as spatial priors for subsequent refinement without requiring dense pixel-level annotations. Third, a patch-based convolutional neural network, U-Net, was trained on synthetic data generated from micrographs based on CAM-derived pseudo-labels via an extensive object-level augmentation strategy, enabling refined whole-image semantic segmentation and generalization across diverse spatial configurations. To ensure robustness and unbiased evaluation, we assessed the segmentation performance of the entire framework using patient-wise group k-fold cross-validation, explicitly modeling generalization across unseen individuals, critical in clinical scenarios. Despite relying on weak labels, the integrated pipeline achieved strong segmentation performance with an average Dice similarity coefficient (≈0.763) and Jaccard index (≈0.639), widely accepted metrics for assessing segmentation quality in medical image analysis. The resulting segmentations were also visually coherent, demonstrating that weakly supervised segmentation is a viable alternative in histopathology, where acquiring dense annotations is prohibitively labor-intensive and time-consuming. Subsequent morphometric analyses on automatically segmented Aβ deposits revealed size-, structural complexity-, and global geometry-related

check for updates

Academic Editor: Hao Lv

Received: 14 June 2025
Revised: 19 July 2025
Accepted: 21 July 2025
Published: 24 July 2025

Citation: Barczánfalvi, G.; Nyári, T.; Tolnai, J.; Tiszlavicz, L.; Gulyás, B.; Gulya, K. Automated Segmentation and Morphometric Analysis of Thioflavin-S-Stained Amyloid Deposits in Alzheimer's Disease Brains and Age-Matched Controls Using Weakly Supervised Deep Learning. *Int. J. Mol. Sci.* **2025**, *26*, 7134. https://doi.org/10.3390/ijms26157134

II.

scientific reports

Check for updates

OPEN

The kynurenic acid analog SZR104 induces cytomorphological changes associated with the anti-inflammatory phenotype in cultured microglia

Melinda Szabo[1,7], Noémi Lajkó[1,7], Karolina Dulka[1], Gábor Barczánfalvi[1], Bálint Lőrinczi[2,3], István Szatmári[2,3], András Mihály[4], László Vécsei[5,6] & Karoly Gulya[1]✉

We previously showed the anti-inflammatory effects of kynurenic acid (KYNA) and its brain-penetrable analog *N*-(2-(dimethylamino)ethyl)-3-(morpholinomethyl)-4-hydroxyquinoline-2-carboxamide (SZR104) both in vivo and in vitro. Here, we identified the cytomorphological effects of KYNA and SZR104 in secondary microglial cultures established from newborn rat forebrains. We quantitatively analyzed selected morphological aspects of microglia in control (unchallenged), lipopolysaccharide (LPS)-treated (challenged), KYNA- or SZR104-treated, and LPS + KYNA or LPS + SZR104-treated cultures. Multicolor immunofluorescence labeling followed by morphometric analysis (area, perimeter, transformation index, lacunarity, density, span ratio, maximum span across the convex hull, hull circularity, hull area, hull perimeter, max/min radii, mean radius, diameter of bounding circle, fractal dimension, roughness, circularity) on binary (digital) silhouettes of the microglia revealed their morphological plasticity under experimental conditions. SZR104 and, to a lesser degree, KYNA inhibited proinflammatory phenotypic changes. For example, SZR104 treatment resulted in hypertrophied microglia characterized by a swollen cell body, enlarged perimeter, increased transformation index/decreased circularity, increased convex hull values (area, perimeter, mean radius, maximum span, diameter of the bounding circle and hull circularity), altered box-counting parameters (such as fractal dimension), and increased roughness/decreased density. Taken together, analysis of cytomorphological features could contribute to the characterization of the anti-inflammatory activity of SZR104 on cultured microglia.

Abbreviations

ASP	Aspirin
BBB	Blood–brain barrier
CD11b/c	A common epitope shared between CD11b and CD11c (integrin αM and αX chains)
CNS	Central nervous system
DAPI	2-(4-Amidinophenyl)-6-indolecarbamidine dihydrochloride
DMEM	Dulbecco's Modified Eagle's Medium
FBS	Fetal bovine serum
KYNA	Kynurenic acid
LPS	Lipopolysaccharide
PBS	Phosphate-buffered saline

[1]Department of Cell Biology and Molecular Medicine, University of Szeged, Somogyi utca 4., 6720 Szeged, Hungary. [2]ELKH–SZTE Stereochemistry Research Group, Institute of Pharmaceutical Chemistry, University of Szeged, 6720 Szeged, Hungary. [3]Institute of Pharmaceutical Chemistry and Interdisciplinary Excellence Center, University of Szeged, 6720 Szeged, Hungary. [4]Department of Anatomy, University of Szeged, 6724 Szeged, Hungary. [5]Department of Neurology, University of Szeged, 6725 Szeged, Hungary. [6]ELKH–SZTE Neuroscience Research Group, Department of Neurology, Interdisciplinary Excellence Center, University of Szeged, 6725 Szeged, Hungary. [7]These authors contributed equally: Melinda Szabo and Noémi Lajkó. ✉email: gulyak@bio.u-szeged.hu

III.

International Journal of
Molecular Sciences

MDPI

Article

Bafilomycin 1A Affects p62/SQSTM1 Autophagy Marker Protein Level and Autophagosome Puncta Formation Oppositely under Various Inflammatory Conditions in Cultured Rat Microglial Cells

István Pesti [1,2], Gábor Barczánfalvi [1], Karolina Dulka [1], Diana Kata [3], Eszter Farkas [1,2] and Karoly Gulya [1,*]

[1] Department of Cell Biology and Molecular Medicine, University of Szeged, 6720 Szeged, Hungary; pesti.istvan@med.u-szeged.hu (I.P.); barczanfalvi.gabor@med.u-szeged.hu (G.B.); karolina.dulka@med.u-szeged.hu (K.D.); farkas.eszter1@med.u-szeged.hu (E.F.)
[2] HCEMM-USZ Group of Cerebral Blood Flow and Metabolism, University of Szeged, 6720 Szeged, Hungary
[3] Department of Laboratory Medicine, University of Szeged, 6725 Szeged, Hungary; kata.diana@med.u-szeged.hu
* Correspondence: gulyak@bio.u-szeged.hu

Abstract: Regulation of autophagy through the 62 kDa ubiquitin-binding protein/autophagosome cargo protein sequestosome 1 (p62/SQSTM1), whose level is generally inversely proportional to autophagy, is crucial in microglial functions. Since autophagy is involved in inflammatory mechanisms, we investigated the actions of pro-inflammatory lipopolysaccharide (LPS) and anti-inflammatory rosuvastatin (RST) in secondary microglial cultures with or without bafilomycin A1 (BAF) pretreatment, an antibiotic that potently inhibits autophagosome fusion with lysosomes. The levels of the microglia marker protein Iba1 and the autophagosome marker protein p62/SQSTM1 were quantified by Western blots, while the number of p62/SQSTM1 immunoreactive puncta was quantitatively analyzed using fluorescent immunocytochemistry. BAF pretreatment hampered microglial survival and decreased Iba1 protein level under all culturing conditions. Cytoplasmic p62/SQSTM1 level was increased in cultures treated with LPS+RST but reversed markedly when BAF+LPS+RST were applied together. Furthermore, the number of p62/SQSTM1 immunoreactive autophagosome puncta was significantly reduced when RST was used but increased significantly in BAF+RST-treated cultures, indicating a modulation of autophagic flux through reduction in p62/SQSTM1 degradation. These findings collectively indicate that the cytoplasmic level of p62/SQSTM1 protein and autophagocytotic flux are differentially regulated, regardless of pro- or anti-inflammatory state, and provide context for understanding the role of autophagy in microglial function in various inflammatory settings.

Keywords: autophagosome; autophagy; bafilomycin A1; inflammation; lipopolysaccharide; microglia; p62/SQSTM1; rosuvastatin

Citation: Pesti, I.; Barczánfalvi, G.; Dulka, K.; Kata, D.; Farkas, E.; Gulya, K. Bafilomycin 1A Affects p62/SQSTM1 Autophagy Marker Protein Level and Autophagosome Puncta Formation Oppositely under Various Inflammatory Conditions in Cultured Rat Microglial Cells. *Int. J. Mol. Sci.* **2024**, *25*, 8265. https://doi.org/10.3390/ijms25158265

Academic Editors: Antonia Patruno, Mirko Pesce and Maccarone Rita

Received: 5 July 2024
Revised: 25 July 2024
Accepted: 27 July 2024
Published: 29 July 2024

1. Introduction

Microglia are macrophage-like resident immune cells in the brain that are activated in response to various factors, including cytokines, chemokines, nitric oxide, reactive oxygen intermediates, and various stimuli of neuropathological origin, including trauma, stroke, and infection [1]. Under physiological conditions, microglial cells contribute to the maintenance and resolution of brain homeostasis. In pathological states, they release high levels of pro-inflammatory mediators and cytotoxic factors that activate nearby microglia, which can propagate neuroinflammation and degeneration [2]. Microglia also exert neuroprotective effects, depending on their various functional phenotypes in response to specific stimuli through the production of anti-inflammatory factors [3]. For example, up-regulation of autophagy stimulates microglia to produce anti-inflammatory factors, while inhibition of autophagy results in the release of inflammatory cytokines [4].